X-Ray Diffraction of Some Technologically Important Surfaces

Thesis submitted for the degree of

Doctor of Philosophy

at the University of Leicester

by

Christopher John Walker MA MSci (Cambridge)

Department of Physics and Astronomy

University of Leicester

September 2001

UMI Number: U534707

UMI

Dissertation Publishing

ProQuest

X-Ray Diffraction of Some Technologically Important Surfaces

Christopher J. Walker

Abstract

Surface X-ray diffraction (SXRD) has been used to study the effect of pressure and temperature on the Ni(110)-(2×1)-2CO reconstruction and the effect of temperature on the InSb(001)-c(8×2) reconstruction. The Ni(110)-(2×1)-2CO reconstruction was observed at a carbon monoxide pressure of 2.3 bar and has a structure unchanged from that at 1×10^{-5} mbar. This structure was found to consist of CO molecules near short bridge sites in agreement with other recent studies in high vacuum conditions. Heating at 1×10^{-5} mbar causes a lifting of the (2×1) reconstruction due to desorption of the CO. In contrast, heating in 2.3 bar of CO leads to a massive rearrangement of the surface and the formation of {111} microfacets. The base of the microfacets is ≈ 100 Å across and their surfaces are disrupted from the bulk terminated (111) surface. This is consistent with an enlargement of the lattice due to the dissolution of carbon in the facets.

SXRD and LEED experiments on the c(8×2) reconstruction of InSb(001) show no structural changes on cooling from room temperature to 74K. Key features of the reconstruction are determined which are at variance with the recent model of Jones *et al.*.

Acknowledgements

encouragement.

I'm also like to acknowledge the contribution of Elias Vlieg without whose analysis software much of the work would not have been possible, and to Olof Svensson and Rainer Wilke for incorporating improvements to this software.

Last, but by no means least, I would also like to thank my mum and dad and my sisters Nicola and Stephanie for their continual support and encouragement throughout the PhD.

Contents

List of Figures

List of Tables

.

Chapter 1

Introduction

The study of surfaces is of fundamental scientific and technological interest. Two dimensional systems can have significantly different electronic and magnetic properties to three dimensional systems. For example, the electronic properties of thin layers are exploited in semiconductor lasers [37] and the magnetic properties of multilayers are used in recent hard disk drives [92]. A detailed knowledge of the structure and atomic order of semiconductor surfaces is central to control of the surface electronic properties, and this is becoming increasingly important for device fabrication. Surfaces are also important in heterogeneous catalysis as reactions take place on the catalyst surface; understanding the mechanisms behind these reactions will lead to the design of more efficient catalyst systems with consequent environmental and financial benefits. Surfaces are, therefore, technologically important to a range of industries including the micro-electronics, opto-electronics, magnetics and the chemistry-based industries, especially those involving catalysis [122].

Surface X-ray diffraction (SXRD) is a powerful technique that has become one of the best-trusted methods in determining the structures of surfaces and interfaces [102]. The power of SXRD is due to weak scattering of the X-rays by matter, which permits the use of the single scattering approximation in the analysis, and also means that the technique is not limited to ultra high vacuum (UHV) conditions. As well as the study of surfaces in UHV, SXRD has been used to look at buried interfaces in a solid [54, 136], and the solid liquid interface [146]. In contrast, many of the alternative analysis techniques used in the study of surfaces, such as low energy electron diffraction (LEED), reflection high energy electron diffraction (RHEED), X-ray photoelectron diffraction (XPS), use electrons and these are strongly scattered by matter and therefore can only be used in UHV conditions.

Surface X-ray diffraction (SXRD) is the primary technique used in the research reported here. This thesis reports a study of two systems:

- **Ni(110)-(2×1)–2CO** Many catalysts operate at high gas pressures, often several bars, and it has become apparent that UHV studies cannot be extrapolated to these higher pressures. The Ni(110)-(2×1)–2CO system has been used as a prototypical catalyst surface to bridge this "pressure gap". The effect on the surface of a carbon monoxide pressure of 2.3 bar has been studied both at room temperature and 150°C.

- **InSb(001)-c(8×2)** Indium antimonide is a III-V semiconductor with potential applications in near-infrared detectors, and optoelectronics [62]. Most III-V devices are grown on the group V terminated (001) surface [63]. Although it is well ordered, the indium rich c(8×2) recon-

struction of the (001) surface cannot be used for ordered growth, and it has been suggested that this is due to its structure.

Chapter 2 reviews the "pressure gap" and describes alternative experimental techniques that can be used at these higher pressures. The Ni(110)-(2×1)-2CO system is also introduced. Chapter 3 covers the theory of SXRD. Chapter 4 describes the experimental apparatus used in the experiments, in particular the UHV / high pressure chamber used to perform experiments at the European Synchrotron Radiation Facility (ESRF). Experimental data is analysed with the help of various computer programs which are described in chapter 5 along with some extensions to these programs written by the author.

Chapter 6 reports the experiments performed using SXRD to measure the Ni(110)-(2×1)-2CO reconstruction at a pressure of 2.3 bar. Chapter 7 is an investigation of the microfacets observed on heating Ni(110) in carbon monoxide. The effect of cooling the $c(8\times2)$ reconstruction of the InSb(001) surface is described in chapter 8 and the results obtained are compared with models of other workers. Chapter 9 describes the overall conclusions of the thesis and suggestions for further work using SXRD and other techniques.

Chapter 2

Bridging the Pressure gap

Catalysis is of huge importance in the manufacture of industrial chemicals. One study suggested that 17% of manufactured goods go through at least one step involving catalytic processes [122]. Catalysts are used to increase the rate of chemical reactions, and some examples of this are given in Table 2.1. Understanding the mechanisms behind catalysis will enable the design of more efficient catalyst systems with consequent environmental and financial benefits.

In recent years, catalysts have become of increasing environmental importance in the control of automobile exhaust emissions. Increasingly strict legislation to control the exhaust gas emissions from motor cars in the United States, Europe and elsewhere has resulted in catalytic converters being fitted to motor vehicles. All petrol cars sold in Europe since 1993 have been fitted with catalytic converters, along with over half of the world's 500 million cars and 80% of new cars sold worldwide [79]. Catalytic converters usually contain platinum, palladium and rhodium dispersed on an alumina support. Other

4

chemicals, "promoters", are added to increase the activity and resistance to poisoning of these catalysts.

■ Countries with catalyst forcing legislation by 2000
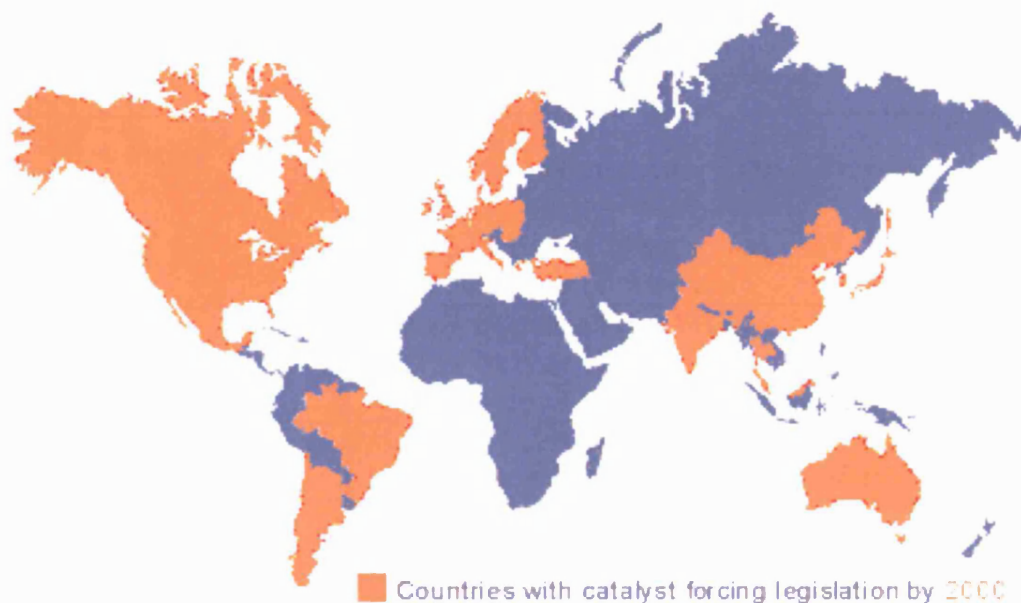
Figure 2.1: Regions of the world where car exhaust gas emission limits can only be met with a catalytic converter (Copyright Johnson Matthey, used with permission) [79].

2.1 The Pressure Gap

Many experiments and computations have been made with the aim of understanding the microscopic process of inhomogeneous catalysis of gaseous species by a solid surface. Until recently, the experiments had only been carried out in Ultra High Vacuum (UHV) with small doses of the active gas. Catalysis processes that occur under real conditions, such as in catalytic converters fitted to cars, or in the chemical industry, do so at pressures of several atmospheres, that is, ten orders of magnitude different from UHV. A simple

Catalyst	Use
Fe or Fe_2O_3	$N_2 + 3H_2 \rightarrow 2NH_3$ Manufacture of ammonia (Haber Process)
Ni	$RC = CH_2 + H_2 \rightarrow RCH_2CH_3$ Hydrogenation of unsaturated oils eg manufacture of margarine
Pt and Rh	$4NH_3 + 5O_2 \rightarrow 4NO + 6H_2O$ $2NO \rightarrow NO_2 \rightarrow HNO_3$ Manufacture of nitric acid (Ostwald process)
$TiCl_4/Al_2(CH_5)_2$	$nC_2H_4 \rightarrow (C_2H_4)n$ Polymerising alkenes (Ziegler method)
V_2O_5	$2SO_2 + O_2 \rightarrow 2SO_3$ Manufacture of sulphuric acid (Contact process)
Cu or CuO	$CH_3CH_2OH + \frac{1}{2}O_2 \rightarrow CH_3CHO + H_2O$ Dehydrogenation of ethanol to produce ethanal (acetaldehyde)
$Pt + Pd + Rh/Al_2O_3$	$CO + NO_x + HC \longrightarrow CO_2 + N_2 + H_2O$ Automobile catalysts. NO_x is oxides of nitrogen HC is unburned hydrocarbons.
Ni	$C_nH_{2(n-1)} + nH2O \rightarrow nCO + (2N - 1)H_2$ Steam-Reforming of Hydrocarbons
Ni	$CO + H2 \rightarrow CH_4 + H_2O$ Methanation of carbon monoxide

Table 2.1: Examples of industrial catalysts and their uses. Taken from various sources [14, 38, 53]. A "Promoter", a substance which enhances performance of the catalyst, is often used [38].

and fundamental question immediately arises: are the chemisorbed struc-
tures that exist under vacuum conditions the same ones that actually exist
on the surface of an operating catalyst? "Bridging the pressure gap" is now
a major aim of fundamental interface research [46]. It has been restricted by
the unavailability of structural techniques that can operate in *real-time* and
in-situ. Surface X-ray diffraction experiments can bridge this pressure gap,
and experiments that do so are described in this thesis.

2.1.1   Origin of the "pressure gap"

Charged particles interact strongly with matter and are, in consequence, fre-
quently used in the study of surfaces; techniques include for example LEED,
RHEED, XPS. They are, however, limited to the study of surfaces in vac-
uum. Recent studies indicate that the surface chemistry at low pressures or
in a vacuum cannot be readily extrapolated to predict the chemistry that
occurs at high pressures [113]; consequently other experimental techniques
are needed. Early surface science measurements on high pressure systems
were carried out in UHV before and after high-pressure studies. These pre-
and post-reaction studies of the catalytically active surfaces revealed that
the structure of the surface is often altered in the reaction [113].

In order to operate *in-situ* and at high pressures, a probe needs to be sur-
face sensitive, and able to penetrate the high pressure gas. Techniques that
can operate at high gas pressures include Scanning Tunnelling Microscope
(STM) [59] and infrared-visible Sum Frequency Generation (SFG) [26, 72],
though neither of these can lead directly to a structural solution. Surface X-

ray diffraction (SXRD) is an established technique for the study of surfaces and can bridge the "pressure gap". X-rays can penetrate the gas and provide information on the gas-solid interface. As explained in chapter 3, SXRD can provide detailed information about the surface structure and morphology and is complementary to STM and SFG. A comparison of the relative merits of these and other techniques is given below.

2.1.2   Scanning Tunnelling Microscopy (STM)

STM is a direct space measurement of the surface and thus does not have the phase problem of X-ray diffraction; it can also measure morphology of the surface. An STM that can operate from UHV conditions to 1 atmosphere [81] and more recently combine these high pressures with high temperatures [58] has been developed by the group of Somorjai. It can also directly observe the presence of domains with different structures.

However, STM can only measure the top layer of a surface, so cannot be used to study buried interfaces easily. STM may also influence the surface; it can cause movement of surface atoms; indeed it has been famously used to move xenon atoms on a Ni(110) surface to form the letters IBM [29, 56]. In addition, the materials used for STM tips are often themselves catalytically active and may therefore induce a reaction that would not otherwise have taken place. The presence of a gas may also degrade the STM tip [131]. Jensen et al [58] change between gold and tungsten tips in order to work in both oxidising and reducing environments. Currently they are not able to work in an oxidising atmosphere at elevated temperature due to the lack of

a suitable tip material.

High pressure STM experiments

The high pressure STM investigations by the group of Somorjai indicate structures not present in UHV conditions. For example, an incommensurate hexagonal overlayer is observed by STM for CO on Pt(111) in the 260-1000 mbar range [59]. On the Rh(111)-CO system, various reconstructions were stable at different gas pressures including some that had not previously been observed including a (2×1) and two forms of $\sqrt{7} \times \sqrt{7}R19°$ [16].

Changes in surface morphology have also been observed. Somorjai and his group observed [58] no change on a stepped Pt(111) surface with nitrogen at pressures up to 1 bar, but found Pt atoms move much more easily under the influence of the STM tip when exposed to CO at high pressure. Heating Pt to 473K in an O_2 pressure of 25 mbar results in significant changes in the steps indicating a decrease in step energy due to the presence of high pressure oxygen. On the platinum (110) face, Jacobs *et al.* [57] observed that the surface massively reconstructs into (111) facets of 100-300 Å corrugation. In 1.6 bar hydrogen though, the surface exhibits various missing row type reconstructions along the [110] direction, but no massive change in the morphology was observed.

2.1.3   Infrared-visible Sum Frequency Generation (SFG)

Infrared-visible Sum Frequency Generation (SFG) is a nonlinear optical technique that makes use of the summing of two photons of frequency ω_1 and ω_2.

If $\omega_1 = \omega_2$, the technique is called second harmonic generation. A vibrational spectrum is obtained by fixing the frequency of one of the photons and tuning the frequency of the other. SFG is surface-specific because such a nonlinear process can only occur in media that do not possess inversion symmetry. A surface or interface is such a medium, in contrast to the bulk of most solids, and the gas phase, which do not give rise to this phenomenon. In consequence, the vibrational spectrum observed by this method can be associated with the interfacial region. By contrast in normal infrared spectroscopy the signals generated in the bulk and the gas phase must be subtracted to produce a "surface" spectrum [113].

SFG can operate with small adsorbate domain sizes, and does not need the well ordered surfaces with large domains essential for surface X-ray diffraction. This enables the study of changes in adsorption site at increasing pressure and also allows the study of the adsorption sites on small crystallites, such as would be found in a catalytic converter. In spite of its success in the study of single crystal surfaces at high pressures [113], the adsorbate site cannot be directly determined.

High pressure SFG experiments

SFG studies of the adsorption of carbon monoxide at pressures between 10^{-10} mbar and 1 bar on the Pt(111) surface found significant changes in the vibrational spectrum of the surface species, particularly at high CO pressures, ascribed to the formation of carbonyl-platinum cluster analogues coadsorbed with an incommensurate CO overlayer [113].

Probing techniques, unaffected by the atmosphere of CO, have been re-

cently used either on Ni or other metals of catalytic interest. Sum frequency generation has been used [26, 72] to measure the vibrations of the CO molecules bonded to metal surfaces, which in turn contain information of the bonding of the adlayer, irrespective of order.

2.1.4 Surface X-Ray Diffraction (SXRD)

Surface X-ray diffraction (SXRD) can be used to determine surface and interface structure [34, 102]. X-ray beams with a wavelength of the order of 1 Å can penetrate to the gas–solid interface with little attenuation. SXRD is therefore able to measure the structure on a surface in the presence of high pressure gas. SXRD is not restricted to measuring the top layer of atoms, but is able to measure a deeper reconstruction, in contrast to STM. Furthermore there is no intrinsic reason why SXRD cannot work in both oxidising and reducing environments and at elevated temperature.

A disadvantage of X-rays is that they may cause ionisation of the gas and thus alter the reaction. SXRD also requires a well ordered surface with a large domain size, and an intense source of X-rays such as that provided by an electron storage ring. The problem is particularly acute for light elements, where the low scattering factor requires the high flux of a third generation synchrotron source.

2.1.5   Surface structure analysis techniques only able to operate at low gas pressures

There are a variety of other techniques used to study the structure of crystals and their surfaces, notably Scanning Electron Microscopy (SEM), neutron diffraction, XPS, LEED and RHEED. These techniques each have their advantages and are often complementary. In particular synchrotron and neutron based measurements require access to large facilities, and limited time is available on these large machines. Diffraction-based techniques suffer from the so called "phase problem" where it is not possible to go directly from measured intensity to a structure.

Neutron Diffraction

Neutron diffraction is sensitive to the scattering factor of the nucleus, whereas for X-rays the scattering factor is proportional to the square of the atomic number. Neutron diffraction is able to measure the position of hydrogen, something almost impossible with X-rays. Isotopic substitution experiments are also possible and allow experiments to show whether a reaction takes place involving atoms in particular sites.

Neutron diffraction is a reciprocal space technique, and like synchrotron experiments requires expensive beamtime (which limits the number of experiments that can be performed). Neutron fluxes are lower than X-ray fluxes, so while it is possible to do reflectivity studies of surfaces [138], surface diffraction is not usually performed.

Electron Diffraction (LEED and RHEED)

Low energy electron diffraction (LEED) and Reflection High energy electron diffraction (RHEED) are standard techniques for measuring surface structure. Electrons interact strongly with matter, so the results are surface sensitive. With a standard phosphor screen it is possible to quickly observe the presence and symmetry of a reconstruction and gain qualitative information on the surface order. With area detectors large data sets can be acquired very quickly. LEED in particular has been used to analyse many surface structures. RHEED has been extensively used to monitor epitaxial growth on a surface *in-situ*.

A problem is that surface contamination may result, particularly with carbon from impurities in the filaments used in the RHEED gun, and the electron beam can cause surface damage. Both techniques suffer from the phase problem and the analysis relies on multiple scattering theory which is computationally expensive and has not been easily accessible to the experimentalist. This is changing, however, with the ever more powerful computers available to the experimentalist, and increasing availability of analysis software.

2.1.6 Summary of surface investigation techniques

It is apparent from the above discussion that each of these techniques have their advantages and disadvantages. These are summarised in table 2.2. The techniques are to a large extent complementary, and complete understanding of a system will come through the application of several techniques.

	STM	LEED	RHEED	Neutron Diffraction	SFG	SXRD
Real space	Yes	No	No	No	No	No
High Gas pressure	Yes	No	No	No	Yes	Yes
Disordered surface	Yes	No	No‡	No	Yes	No
Morphology	Yes	No	No	No	No	Yes
Lab based	Yes	Yes	Yes	No	Yes	No
Surface specific	Yes	Yes	Yes	No†	Yes	Yes

Table 2.2: Summary of merits of techniques used to study surface structure. † Neutron flux from current sources is insufficient for surface diffraction, though reflectivity measurements are possible, for example as performed in [138]. ‡ RHEED is used to study epitaxial growth which may involve the change from order to disorder. In addition, some information on disordered surfaces may be obtained by analysis of the diffuse scatter [68]

2.2   Choice of CO/Ni(110) system

No detailed structural study of the high pressure CO/Ni(110) system has been published as yet. Chapters 6 and 7 describe such experiments. The aim was to extend currently known results at low pressure to high pressure on a catalytic surface, and the system was chosen to facilitate that.

Nickel is well known as a catalyst, and recent studies agree on the structure of the Ni(110)-(2×1)-2CO reconstruction [50, 76, 91, 115, 147], and it has been studied previously with surface X-ray diffraction [103]. The purification of CO by distillation has been performed in the apparatus in previous experiments [98, 116]. The $p2mg$ symmetry prevents the top layer of nickel atoms moving in the plane of the surface, so the reconstruction peaks come mainly from the CO. Nickel has atomic number 28, and is in the top row of the transition metals. The X-ray scattering factor is proportional to Z^2, and

nickel being one of the lighter elements results in a scattering factor which is relatively small, and nearer that of carbon and oxygen than would be the case with other transition metals. The signal in the crystal truncation rods from the CO is thus not completely swamped by the signal from the bulk, so it is possible to determine the registry of the surface with the bulk.

2.2.1   Nickel as a catalyst

Nickel, like many transition metals, is of great commercial significance as a catalyst. Major uses include hydrogenation of unsaturated oils, for example the hydrogenation of vegetable oils to produce margarine [38]. It is used in the catalytic converters fitted to almost all US cars, though concerns about the toxicity of nickel carbonyl have prevented its use in Europe [12]. Other uses include the steam reforming of hydrocarbons [38]; see table 2.1 for more details.

Nickel can be used as a catalyst to produce methane from carbon monoxide and hydrogen [14, 85, 114], by the methanation reaction (equation 2.1).

$$CO + 3H_2 \longrightarrow CH_4 + H_2O \qquad (2.1)$$
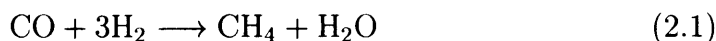
The reaction is thermally activated (temperatures between 150-400°C) and it is carried out at or above atmospheric pressure. It is generally accepted that one of the key steps of the reaction is the dissociation of CO adsorbed on the metal surface. This reaction is a possible starting point in the manufacture of chemicals and fuel from coal instead of oil [45], and may be of importance when reserves of oil run out.

Due to its practical and fundamental interest, the adsorption of CO on Ni surfaces (either single or polycrystalline) has been extensively investigated under UHV conditions with a variety of techniques. Early studies found the surface sensitive to impurities [52], and thus the necessity of UHV conditions for a clean surface.

2.2.2 (110) surfaces

The (110) planes of most fcc transition metals, including nickel, are unstable, and their surface structure is substantially affected by the presence of a number of adsorbates [27].

At low CO coverages on nickel, an incoherent structure is observed by LEED [52]. X-ray photoelectron diffraction shows that at low coverages CO molecules are perpendicular to the surface [137]. STM experiments [115] do not see any reconstruction at low coverages, and this is attributed to the high mobility of CO at sub-saturation coverages.

At saturation coverage on Ni(110), CO forms a $p2mg$ (2×1) structure. A similar structure is formed on the (110) surfaces of Ir, Pd, Pt and Rh [76]. There is a general consensus that the structure of the overlayer is a zig-zag arrangement of CO molecules along the $[1\bar{1}0]$ axis alternately tilted to one side and the other along the [001] direction [76]. The determination of the adsorption site has proved more controversial, and four possible sites are shown in figure 2.2. Most of the recent studies [50, 76, 103, 147] have concluded that the adsorption site is the so called short bridge site (A) as shown in figure 2.2.
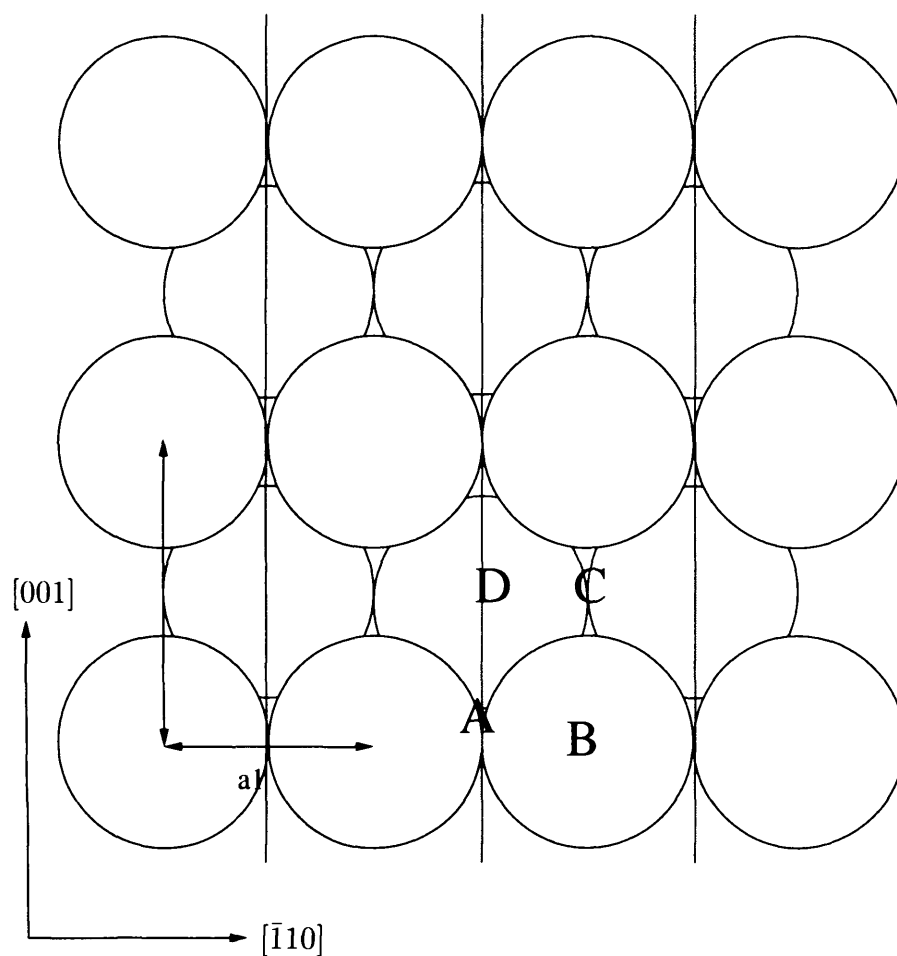
Figure 2.2: Possible adsorption sites for CO on the Ni(110) surface. Short bridge (A), on top (B), long bridge (C), hollow (D). Experiments in this thesis support the assignment to the short bridge sites (A).

The $p2mg(2\times1)$ reconstruction can be prepared at low temperatures by simply dosing with carbon monoxide, but at higher temperatures exists in equilibrium with the gas [52, 103, 137].

The change in CO tilt angle between the low and high coverages implies that it would also be pressure dependent. Wesner [137] found, however, that there were two distinct states. At low coverage, the main axis of the CO was perpendicular to the surface, and at high coverages, the CO was tilted at $21\pm1°$, due to the repulsive CO-CO interaction (which lowers the thermal desorption spectra (TDS) peak). At intermediate coverages, a mixture of perpendicular CO and tilted CO was observed. The study described in chapter 6 finds that even at 2.3 bar, the CO tilt angle is the same as at 10^{-5} mbar, supporting the results of Wesner [137].

2.2.3   Faceting

The chemisorption of an atom or molecule often induces rearrangement of the substrate atoms around the adsorption site. Adsorbate-induced restructuring can involve massive restructuring of the surface by atom transport. For example, sulphur restructures the (111) crystal face of nickel until the metal surface assumes the (100) orientation. Alumina restructures iron through the formation of an iron–aluminate phase to produce (111) crystal faces during ammonia synthesis, regardless of the original crystallite orientation [111].

In the Mond process for purifying nickel, carbon monoxide is passed over the impure nickel, forming nickel carbonyl, $Ni(CO)_4$, a volatile gas. The nickel carbonyl is heated to 200°C and decomposes, depositing pure metallic

nickel.

$$Ni + 4CO \xrightarrow{50°C} Ni(CO)_4 \xrightarrow{200°C} Ni + 4CO \tag{2.2}$$
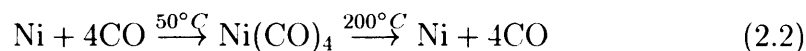
The nickel (111) surface has been found to react to form the carbonyl faster than the (110) and (100) surface [73]. Other studies find the formation of sharp (111) facets after the reaction has proceeded for some time [25].

2.3 Summary

There is a need to develop techniques to determine surface structures to atomic resolution in a gaseous environment. This is an aspect of a wider problem: how to determine structure and morphology at interfaces rather than surfaces. In order to penetrate the environment to the interface, SFG and SXRD employ "photon in, photon out", STM has a different approach and relies on the small distance between the tip and the surface to allow electron tunnelling to be used.

The choice of the Ni(110)-(2×1)-2CO reconstruction as the system to study has been explained. This system is technologically interesting because of its applications in catalysis. The system is a good choice for these high pressure experiments, as the low pressure structure is known, and the relatively low atomic number of nickel means that it does not completely swamp the scattered intensity from the carbon monoxide.

Chapter 3

Surface X-Ray Diffraction Theory

3.1 Introduction

3.1.1 Background

X rays were discovered in 1895 by Wilhelm Röntgen. Seventeen years later, in 1912, Max von Laue suggested that they might be diffracted when passed through a crystal. Laue's suggestion was confirmed almost immediately by Walter Friedrich and Paul Knipping. Later the same year WL Bragg presented a paper to the Cambridge Philosophical Society on how the structure of rock salt could be deduced using X-rays. In 1953, F.Crick, J.D.Watson, M.Wilkins, R. Franklin solved the structure of DNA [134] using X-rays. X-ray diffraction is now routinely used in solving the atomic arrangements of crystal structures.

Surface diffraction

X-rays scatter weakly from atoms, and with laboratory sources their use for the study of surfaces, as opposed to bulk material, was limited. Electron synchrotrons and storage rings have several orders of magnitude more flux than conventional laboratory X-ray sources (figure 3.1) and have transformed surface diffraction experiments from the verge of feasibility to the routinely possible [13].

3.2 Diffraction Theory

In order to explain the technique of surface diffraction, and to put the results in context, a brief introduction to diffraction theory is given. For a more thorough treatment, readers are referred to the many books that cover this, for example Cowley [21] or Giacovazzo [42]. The treatment given here is strongly influenced by Als-Nielsen, Feidenhansl and Giacovazzo [2, 34, 42].

3.2.1 Bragg Diffraction

A simple and intuitive understanding of diffraction can be gained by considering the interference of X-rays scattered from parallel planes (fig 3.2).

When the path travelled by rays scattered from adjacent planes differs by one wavelength, they will constructively interfere. This occurs when

$$2d\sin\theta = n\lambda \qquad (3.1)$$

the Bragg equation.
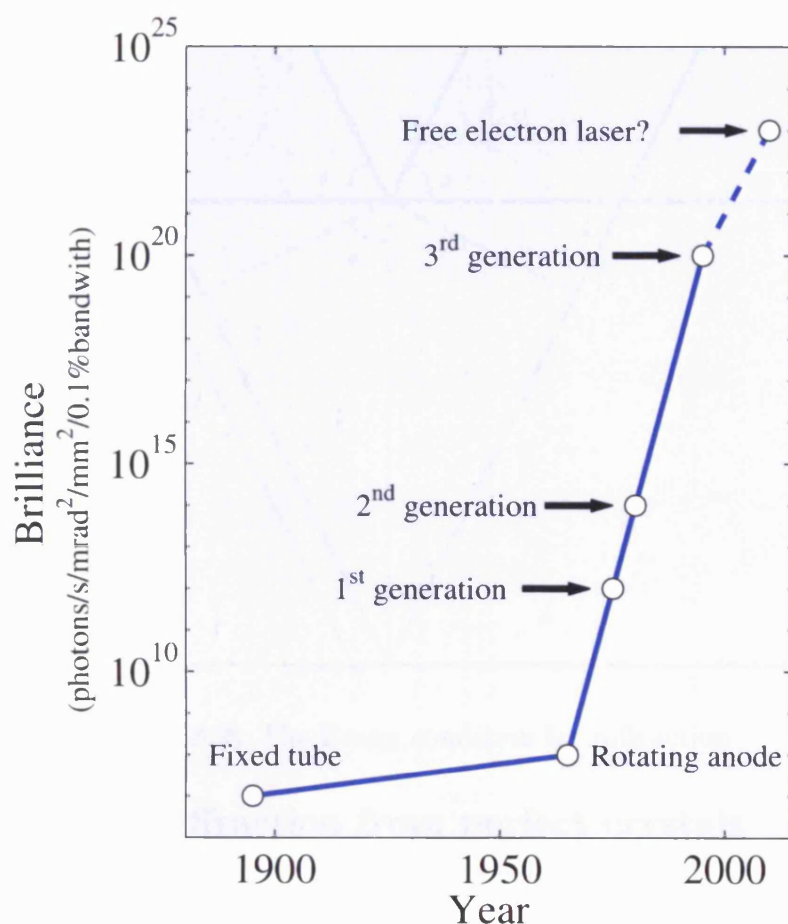
Figure 3.1: Brilliance available from X-ray sources as a function of time. Third generation synchrotron sources such as the ESRF are several orders of magnitude more brilliant than a lab based rotating anode source. Reproduced from *Elements of modern X-ray physics* by , J. Als-Nielsen and D. McMorrow [2] with kind permission of the authors.
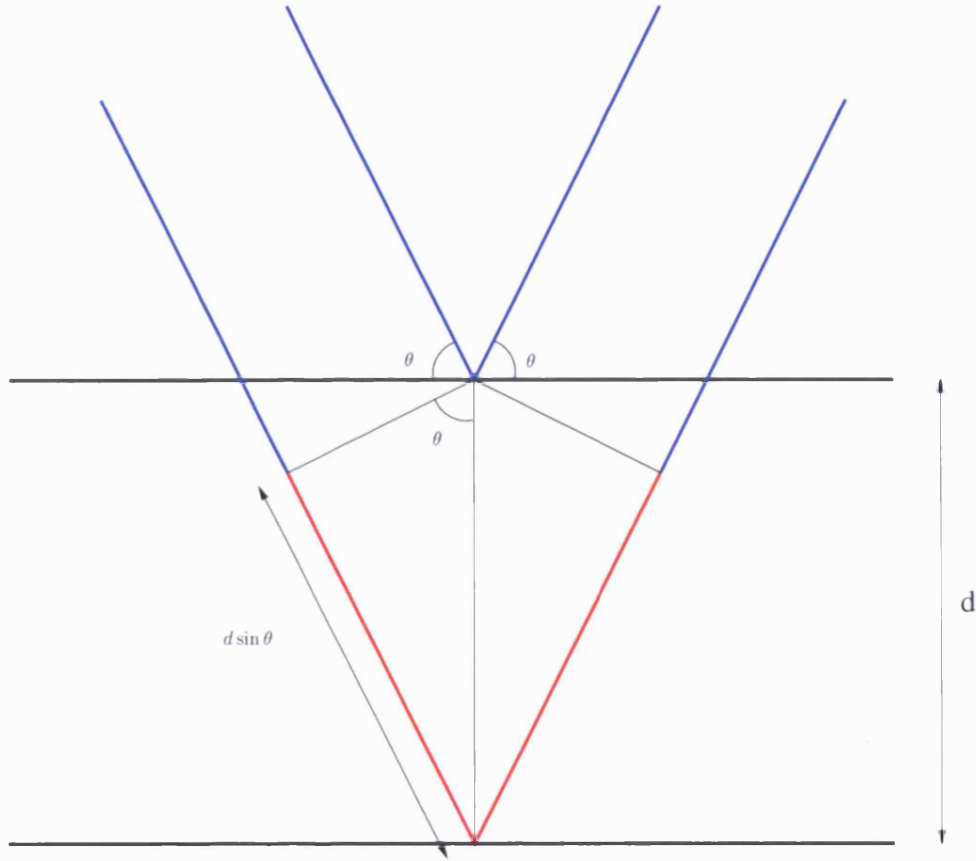
Figure 3.2: The Bragg condition for diffraction

3.2.2 Laue - diffraction from perfect crystals

Consider a plane wave with amplitude E_0 and wave vector $\mathbf{k_i}$ incident on an atom situated at $\mathbf{r}$.

$$\mathbf{E}(\mathbf{r}) = E_0 e^{i(\mathbf{k_i} \cdot \mathbf{r} - \omega t)} \tag{3.2}$$

X-rays are scattered by free electrons according to the Thomson formula. The scattered field E at a distance R from the nucleus has the amplitude

$$E = E_0 \left(\frac{e^2}{mc^2 R} \right) P^{1/2} \qquad (3.3)$$

Where P is the polarisation factor, e is the charge on an electron, m is the mass of the electron.

For horizontally polarised radiation	
$P = 1$	Vertical scattering
$P = cos^2(2\theta)$	Horizontal scattering
$P = \frac{1+cos^2(2\theta)}{2}$	for unpolarised radiation
2θ is the angle between the incident and diffracted beam.	

We are interested only in elastic scattering (eq 3.5), because only elastic scattering will produce constructive interference[1]. As scattering of X-rays is weak we can assume that the scattered wave is made up only of contributions scattered directly from the incident wave, the *single-scattering*, or *kinematical* approximation.

$$\mathbf{k_f} - \mathbf{k_i} = \mathbf{q} \qquad (3.4)$$

$$|\mathbf{k_f}| = |\mathbf{k_i}| \qquad (3.5)$$

Where $\mathbf{k_i}$ is the incident wavevector, $\mathbf{k_f}$ is the wavevector of the scattered wave, and $\mathbf{q}$ is the scattering vector.

---

[1] Inelastic scattering results in no correlation between the incident and scattered photons, and will cause background noise.
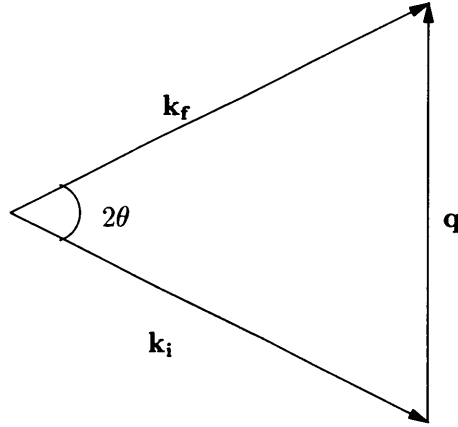
Figure 3.3: Incident and exit wavevectors

From equation 3.3 it can be seen that scattering from protons in the nucleus can be neglected as the $\frac{e}{m}$ factor is nearly two thousand times smaller. The scattering from electron density $\rho(\mathbf{r})$ is then

$$E = \int E_0 \rho(\mathbf{r}) \, d\mathbf{r} \qquad (3.6)$$

$$= E_0 \frac{e^2}{mc^2 R} P^{1/2} \int \rho(\mathbf{r}) e^{i\mathbf{q} \cdot \mathbf{r}} d\mathbf{r} \qquad (3.7)$$

Thus the electric field is proportional to the Fourier transform of the electron density.

A bulk crystal is periodic and has a lattice with

$$\mathbf{R} = m_1 \mathbf{a_1} + m_2 \mathbf{a_2} + m_3 \mathbf{a_3} \qquad (3.8)$$

where $\mathbf{R}$ is a lattice vector, m_1, m_2, m_3 are integers, and $\mathbf{a_i}$ are the basis vectors of the lattice.

The electron density of the crystal can be represented in terms of the electron density of the unit cell $\rho_u(\mathbf{r})$ by the following:

$$\rho(\mathbf{r}) = \left(\rho_u(\mathbf{r}) * \sum_{m_1 m_2 m_3} \delta(\mathbf{r} - \mathbf{R}) \right) S(\mathbf{r}) \tag{3.9}$$

where $*$ represents the convolution operator and $S(\mathbf{r})$ is the crystal shape function.

$$0 \le S(\mathbf{r}) \le 1 \tag{3.10}$$

Substituting equation 3.9 into equation 3.7 and using the convolution theorem (appendix B):

$$E = E_0 \frac{e^2}{mc^2 R} P^{1/2} \overbrace{\int \rho_u(\mathbf{r}) e^{i\mathbf{q}\cdot\mathbf{r}} d\mathbf{r}}^{F(\mathbf{q})}$$

$$\times \int \sum_{m_1 m_2 m_3} \delta(\mathbf{r} - \mathbf{R}) e^{i\mathbf{q}\cdot\mathbf{r}} d\mathbf{r} * \overbrace{\int S(\mathbf{r}) e^{i\mathbf{q}\cdot\mathbf{r}} d\mathbf{r}}^{S(\mathbf{q})} \tag{3.11}$$

$$= E_0 \frac{e^2}{mc^2 R} P^{1/2} F(\mathbf{q}) \sum_{m_1 m_2 m_3} \int \delta(\mathbf{r} - \mathbf{R}) e^{i\mathbf{q}\cdot\mathbf{r}} d\mathbf{r} * S(\mathbf{q}) \tag{3.12}$$

For a perfect infinite crystal, $S(\mathbf{r}) = 1$, for all $\mathbf{r}$, so the contribution from $S(\mathbf{q})$ the shape function vanishes. The diffraction spots are therefore delta functions in reciprocal space, and their position is determined solely by the lattice spacing. The electron density in the unit cell then determines the intensity of those spots.

The electric field E will be non zero when

$$\mathbf{q}.\mathbf{R} = 2n\pi \tag{3.13}$$

Note that this is equivalent to saying that the scattering vector $\mathbf{q}$ is

perpendicular to the Bragg planes, and the magnitude is given by eq 3.14

$$|\mathbf{q}| = \frac{2n\pi}{d} \qquad (3.14)$$

If we define reciprocal lattice vectors $\mathbf{b_i}$ as follows,

$$\mathbf{b_1} = 2\pi \frac{\mathbf{a_2} \wedge \mathbf{a_3}}{\mathbf{a_1} \cdot (\mathbf{a_2} \wedge \mathbf{a_3})} \qquad (3.15)$$

$$\mathbf{b_2} = 2\pi \frac{\mathbf{a_3} \wedge \mathbf{a_1}}{\mathbf{a_1} \cdot (\mathbf{a_2} \wedge \mathbf{a_3})} \qquad (3.16)$$

$$\mathbf{b_3} = 2\pi \frac{\mathbf{a_1} \wedge \mathbf{a_2}}{\mathbf{a_1} \cdot (\mathbf{a_2} \wedge \mathbf{a_3})} \qquad (3.17)$$

Then equation 3.13 is satisfied if

$$\mathbf{q} = h\mathbf{b_1} + k\mathbf{b_2} + l\mathbf{b_3} \qquad (3.18)$$

3.3 Diffraction from surfaces and imperfect crystals

Real crystals are neither perfect nor infinite, so instead of being an infinite series of delta functions, the diffraction pattern will be these delta functions convoluted with the crystal shape function (fig 3.4).

In addition to the broadening of the lines due to the finite size of the crystal, there will be some instrumental broadening due to resolution limits of the instrument.
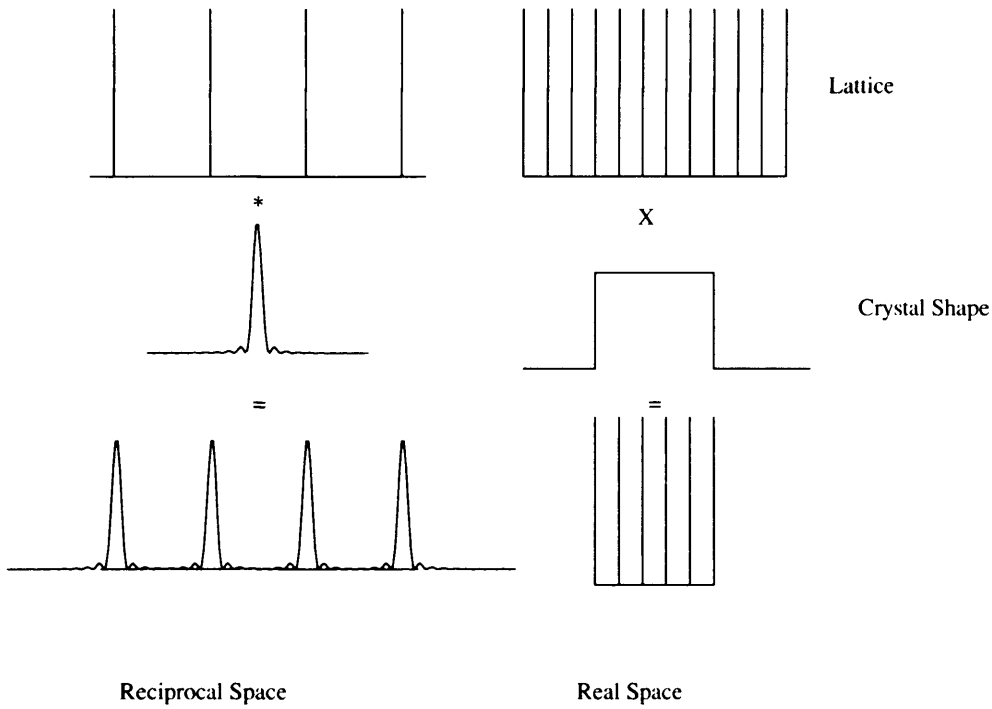
Figure 3.4: The convolution theorem

3.3.1   Diffraction from small crystals

For a small crystal, $S(\mathbf{q})$ results in broadening of the diffraction spots. Consider the case of a one dimensional crystallite. This can be represented in real space by a top hat function (fig 3.5). The electric field is then given by equation 3.12 and is the Fourier transform of a top hat function which is a *sinc* function (where $sinc(x) = \frac{sin(x)}{x}$), as shown in figure 3.6. Therefore the intensity (which is $\propto |E|^2$) will be a $sinc^2$ function. The measured intensity is therefore the convolution of a $sinc^2$ function and a series of delta functions (fig 3.4).

While the domain (or crystal) size could be determined by the minimum of the *sinc* function, in practice it is easier to use the Full Width Half Maximum (FWHM) as, usually many domains of varying sizes are present and
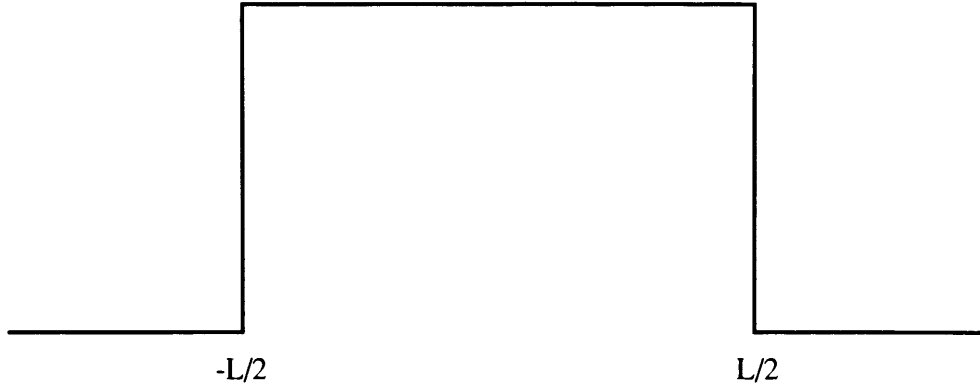
Figure 3.5: A one dimensional crystal

contribute to the diffracted signal, so there will not be a zero in the intensity.

For a "top hat" shape function, $s(x)$, shown in figure 3.5 the shape is given by the following formula:

$$s(x) = \begin{cases} 1 & (|x| < \frac{L}{2}) \\ 0 & \text{otherwise} \end{cases}$$

The diffracted intensity is then given by the Fourier transform of $s(x)$.

$$\int_{-\infty}^{\infty} s(x)e^{2\pi ihx}dx \tag{3.19}$$

$$= \int_{-\frac{L}{2}}^{\frac{L}{2}} e^{2\pi ihx}dx \tag{3.20}$$

$$= \left[\frac{Ae^{2\pi ihx}}{2\pi ih}\right]_{-\frac{L}{2}}^{\frac{L}{2}} \tag{3.21}$$

$$= 2A\frac{sin(\frac{2h\pi L}{2})}{2h\pi L/2} \tag{3.22}$$

$$= 2Asinc(\frac{2h\pi L}{2}) \tag{3.23}$$

The FWHM of sinc(x) is 1.895
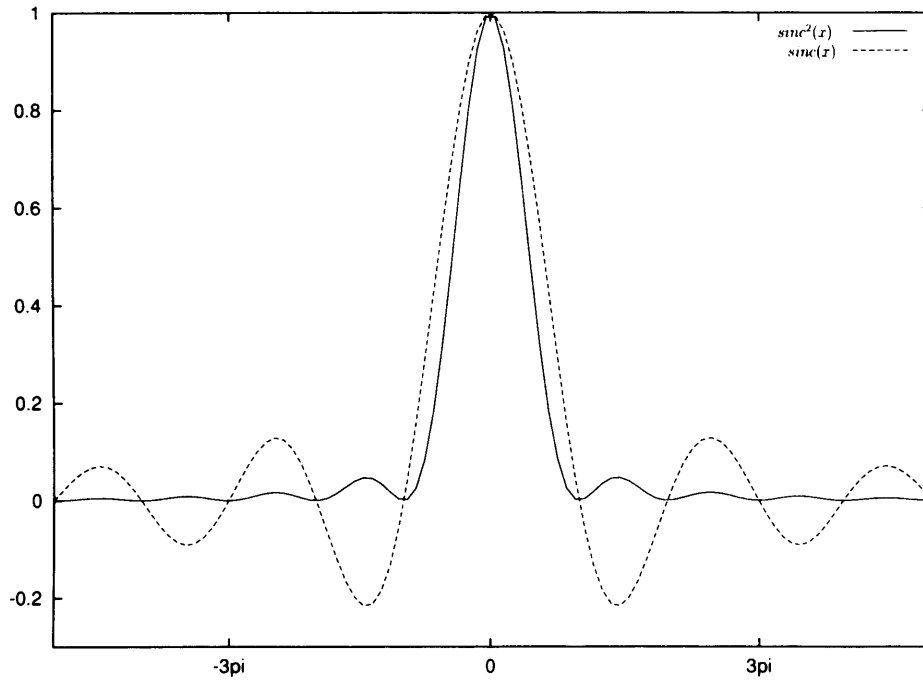
Figure 3.6: A sinc function

Therefore

$$2\pi\Delta h_{FWHM}L = 2 * 1.895 \tag{3.24}$$

$$\Delta h_{FWHM} = \frac{1.895}{\pi L} \tag{3.25}$$

The width in reciprocal space is inversely proportional to the crystal size. Therefore for large crystals the Bragg peaks will be sharp, but for small crystals they will be wider. A limit is placed on the minimum width by the inherent resolution of the instrument.

Surfaces however have domains of varying size which can be described by a correlation function. Vlieg *et al.* [129] have performed a more realistic analysis using an exponential correlation function (eq 3.26).

$$C(\mathbf{r}) = e^{\frac{-r}{L}} \qquad (3.26)$$

Where $C(\mathbf{r})$ is the probability that the height at two positions, separated by r is the same for a correlation length L.

The result derived by Vlieg *et al.*, (equation 3.27) is similar to the one derived above for a for a one dimensional crystallite.

$$\Delta q_{FWHM} = \frac{a_1}{\pi L} \qquad (3.27)$$

3.3.2 Surface Diffraction

The surfaces of crystals frequently adopt structures that are subtly or dramatically different from the bulk terminated surface [20], the surface layers may undergo "relaxation" perpendicular to the surface, or more dramatically "reconstruct" to produce a larger unit cell. Some authors use the term reconstruction when large atomic displacements occur, even though the surface may retain (1×1) periodicity [119]. Reconstruction is particularly common in semiconductors, and results from the reduction in surface energy from a reduction in the number of dangling bonds.

Surface diffraction involves two phenomena not observed in 3-D crystallography. The Crystal Truncation Rod (CTR) is due to termination of the crystal at the surface. A larger unit cell associated with a reconstruction leads to extra reflections (fractional order rods).

Throughout this thesis, the convention used in LEED is followed where the axes are reindexed from the bulk so $\mathbf{a_1}$ and $\mathbf{a_2}$ are in the plane of the

surface and $\mathbf{a_3}$ is perpendicular to the surface.

Fractional order reflections

Figure 3.7 shows a representation of a surface reconstruction with a larger unit cell than that of the bulk. This leads to fractional order reflections that are due only to the reconstruction. They are usually labelled using the lattice of the substrate, but with non-integer values of h and k. As there is no periodicity perpendicular to the surface, these reflections are diffuse in l (fig 3.8). The notation developed by Wood [142] is used to label surface reconstructions. In this notation, a reconstruction that has a periodicity of m unit cells along $\mathbf{a_1}$ and n along $\mathbf{a_2}$ is called an $(m \times n)$ reconstruction, and a $c(m \times n)$ reconstruction has a centred cell. Rotations can also be represented eg $(m \times n)$R19°. An alternative representation using matrices [119] is also used, though not in this thesis, and can represent some reconstructions not represented by the Wood notation.
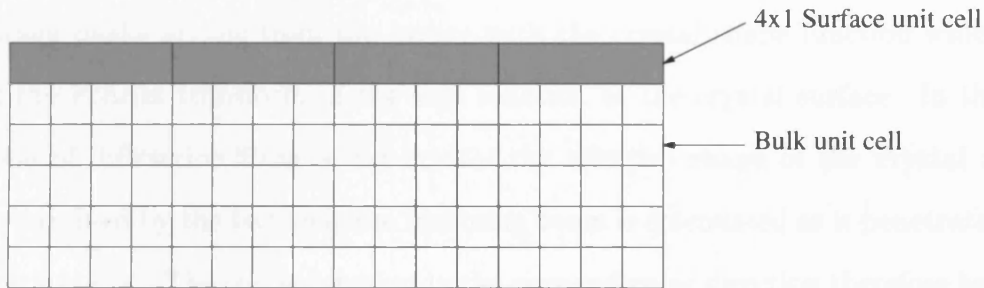
Figure 3.7: Side view (real space) of a model (4×1) surface reconstruction

l

3

2

1

0   1   2   3   → h

● ← Bulk Bragg peak

← Crystal Truncation Rod

← Fractional order rod

Fractional order
in-plane reflection
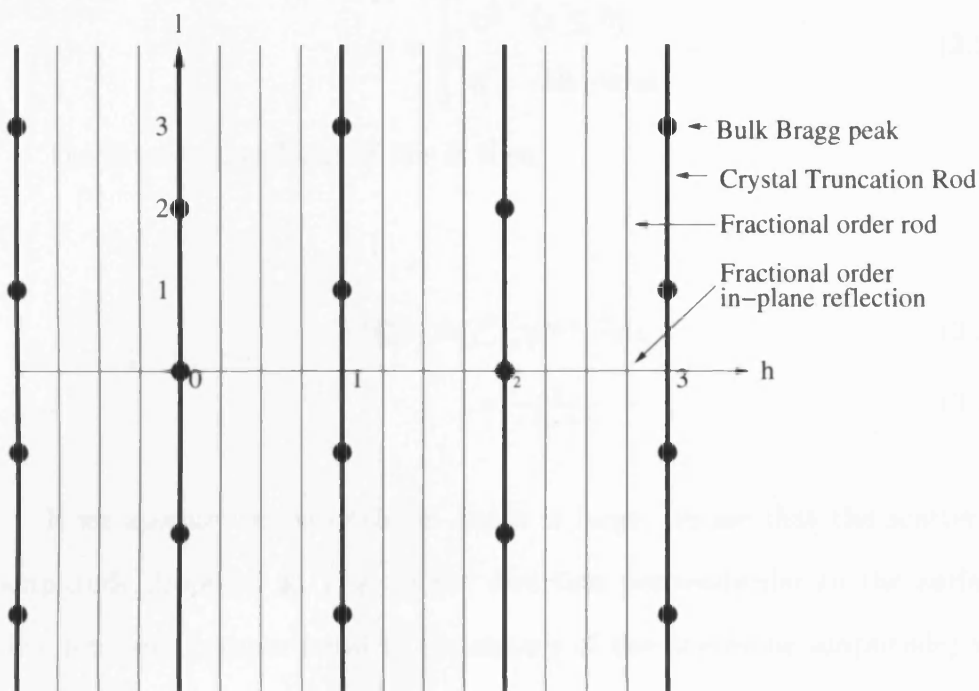
Figure 3.8: Reciprocal space view of a (4×1) reconstruction

Crystal truncation rods

Crystal Truncation Rods (CTRs) are due to the convolution of the sharp Bragg peaks arising from the lattice with the crystal shape function which is the Fourier transform of the step function at the crystal surface. In the case of diffraction from a flat crystal the effective shape of the crystal is determined by the fact that the incoming beam is attenuated as it penetrates the material. The shape function in the perpendicular direction therefore has a step shape at the crystal boundary, and an exponential decay as a function of depth.

The crystal shape function can be given by:

$$s(x) = \begin{cases} e^{\frac{z}{\mu}} & (z \leq 0) \\ 0 & \text{otherwise} \end{cases}$$

(3.28)

The Fourier transform of this is then:

$$S(\mathbf{Q}) = \int_{-\infty}^{0} e^{iq_z z} e^{\frac{z}{\mu}} dz \qquad (3.29)$$

$$= \frac{1}{-iq_z + \frac{1}{\mu}} \qquad (3.30)$$

If we assume the penetration depth is large, we see that the scattering amplitude drops off as $1/q_z$ in the direction perpendicular to the surface. The intensity (proportional to the square of the scattering amplitude) will drop off as $1/q_z^2$.

CTRs are modified by roughness or reconstructions of the surface [129]. They can give information on the registry of the surface to the bulk. Figure 3.9 shows a theoretical (10) CTR of the bulk terminated (001) surface of indium antimonide with no surface relaxation or reconstruction.

3.4 Data analysis techniques

The structure factor is the Fourier transform of the electron density.

$$F(\mathbf{q}) = \int \rho(\mathbf{r}) \exp^{i\mathbf{q}\cdot\mathbf{r}} d\mathbf{r} \qquad (3.31)$$

If the phase of F were known, it would be possible to derive $\rho(\mathbf{r})$ simply by calculating the inverse Fourier transform. The phase of F is not known
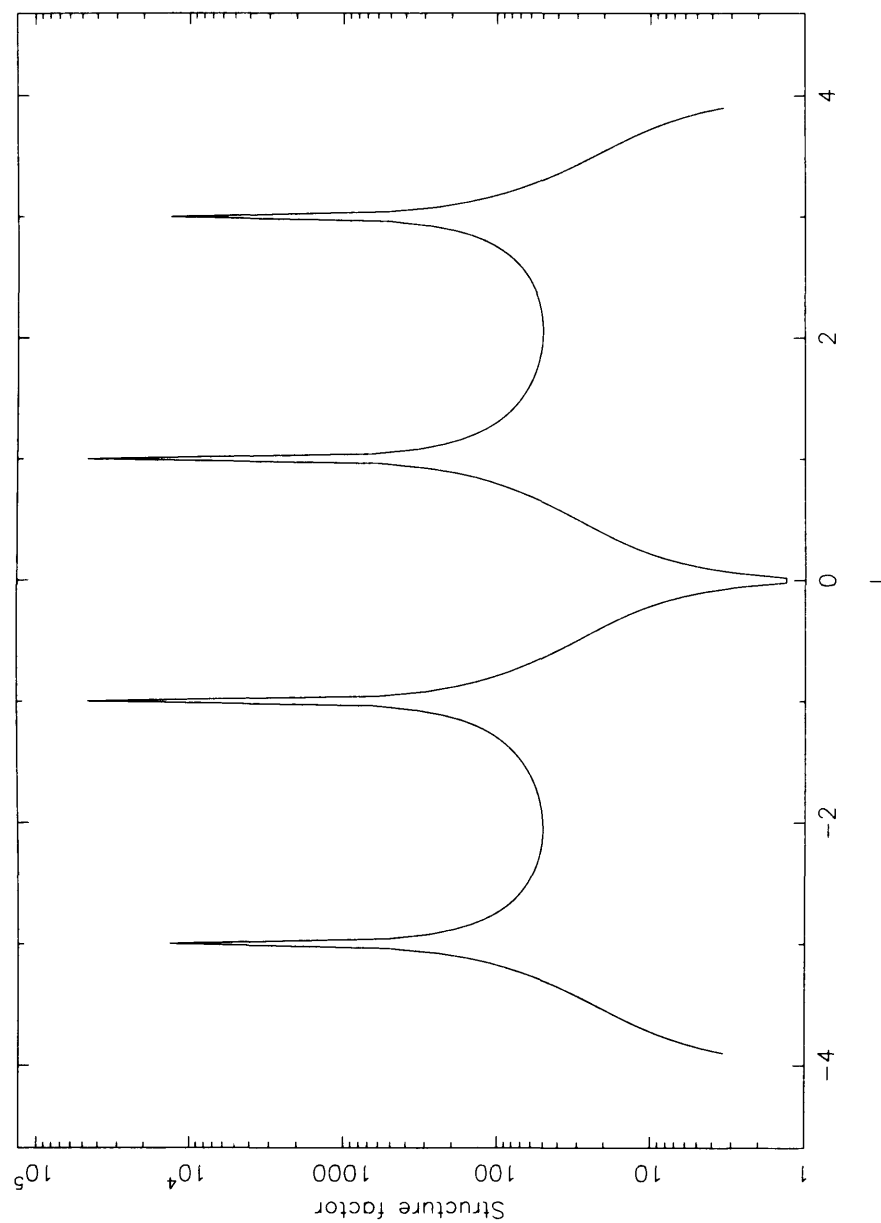
Figure 3.9: The 10 Crystal truncation rod of bulk terminated indium antimonide

however - the classic problem of X-ray diffraction.

There are, currently, no general automatic methods for solving surface crystallographic structures. Most structures solved to date have used Patterson, difference-Fourier or guess and refine methods [102]. The combination of direct methods with the maximum entropy method [43] is promising, but surface diffraction has unique problems, and maximum entropy is still in its infancy when applied to surfaces. In the future it is likely that more use will be made of the phase information available from CTRs [102] which is not currently used.

3.4.1 Patterson Maps

The Fourier transform of $|F|^2$ is known as the Patterson function, which is the autocorrelation function of the electron density. Peaks in the Patterson function therefore correspond to interatomic vectors. It is possible to calculate the Patterson function directly from diffraction data as it does not require the phase of the structure factor F. One such example is shown in figure 8.15, the Patterson function for indium antimonide. The Patterson function, $P(\mathbf{r})$, is defined as

$$P(\mathbf{r}) = \rho(\mathbf{r}) * \rho(-\mathbf{r}) = \int_v \rho(\mathbf{r}')\rho(\mathbf{r} - \mathbf{r}')d\mathbf{r}' \qquad (3.32)$$

$$= \int_v |F(\mathbf{q})| \exp^{2\pi i \mathbf{q} \cdot \mathbf{r}} d\mathbf{q} \qquad (3.33)$$

$$= \frac{1}{V_u} \sum_{hkl} |F_{hkl}|^2 \cos(\mathbf{q} \cdot \mathbf{r}) \qquad (3.34)$$

where $\rho(\mathbf{r})$ is the electron density at $\mathbf{r}$, $\mathbf{q}$ is the momentum transfer vector, and V_u is the volume of a unit cell.

For in-plane data this is then:

$$P(hk) = \sum_{hk} |F_{hk}|^2 cos(hx + ky) \qquad (3.35)$$

where h and k are the in-plane reciprocal lattice coordinates.

Surface diffraction data can yield unique problems. Integer order reflections have a large contribution from the bulk, and are therefore usually excluded. This can, however, lead to negative regions in the Patterson map as effectively this sets the structure factor to zero at these points. Although the validity of this partial Patterson map has been questioned [144], it can be shown [10] that all positive peaks in this partial Patterson function must also be peaks in the full Patterson function. The Patterson function also suffers from series truncation errors. Finally, the Patterson function is easier to interpret if there is a heavy atom, which dominates the scattering, in the unit cell. If there are many light atoms, many peaks occur and it is difficult to pick out important vector information. Heavy atom substitution is sometimes used to reduce this problem.

3.5 Thermal Diffuse Scattering

Atoms are not fixed at definite positions but vibrate about their equilibrium positions giving rise to thermal diffuse scattering which increases the background signal.

This background results in a relative reduction in intensity of the peaks which is more pronounced at high momentum transfers; it is conventionally described by the Debye-Waller B factor which modifies the structure factor.

$$F_{hkl} = \sum_j f_j e^{\frac{-B_j Q^2}{16\pi^2}} e^{2\pi i(hx_j + ky_j + lz_j)} \tag{3.36}$$

The Debye Waller parameter is related to the mean square thermal vibration amplitude $< u^2 >$ by

$$B = 8\pi^2 < u^2 > \tag{3.37}$$

Here B is isotropic. More generally, B can be written as a tensor and the component along the direction of the momentum transfer should be used in the Debye-Waller factor. The structure factor as written above is the form used in fitting a structure model to experimental data. Bulk values of B are tabulated, however for a surface they are usually fitted during the analysis procedure, as they depend on the bond strength and are likely to be different, usually resulting in bigger displacements than the bulk values.

3.6 Scattering from a single unit cell

This section shows that the scattering from the electron density in the unit cell (eq 3.38) can be approximated by summing over the form factors of the atoms in the unit cell (eq 3.40).

$$F(\mathbf{q}) = \int_{\text{unit cell}} \rho_u(\mathbf{r}) e^{i\mathbf{q}\cdot\mathbf{r}} d\mathbf{r} \tag{3.38}$$

$$\approx \int_{\text{unit cell}} \sum_{\text{atoms in cell}} \rho_i \delta(\mathbf{r} - \mathbf{r_i}) e^{i\mathbf{q}\cdot\mathbf{r}} d\mathbf{r} \tag{3.39}$$

but

$$f_i(\mathbf{q}) = \int \rho_{\text{atom}} e^{i\mathbf{q}\cdot\mathbf{r}} d\mathbf{r} \tag{3.40}$$

$$F(\mathbf{q}) = \sum_{\text{unit cell}} f_i(\mathbf{q}) e^{i\mathbf{q}\cdot\mathbf{r}} = \sum_{\text{unit cell}} f_i(\mathbf{q}) e^{2\pi i(hx+ky+lz)} \tag{3.41}$$

These form factors are tabulated [140]. The tabulated scattering factors do not take into account chemical bonding, and have small intrinsic inaccuracies, but for the experiments described in this thesis, they are sufficiently accurate.

Chapter 4

Experimental apparatus and techniques

4.1 Introduction

Synchrotron radiation (SR) has a number of major advantages over conventional laboratory-based X-ray sources. For the experiments in this thesis, the most important property was the high brilliance, that is to say high flux at a given wavelength with small angular divergence and source size, of the X-ray source. Other techniques make use of the other properties of synchrotron sources such as tunable wavelength, polarisation and time structure.

The experiments described in this thesis have been performed using synchrotron radiation at the European Synchrotron Radiation Facility (ESRF) [32] on beamline ID3 [33, 35]. Preliminary experiments were also performed at Daresbury on station 9.4 [22] though these are not reported here.

4.2 Synchrotron Radiation

Electromagnetic radiation is produced when electrons are accelerated. In a synchrotron or storage ring, relativistic electrons (6 GeV at the ESRF) are accelerated in a circular orbit by a series of bending magnets (64 in the case of the ESRF) resulting in a circumference of 844.4 metres. Relativistic effects mean that an intense, highly collimated, beam is emitted in the direction of the electron orbit at a tangent to the storage ring at each bending magnet. At the ESRF, radiation can be used from half these bending magnets. More brilliant radiation can be obtained from insertion devices: undulators and wigglers, in straight sections of the ring. These are the primary radiation source at third generation synchrotron sources, such as the ESRF.

In an undulator, an alternating series of magnets force the electrons in the storage ring to perform a sinusoidal path. The period is such that radiation is emitted in phase and is significantly more intense and well collimated than radiation from a bending magnet. The experiments described in this thesis were performed on beamline ID3 which uses the radiation from an undulator.

Station 9.4 at Daresbury uses another type of insertion device, a wiggler. This uses a very strong magnetic field produced by a superconducting magnet to force the electrons into a single tight curve. Multipole wigglers are used at the ESRF, unlike an undulator however the radiation from successive curves does not add in phase.

The energy of the radiation from an undulator is concentrated in a fundamental and harmonics, the energy of which depend on the beam energy (which is effectively fixed), and the undulator gap which can be changed. A

multipole wiggler cannot produce such intense radiation at lower energies, but at high photon energy is able to produce more intense radiation than an undulator.

Radio frequency cavities are used to restore the energy lost by emitting radiation as the electrons travel round the storage ring.

4.2.1 Brightness, Brilliance and Flux

The usual definitions employed in describing the emission from a SR source are:

$$\text{Flux} = \text{photons s}^{-1}$$

$$\text{brightness} = \frac{\text{photons s}^{-1}}{(\text{unit solid angle})(0.1\% \text{ Bandwidth})}$$

$$\text{brilliance} = \frac{\text{photons s}^{-1}}{(\text{unit solid angle})(0.1\% \text{ Bandwidth})(\text{source size})}$$

In general high brightness is important in experiments without focusing elements, brilliance in those that have such elements [140].

The maximum brilliance from third generation undulators is 10 orders of magnitude greater than from a rotating anode at the K_α line [2] and this has resulted in experiments that were inconceivable 10 or 20 years ago becoming almost routine.

4.2.2 Optics

The photon energy was selected using a sagittally focused double-crystal, Si(111) monochromator [19]. Harmonic rejection was achieved with two mirrors. The undulator gap was set at 20mm, and for the experiments of CO/Ni(110) a photon energy of 17.0 keV (0.7293Å) corresponding to the 5th harmonic of the undulator was used.

	Undulator gap	Harmonic	Photon energy	Wavelength
InSb(001)-c(8×2)	20mm	3rd	10.34	1.20852Å
Ni(110)-(2×1)-2CO	20mm	5th	17.0	0.7293Å

Table 4.1: X-ray wavelength and undulator settings used the in experiments described in this thesis.

In surface diffraction, the choice of X-ray energy is to some extent arbitrary, and is determined by the geometry, and the desire for maximum X-ray flux. Unlike spectroscopic techniques, it is not usually necessary to work at a specific X-ray energy, though absorption edges are usually avoided to reduce the background due to inelastic scattering. To maximise X-ray flux, the minimum undulator gap was used. For the Ni(110)-(2×1)-2CO experiments, the geometry of the diffractometer limited the perpendicular momentum transfer, so the 5th harmonic was chosen. The InSb(001)-c(8×2) experiments used a different diffractometer without this restriction, and the 3rd harmonic was chosen to give a higher resolution in l, the perpendicular momentum transfer vector.

4.3 UHV/HiP chamber

The specially designed UHV/high pressure chamber [7] mounted on a high precision Huber six circle diffractometer with the surface normal vertical (figure 4.1), allowed the preparation by standard surface science methods (argon ion sputtering and annealing in UHV) of single crystal surfaces of good quality. The chamber could then be pressurised to several bars by introducing CO gas, which was purified as described in section 4.3.1. The vacuum chamber had a 2mm thick cylindrical beryllium window, transparent to the high energy X-rays used, which allowed the incoming and diffracted beams to reach the surface and the detector respectively.

A ceramic heating element [17] that is UHV and high-pressure compatible was used to control the sample temperature. The temperature was monitored by a K-type thermocouple in contact with the tantalum sample mounting clips.

The chamber pressure is monitored by a combined Penning / cold cathode gauge mounted near the sample, and a cold cathode gauge near the turbomolecular pump.

Two manual gate valves permit the isolation of the pressurised chamber from the sputter gun and the pumping stage.

4.3.1 Gas Distillation

At high gas pressures, even trace impurities can adsorb preferentially onto clean surfaces. An impurity level of 1ppm of a gas at 1 bar is equivalent to a partial pressure of 10^{-3} mbar. This level of impurity concentration may
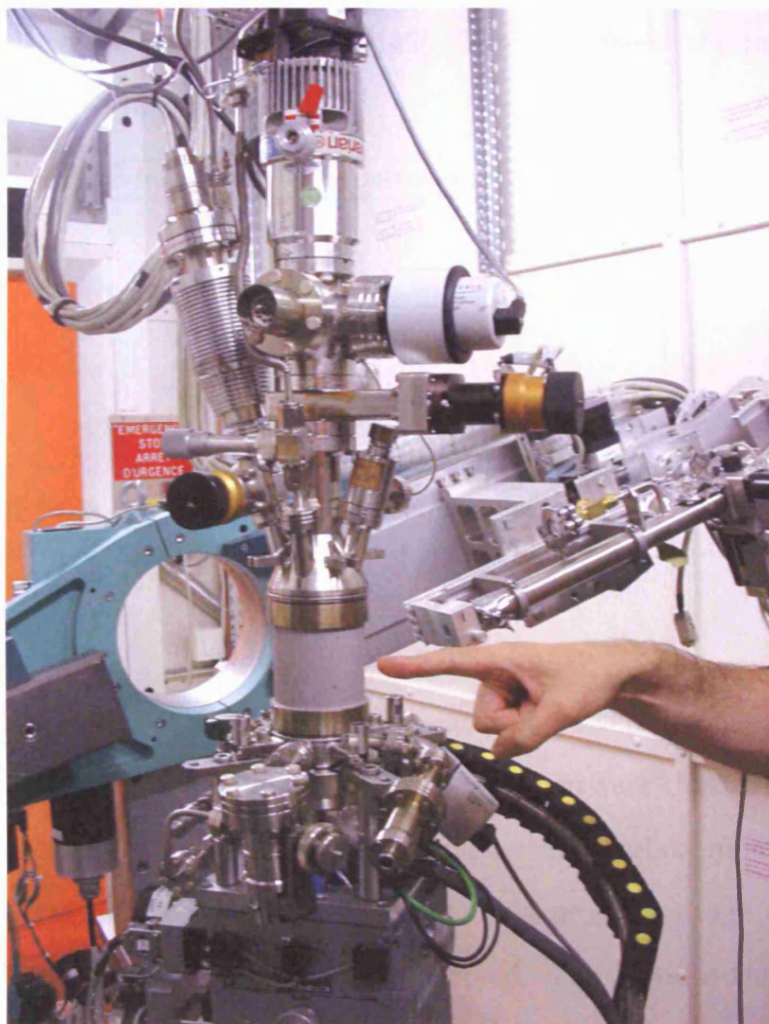
Figure 4.1: UHV/HiP Chamber mounted on diffractometer. The hand gives some idea of scale, and is pointing at the beryllium window.

be completely unacceptable from the point of view of surface cleanliness; it is, for example, 100 times the pressure of CO used to form the (2×1) reconstruction. To obtain a very high purity gas, high purity CO (99.997%, Air Liquide) was further cleaned by a distillation procedure described below based on that described by Yates [145]. Table 4.2 shows the impurities in the gas supplied by Air Liquide.

Impurity	Concentration (ppm volume)
H_2O	3
O_2	3
C_nH_m	2
CO_2	1
N_2	10
H_2	1
Ar	< 10

Table 4.2: Nominal impurity concentrations prior to distillation in 99.997% pure carbon monoxide as supplied by Air Liquide (N47 grade).

The distillation of carbon monoxide was performed in the manifold shown in figure 4.2. The gas manifold contains two reservoirs that can be cooled to 77K using liquid nitrogen. At this temperature, carbon monoxide has a vapour pressure of 0.6 bar. A Pirani/Penning pressure gauge allowed the pressure in the gas manifold to be monitored. The liquid nitrogen dewars can be lowered to warm the reservoirs to permit distillation. A system of valves allow the reservoirs to be isolated from the rest of the manifold.

The distillation procedure was as follows. After pumping the gas manifold, a quantity of carbon monoxide was condensed in reservoir A. The reservoir was then warmed by lowering the dewar of liquid nitrogen, and the

gas distilled into reservoir B. When there was only a little liquid remaining in A, reservoir B was isolated and the manifold pumped to remove higher vapour pressure gases such as hydrogen, and low vapour pressure impurities remaining dissolved in the liquid remaining in reservoir A. Reservoir B was also briefly pumped to remove high vapour pressure gases. Gas pressures above 0.6 bar were possible by lowering the dewar and allowing some carbon monoxide to evaporate.

4.3.2 Sample mounting

In surface diffraction it is very important that the sample is held rigidly, otherwise systematic and random errors will result. In addition, the sample must stand proud of the mounting clips to eliminate scattering from them. The sample was held in place in the UHV/HiP chamber [7] by tantalum clips in slots cut in the side of the sample as shown in figures 4.3 and 4.4. This gave the necessary sample rigidity, and ensured that the sample mounting clips were below the level of the sample. A K-type thermocouple in contact with the sample allowed the measurement of sample temperature.

Sputtering

Argon ion sputtering was used to clean the Ni(110) and InSb samples. In the former case, it was necessary to use a bias voltage to increase the sputter current. A commercial sputter gun, of the filament type rather than a cold cathode design, was used.
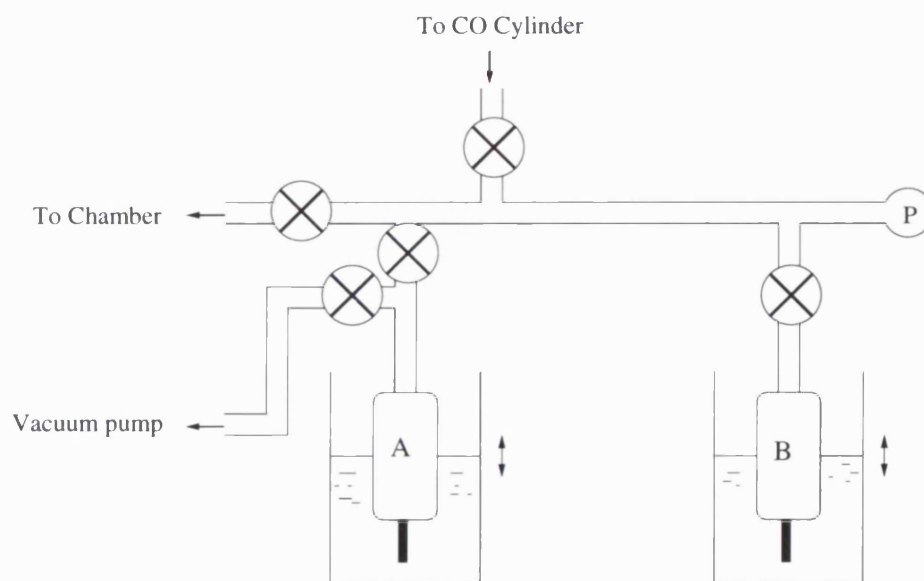
Figure 4.2: The gas manifold. Reservoirs A and B can be submerged in a dewar of liquid nitrogen which can be raised and lowered allowing the gas to be distilled. The pressure is measured by a Pirani/Penning gauge, P

Ta mounting clip

Ni Sample

8mm

Plan View (above)

Side View (below)

Diameter 8mm

Ta mounting clip

Sample
thickness
3mm
(approx)
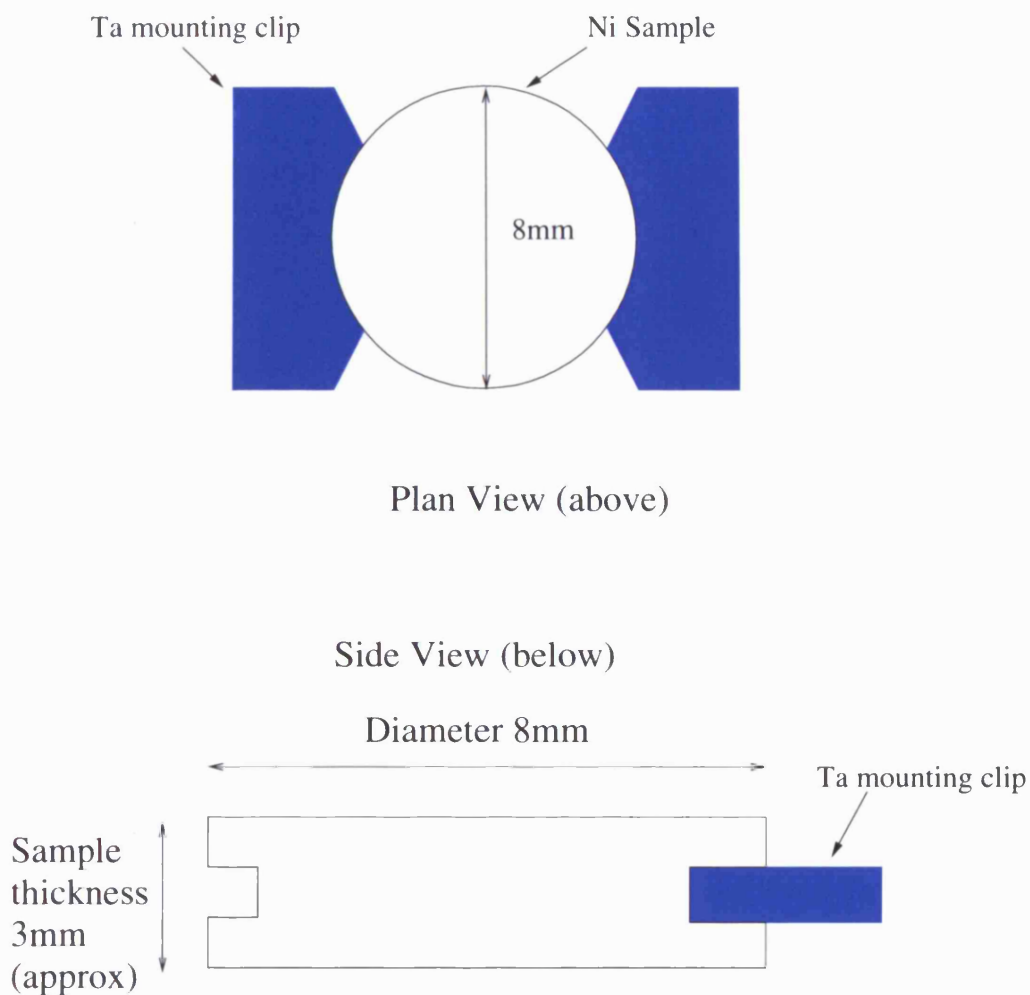
Figure 4.3: The Nickel (110) sample is held in place by tantalum clips inserted into slots cut into the side of the sample. This arrangement allows the surface to stand proud of the sample mounting, a necessity for surface diffraction
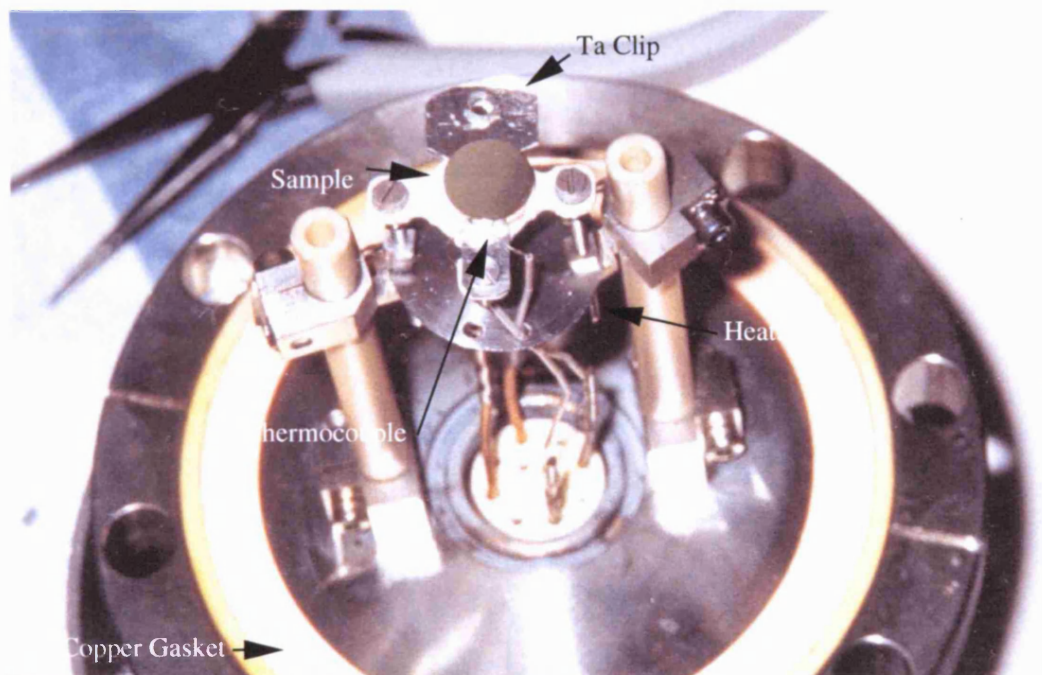
Figure 4.4: Ni(110) sample (centre top) mounted using Ta clips to baseplate of UHV/HiP chamber. Thermocouple wires can also be seen in contact with the sample. A heatshield can be seen below the sample. Also visible is the copper gasket for the UHV/HiP seal
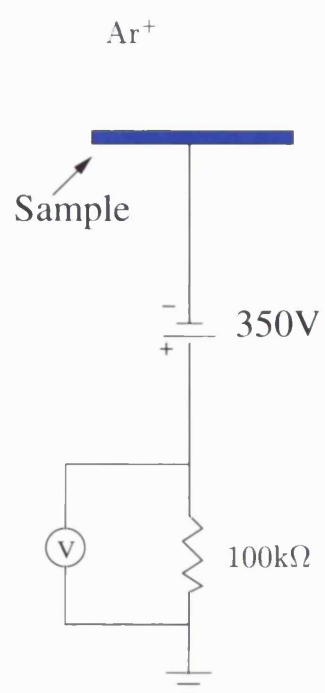
Figure 4.5: Argon ion sputtering with bias voltage. The sputter current is calculated from the voltage drop across the 100 kΩ resistor.

4.3.3 Sample surface preparation

A high purity (99.995%) nickel (110) crystal (supplied by Surface Preparation Laboratory, The Netherlands) was used for the experiments described in this thesis. The surface miscut was less than $0.1°$. After a final 0.05 micron polishing step, the surface roughness was less than 0.03 micron [67].

The sample was initially cleaned by cycles of argon ion sputtering and annealing as described in section 4.3.2. After this cleaning, LEED showed sharp diffraction spots, and no traces of carbon, oxygen or sulphur could be detected in the X-ray photoemission spectrum.

Three periods of beamtime were used for the experiments of CO on Ni(110). Before each experiment, the chamber was baked for at least 24 hours, then the filaments and sample heater were outgassed. The mass spectrometer was used to check for leaks.

For the first experiment, the chamber was baked for 48 hours, and then leak-checked. After the bakeout, the pressure dropped to 5×10^{-9} mbar, though a base pressure of 5×10^{-10} mbar was eventually achieved. The Ni(110) crystal was then cleaned for several hours by cycles of argon bombardment at an energy of 2keV. A sample bias of -300V was used to increase the sputter current to 1-2μA. Immediately after sputtering, the sample was annealed at $800°$ C for 3 minutes.

After heating in CO, the surface reconstruction was destroyed, so at several points within the beamtime, it was necessary to re-prepare the surface. This was done by argon bombardment followed by annealing. On the occasions when CO had been introduced to the chamber, significant outgassing

occurred on heating the sample. If this outgassing occurred, a second sputter of 10 minutes followed by annealing to 800° C was performed as this was found to give a more ordered surface and more intense reconstruction. After this heating it was necessary to realign the sample on the diffractometer.

To prepare the (2×1) reconstruction, CO was introduced when the temperature fell below 500° C while the sample was cooling from the final anneal. The pressure stabilised at 5×10^{-6} mbar in flow mode by the time the sample cooled to 400° C.

The apparatus used could not directly measure the surface cleanliness of the nickel crystal. To give some idea of the quality of the surface, the width and integrated intensity of the (1 0 0.1) and (0 1 0.1) peaks were measured, as they indicate surface order, and impurities disrupt the surface order. The peak width of both of these peaks was 0.1° which corresponds to a surface correlation length of 320Å and 225Å respectively. These figures are not directly comparable with those for fractional order peaks as there is a contribution from roughness and disorder in the bulk. The narrower and more intense the peak however, the better the surface quality.

4.3.4 Support rods

The chamber is fitted with removable reinforcing rods to support the beryllium window during transport. While preliminary experiments left some of these support rods in place, they block approximately 5° of the incoming or outgoing beam. While this seems a relatively small amount of reciprocal space obscured, the effect is significantly worse as it affects the incident and

exit beams; also the chamber, and hence reinforcing rods, rotate with the sample when rocking scans, which can span several degrees, are performed to measure the integrated intensity of reflections. Scanning a CTR without gaps in l is particularly difficult as the chamber must rotate slightly as l is increased to maintain the diffraction condition. To eliminate this problem, the support rods were removed for subsequent experiments.

4.4 UHV Chamber

4.4.1 The need for UHV

Surface science experiments make use of ultra high vacuum (UHV) conditions to ensure that the surface remains clean and free from contamination. At a pressure of 10^{-6} mbar 1 monolayer of CO arrives on a surface in around five seconds, at a pressure of 10^{-10} mbar, the monolayer arrival time is approximately 10 hours. UHV conditions are therefore used to ensure the surface remains unchanged throughout the experiment.

4.4.2 Chamber

The chamber used for the $InSb(001)$-$c(8\times2)$ experiment is described by Ferrer and Comin [35] and shown in figure 4.6. A fast entry lock allows samples to be inserted into the chamber without venting. Beryllium windows allow the entrance and exit of X-rays at incident and exit angle up to 45° to the surface normal, and an in-plane scattering limited to a maximum of 150°.
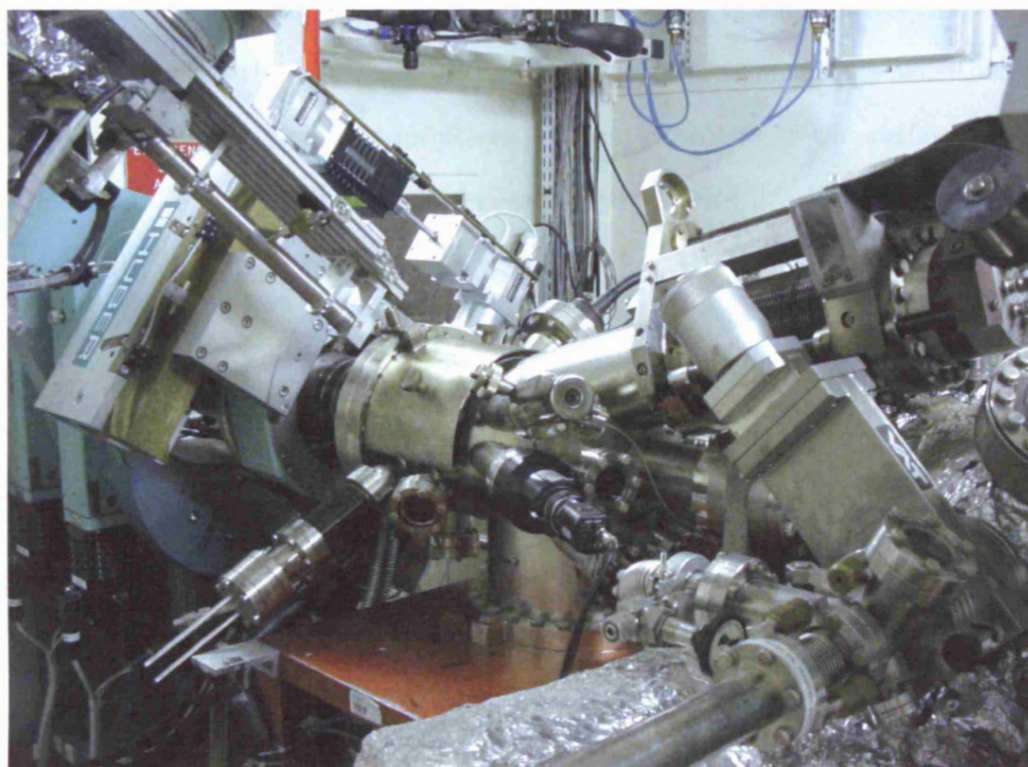
Figure 4.6: The UHV chamber on ID3

4.4.3 Auger Electron Spectroscopy

Auger Electron Spectroscopy (AES) was used to monitor the level of impurities (carbon in particular) in the experiment on the indium antimonide surface.

In Auger electron spectroscopy, high energy electrons from an electron gun ionise atoms in the sample. An electron from a higher energy level falls into the resulting vacancy in the lower shell causing an electron to be emitted with a characteristic energy. The technique is surface sensitive, as these Auger electrons can only escape from atoms near the surface of the material. The resulting characteristic spectral lines are tabulated for each element.

4.5 X-Ray measurements

4.5.1 Diffractometer

The diffractometer used for the experiments on the CO/Ni(110) system was a six-circle Huber diffractometer as pictured in figure 4.1. The diffractometer circles are shown schematically in figure 4.7. The sample normal is vertical, thus in-plane scattering is in the horizontal plane. The diffractometer geometry is identical to the 6-circle diffractometer described by Vlieg [125], except that Vlieg's paper describes a diffractometer with the sample normal being horizontal.

For the InSb(001) experiment, a diffractometer with a UHV system described by Ferrer and Comin [35] was used. This diffractometer geometry
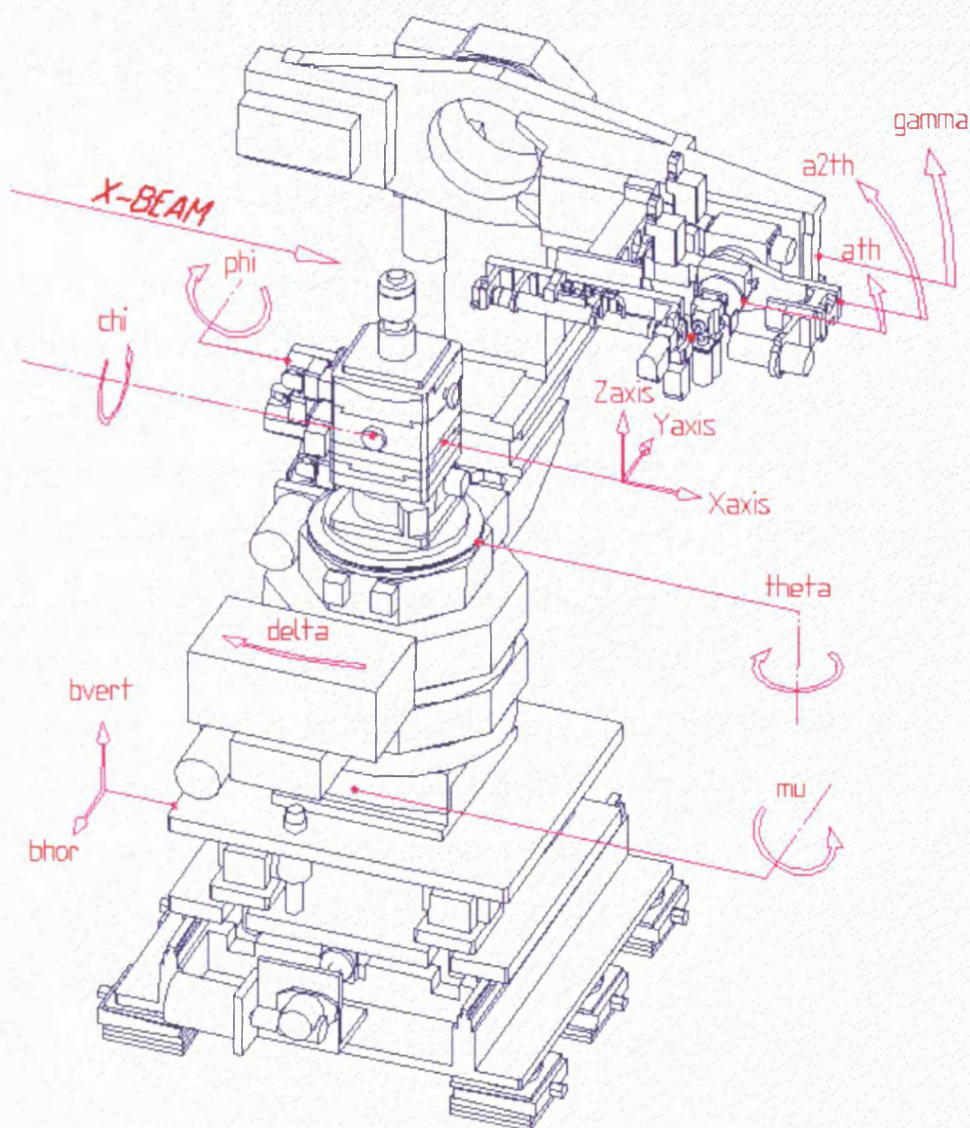
Figure 4.7: Schematic of vertical axis diffractometer showing motor names. This diffractometer was used for the Ni(110)-(2×1)–2CO experiments

has the sample normal horizontal, so in-plane scattering is predominantly vertical. The gamma arm is on a linear stage, so an additional correction factor of $\cos(\gamma)$ is necessary to correct the data when compared to the paper of Vlieg [125].

4.5.2 Sample alignment and Data collection

The sample surface is aligned so that it is perpendicular to the theta axis by adjusting the phi and chi arcs of the diffractometer. This was performed using a laser for the InSb sample, and the X-ray beam for the nickel sample. The sample is then crystallographically aligned by determining the orientation of the sample at two Bragg peaks. This allows the diffractometer control software, SPEC [108], to move the sample and detector to a particular point in reciprocal space. The diffractometer was controlled by SPEC software running on a Hewlett-Packard workstation. Two different types of scan were used in the experiments, a reciprocal space scan, where the diffractometer scans along a reciprocal lattice vector (such as h); the other scan type was a rocking scan, where the sample was rotated around the surface normal by rotating the diffractometer θ axis.

Chapter 5

SXRD - Data analysis techniques and programs

Data analysis takes place in two stages. First, the raw X-ray scans (eg figure 6.4) are integrated and corrected for the geometrical and resolution factors to obtain a set of integrated intensities. A structural model is then fitted to these integrated intensities (eg fig 6.10 and 8.13).

5.1 Programs used

Data analysis was performed using a suite of programs written by Elias Vlieg. The programs are written in the C programming language originally for use under DOS. There are significant memory and other limitations to this approach however and a Unix port using the PGPLOT graphics library [95] was written by Paul Howes.

Part of the work in this thesis has involved modifying Howes's version to

compile using more recent versions of the libraries; a number of improvements and bug fixes by Vlieg were also incorporated. The ESRF now distribute a version derived from this work [128], and it is this version that was used in the analysis of the data. Extensions to these programs to facilitate display of structures, and to add corrections for monitor dark counts were developed in the course of this thesis work and are described later in this chapter.

Program	Use
DIF	Crystallographic alignment
ANA	Geometric and resolution correction factors, fitting and Integration of peaks to generate structure factors
AVE	Averaging of symmetry equivalent peaks
ROD	Fitting model to structure factors

Table 5.1: Surface X-ray diffraction analysis programs written by Vlieg and used in the data analysis.

5.1.1 DIF - Crystallographic alignment

DIF was only used in some preliminary studies at Daresbury, and is mentioned here for completeness. In a surface X-ray diffraction experiment, the sample surface normal is found by using a laser alignment procedure on the diffractometer. After this, a crystallographic alignment is carried out by finding the position of several bulk Bragg peaks. DIF is then used to calculate an orientation matrix (also called a UB matrix) that describes the orientation of the sample on the diffractometer. For the experiments carried out at the ESRF however, most of this functionality was built into the "spec" software, so it was not necessary to use DIF.

5.1.2 ANA - Correction factors

It is necessary to integrate the measured data, and apply a number of geometrical and resolution corrections, in order to calculate structure factors. To perform the corrections described by Vlieg [125], the computer program ANA [124] was used. The correction factors are summarised by equation 5.1, and the formulae used in the error calculation are given in appendix C.

$$C_{tot} = P L_\omega C_{rod} C_{area} C_{beam} \qquad (5.1)$$

The total correction factor C_{tot} is made up of a corrections for the beam polarisation, P, the Lorentz factor L_ω, cut of the rod C_{rod}, active sample area C_{area}, and a correction for the beam profile, C_{beam}.

The Lorentz factor, L_ω, results from the conversion of angular integration variables from real to reciprocal space. The cut of the rod correction C_{rod} takes into account the intersection of the crystal truncation rod with the Ewald sphere.

Polarisation

The correction for polarisation, P, is given in section 3.2.2. For all the experiments described in this thesis, the X-ray beam was completely polarised in the horizontal plane. For the experiments on Ni(110)-(2×1)-2CO, the sample normal was vertical, and for the InSb(001)-c(8×2) experiments, the sample normal was horizontal due to the different diffractometers used. Because of this, the polarisation correction differed for the two experiments.

Area Correction Factor

The area correction factor corrects for the active surface A - the area on the surface that is illuminated by X-rays and visible to the detector. This area is determined by the sample size, and by slits s_1 and s_2 close to the sample.
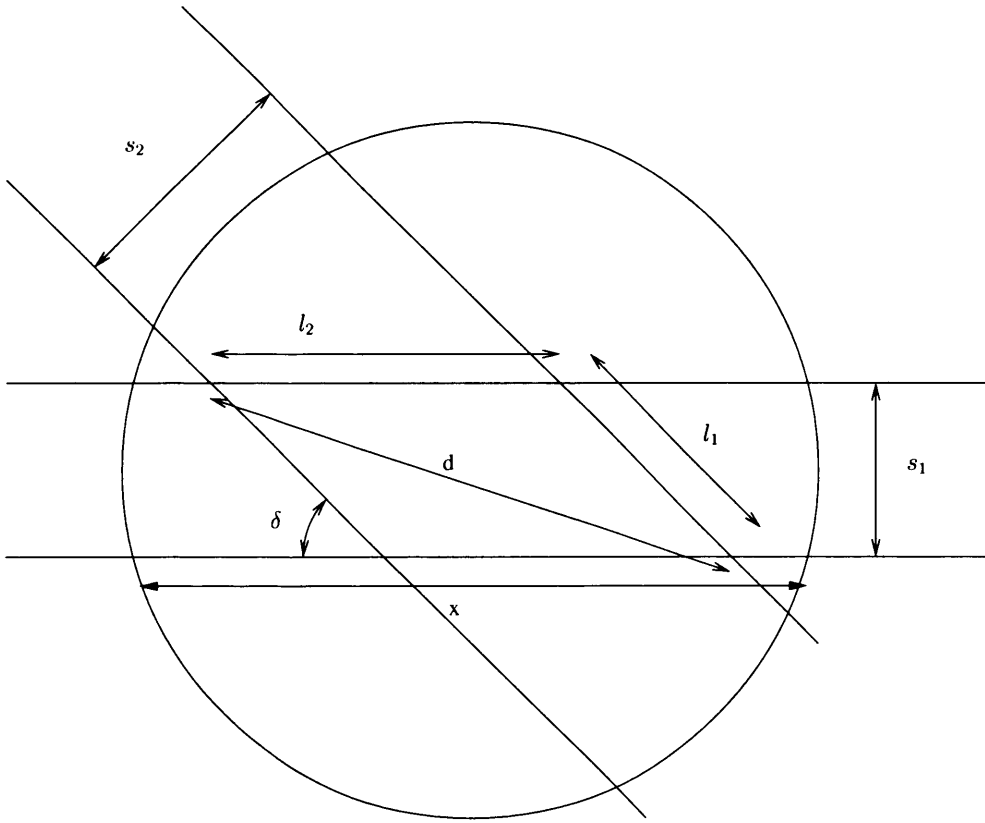
Figure 5.1: Area of beam on sample

$$l_1 = \frac{s_1}{\sin \delta}, \qquad l_2 = \frac{s_2}{\sin \delta}$$

$$d = \sqrt{l_1^2 + l_2^2 - 2l_1 l_2 \cos(180 - \delta)}$$

$$\Rightarrow d = \frac{\sqrt{s_1^2 + s_2^2 + 2s_1 s_2 \cos \delta}}{\sin \delta} \tag{5.2}$$

This formula differs from that given by Feidenhansl [34] by a factor of two. The formula given above however is clearly correct given $\delta = 90°$. The formula given by Feidenhansl is correct for the radius, and this discrepancy does not influence the final result of Feidenhansl.

Beam profile correction

For a large sample, and small slits settings, the area of beam visible to the detector will lie entirely on the sample. At low diffraction angles and wide slits however this is not necessarily true, and an additional correction factor is necessary. This correction is also necessary if the intensity of the out of plane component of the beam varies significantly, more likely with third generation sources, resulting in variation in intensity with distance x along the sample. The procedure implemented by Vlieg in ANA [124, 125] also takes into account the horizontal and vertical profile of the beam, and uses numerical ray-tracing to determine the illuminated area visible to the detector.

For the experiments on Ni(110)-(2×1)-2CO described in chapters 6 and 7 the active area extended off the sample, and this numerical beam profile correction was used for all the reflections.

For the InSb(001)-c(8×2) experiments described in chapter 8 however the active sample area was defined by the beam footprint rather than the slits, so an analytic calculation of the area is sufficient.

As with all numerical integrations, it is possible that errors will be introduced by rounding errors or by the sampling procedure. To check the former, the numerical precision of the sampled points was increased by changing from

(a) Beam Width (FWHM=0.8mm)   (b) Beam Height (FWHM=0.4mm)
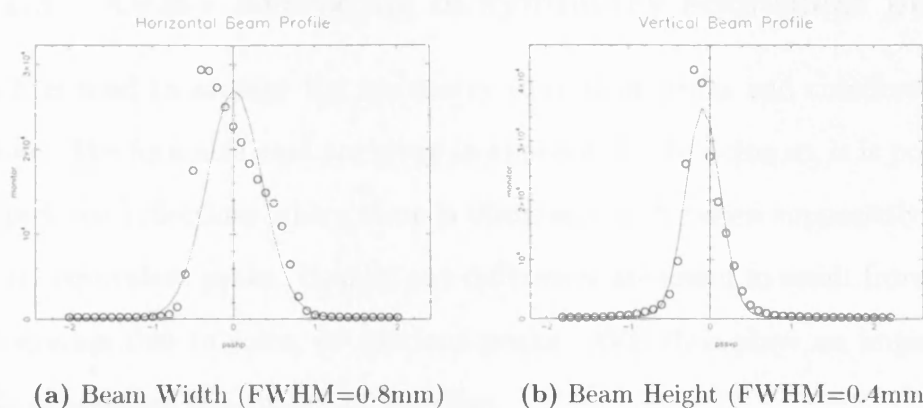
Figure 5.2: Gaussian fits (solid line) to the measured profile of the incident X-ray beam for CO/Ni(110) experiments.

single precision to double precision floating point numbers. This made no difference to the final correction factors, so they are not limited by numerical precision. Increasing the number of sampled points by a factor of four resulted in a change in correction factor of less than 1%. The numerical errors will therefore be insignificant when compared to the experimental errors.

It is possible, though complex, to calculate the active sample area analytically. While in theory this method may seem to be more accurate, current implementations do not take into account the beam profile and so may end up being less accurate. In addition, the analytical calculations consist of a large number of special cases of the geometry, some of which will be used very infrequently, this makes it much more difficult to test all the cases, and is more likely to lead to obscure errors in the calculations. Analytical calculations can however be significantly faster.

5.1.3   AVE - Averaging of symmetry equivalent peaks

AVE is used to average the symmetry equivalent peaks and combine their errors. The formulae used are given in appendix D. In doing so, it is possible to pick out reflections where there is disagreement between supposedly symmetry equivalent peaks. Usually any differences are found to result from poor integration due to noise, or spurious peaks. AVE thus plays an important role in ensuring the quality of the data.

5.1.4   ROD - Structure fitting

The program ROD [127] is used in this thesis to fit a model to the measured structure factors using the theory in chapter 3 and given by Vlieg [129] and also by Robinson [101]. ROD is able to calculate the Patterson function, and plot comparisons between experimental structure factors and those calculated from a model. A manual for rod is also available [123].

5.2   Extensions to analysis programs

As part of the research, modifications have been made to the data analysis programs. The author has written an extension to ANA to correct for an off-set in the beam monitor, and also an interface between ROD and the graphics program rasmol [104] to allow easy visualisation of surface structures. These extensions would not have been possible without the source code for ROD and ANA. Details of these extensions are given below.

5.2.1   ANA-Monitor Dark current correction

As the current in the storage ring decreases over time, the incident X-ray flux decreases. To correct for this, detector counts are normalised to an ion chamber monitor.

There is often a small dark current in the monitor. In the Ni(110)-(2×1)– 2CO experiments on ID3, for example, this was approximately 400 monitor counts s^{-1} with no beam. This is small compared with the values with beam given in table 5.2.

Date	Filling Mode	Current (mA)	Monitor counts s^{-1}
June 2000	16 bunch	90 - 60	21 000 - 16 000
Sept 2000	$2 * \frac{1}{3}$	200 - 175	74 000 - 67 000

Table 5.2: Comparison of monitor counts in different filling modes with beam current. The two values given for current and monitor counts are just after, and just before a refill.

The smallest count rate here will give a systematic error smaller than 3% when normalising to the monitor counts. This is probably within the range of the other systematic errors in alignment, so has usually been neglected.

In some of the scans, however, beam instabilities (possibly due to problems with the monochromator stabiliser), caused the counting time to vary widely (from 0.5 to 24 seconds in one case for the same number of monitor counts). I have added a correction for this effect to ANA. In growth experiments where a particular position in reciprocal space is monitored, this correction is particularly important, as the systematic error may introduce oscillations that cannot be distinguished from growth oscillations. This is not however relevant to the experiments described here.

$$I_{corrected} = I\frac{M_{norm}}{M(1 - \frac{M_{dark}}{M})} \tag{5.3}$$

In equation 5.3 $I_{corrected}$ is the corrected number of counts, I is the measured number of counts, M_{dark} is the monitor count rate with no beam (ie the dark count rate), M is the measured monitor count rate and M_{norm} is an arbitrary normalising factor usually chosen so that $\frac{M_{norm}}{M} \approx 1$. As a rule, $\frac{M_{dark}}{M}$ is small, so equation 5.3 reduces to:

$$I_{corrected} = I\frac{M_{norm}}{M} \tag{5.4}$$

5.2.2   Rasmol extensions to ROD

ROD is well established as a program for fitting surface X-ray diffraction data. As part of this thesis, an extension to ROD that allows it to make use of the molecular graphics package rasmol [104] to visualise in 3d the surface structure (and optionally the bulk) has been written. Visualisation of the structure in a molecular graphics package can quickly rule out physically

unreasonable structures, and can enable errors in entering a model to be rapidly discovered. As well as loading a file into rasmol, the extension allows ROD to issue commands to rasmol enabling, for example, incorporation of those commands into ROD macro files.

This extension has been incorporated into the experimental version of ROD distributed by the ESRF [128] and instructions for use are available from the same web site [132].

Details of Implementation

ROD first saves the surface structure to a temporary file (defined by the ext.wal.set.rasmol.filename) in xyz format. A function modified from an original version by Svensson was used for this, and it is possible to specify the number of repeat units of the unit cell. ROD then sends commands to rasmol to load this file using BSD[1] style network sockets [83].

Usually, rasmol and ROD will run on the same machine, but this is not necessary. It may, for instance, be desirable that ROD runs on a fast server to quickly perform calculations, but that rasmol runs on the local machine for fast interactive graphics. This is possible, though the machines must share a filesystem to support this.

Limitations and Further Work

Currently, the Windows version of rasmol does not support BSD network sockets, so it is not possible to use the extension under Windows. Due to limitations in rasmol, it is not currently possible to send the surface structure

---

[1]Berkley Software Distribution, a "flavour" of UNIX

file to rasmol over the network. Currently therefore ROD and rasmol must have a shared filesystem, though they may run on different computers. It is hoped that modifications will be made to rasmol to lift these restriction in the future.

Chapter 6

The CO/Ni(110) reconstruction at a pressure of 2.3 bar

This chapter describes experiments to determine the changes that occur to the (2×1) reconstruction of carbon monoxide (CO) adsorbed on the (110) surface of nickel as the pressure is raised from the UHV conditions to a pressure of 2.3 bar. The chapter will show that, at room temperature, the structure at high pressure is identical to that at UHV, within experimental accuracy. In addition, the assignment of CO to the short bridge sites of recent experiments [50, 76, 91, 103, 115, 147] is confirmed, and the atomic coordinates are defined to within 0.02Å. These results are more accurate than, though within the errors of previous results.

The results have been published in Physical Review Letters [100].

6.1 Background

As discussed in chapter 2, studies of catalyst surfaces are performed to provide an insight into the factors that affect catalyst performance, and ultimately lead to the manufacture of better catalysts.

Previous *in-situ* experiments looking at the effect of high pressure gas–surface interactions have used STM or SFG. Surface X-ray diffraction (SXRD) is complementary to these techniques as it can provide detailed structural information. No previous experiment has studied the Ni(110) surface under high pressures of CO.

At saturation coverage on Ni(110), CO forms a *p2mg* (2×1) structure. A similar structure is formed on the (110) surfaces of Ir, Pd, Pt and Rh [76]. There is a general consensus that the structure of the overlayer is a zig-zag arrangement of CO molecules along the $[1\bar{1}0]$ axis alternately tilted to one side and the other along the [001] direction [76]. The determination of the adsorption site has proved more controversial, though recent studies by LEED [50, 147], photoelectron diffraction [76], SXRD [103] and STM[115] have concluded that the adsorption site is the so called short bridge site as shown in figures 6.1 and 6.2.

The *p2mg*(2×1) reconstruction can be prepared at low temperatures by simply dosing with carbon monoxide, but at higher temperatures it exists in equilibrium with the gas [52, 103, 137]. The effects on this structure of both increasing and decreasing the pressure were measured.

Previous experiments on a similar system, CO/Au(111) [98], found a rapid degradation of the surface reconstruction at 20 mbar in the presence
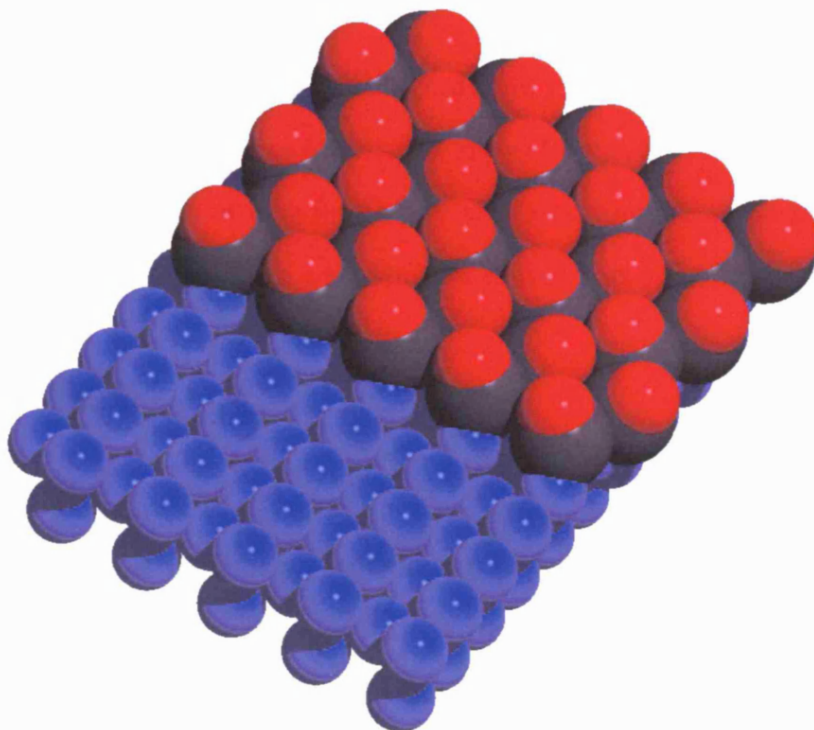
Figure 6.1: Model of the *p2mg* (2×1) reconstruction of CO on Ni(110) with CO in short bridge sites as proposed previously and refined by this study. Half the surface is covered by the reconstruction, and half is the bare Ni(110) surface. Nickel atoms are blue, oxygen red and carbon black. Each atom is represented by a sphere of their van der Waals radius.

Multiplicity	Wyckoff letter	Site Symmetry	Position
4	d	1	(x,y) $(\bar{x},\bar{y})$ $(\bar{x}+\frac{1}{2},y)$ $(x+\frac{1}{2},\bar{y})$
2	c	.m.	$(\frac{1}{4},y)$ $(\frac{3}{4},\bar{y})$
2	b	2..	$(0,\frac{1}{2})$ $(\frac{1}{2},\frac{1}{2})$
2	a	2..	$(0,0)$ $(\frac{1}{2},0)$
asymmetric unit cell $0 < x < \frac{1}{4}$ and $0 < y < 1$			

Table 6.1: Symmetry positions in the *p2mg* plane group

of an X-ray beam, but that this degradation could be virtually eliminated by biasing the sample to +300V with respect to the chamber walls. This could have been due to ions formed by the beam impacting on the surface. A similar biasing procedure was adopted during this structural study.

6.1.1 Lattice

Symmetry

Knowledge of the symmetry of a reconstruction significantly reduces the parameters that need to be fitted in the model. The systematic absence of reconstruction peaks along the (10) direction is characteristic of a glide plane and the (2×1) reconstruction has *p2mg* symmetry, a subgroup of the *p2mm* symmetry of the nickel (110) surface. The corresponding site symmetry of general and high symmetry positions [48] is listed in table 6.1 and illustrated in figure 6.2.

6.1.2 Coordinate transforms

For the analysis of the diffracted intensity, the atomic structure of the Ni(110) surface was described by a tetragonal unit cell defined by three base vectors

a_i, and corresponding reciprocal lattice vectors b_i. Using this convention a_1 and a_2 are in the surface plane, and a_3 is perpendicular to the surface. The vectors are related to the conventional face centred cubic cell by:

Real space: Reciprocal space:

$$a_1 = \tfrac{1}{2} \ [\bar{1}10]_{cubic}$$
$$a_2 = \quad [001]_{cubic}$$
$$a_3 = \tfrac{1}{2} \ [110]_{cubic}$$

$$b_1 = \quad (\bar{1}10)_{cubic}$$
$$b_2 = \quad (001)_{cubic}$$
$$b_3 = \quad (110)_{cubic}$$

with   with

$$|a_1| = |a_3| = \frac{a_0}{\sqrt{2}} = 2.492\text{Å}$$
$$|a_2| = a_0 = 3.524\text{Å}$$

$$|b_1| = |b_3| = \frac{2\sqrt{2}\pi}{a_0} = 2.521\text{Å}^{-1}$$
$$|b_2| = \frac{2\pi}{a_0} = 1.783\text{Å}^{-1}$$

6.2 Experimental

The experiments were performed on the Surface Diffraction beamline of the ESRF (beamline ID3) [35]. A photon energy of 17.0 keV (corresponding to a wavelength of 0.7293Å) was selected using a sagittally focused double-crystal Si(111) monochromator [19], with harmonic rejection being performed by two mirrors. The Ni(110) crystal was mounted in an Ultra High Vacuum/High pressure chamber (UHV/HiP) chamber [7] which in turn was mounted on a Huber high precision vertical z-axis 6 circle diffractometer. The details of the instrument are described in chapter 4 and elsewhere [35].

The experiments were carried out with an angle of incidence of 0.74°, this is approximately four times the critical angle at this wavelength. For
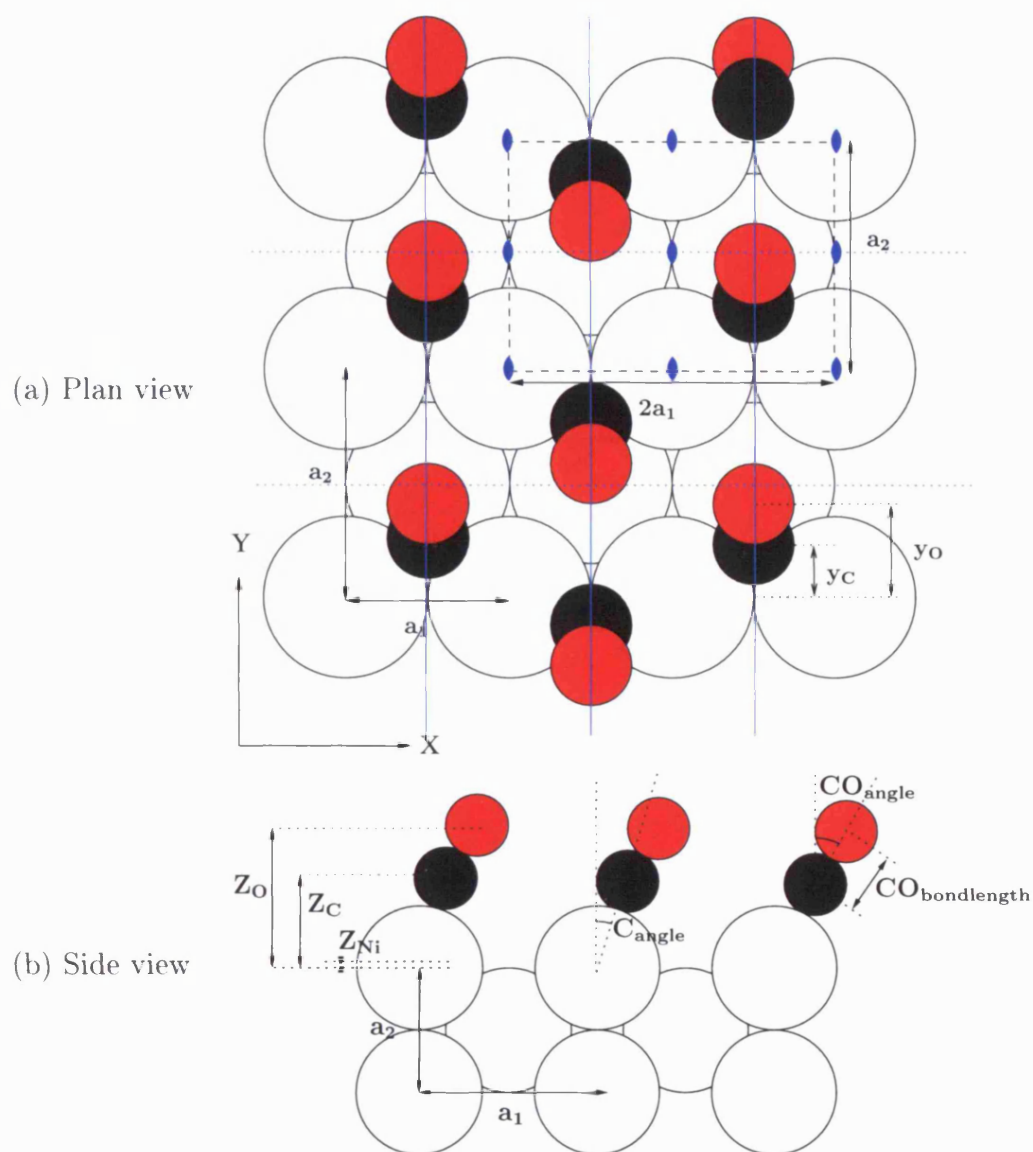
Figure 6.2: Surface structure of Ni(110)-(2×1)–2CO reconstruction. The unit cell of the reconstruction is shown by the dotted rectangle in (a). Oxygen (top layer) is denoted by red circles, carbon (2nd layer) by black circles, nickel atoms by open circles (3rd and 4th layer). Symmetry elements of the $p2mg$ symmetry are in blue - Mirror lines are denoted by solid blue lines, glide lines by dotted blue lines and twofold rotations by blue ovals. Possible alternative adsorption sites are depicted in figure 2.2
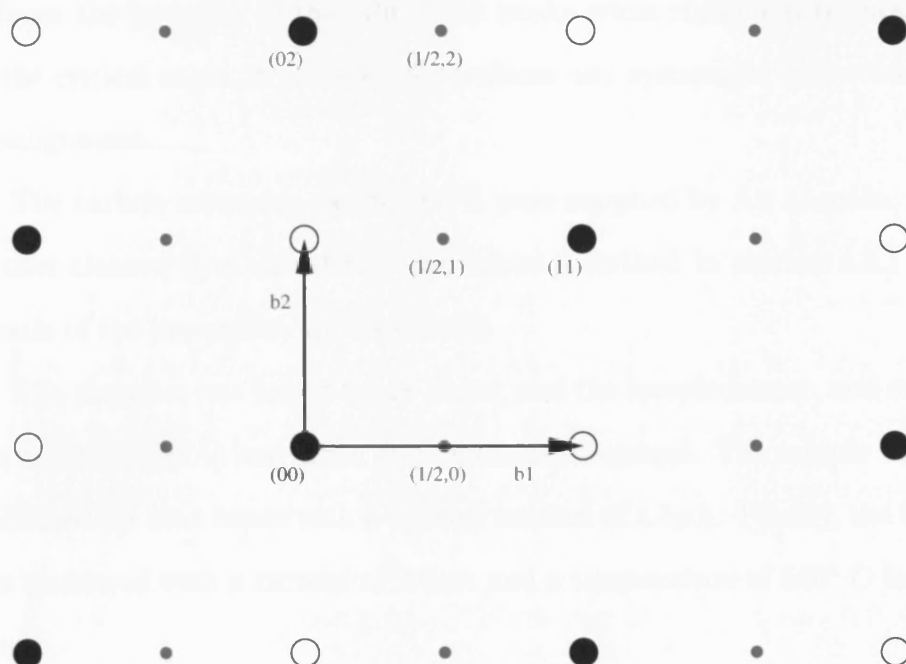
(a) In-plane (h k 0) Reciprocal space for Ni(110). The large circles correspond to the bulk CTRs (filled with a peak at l=0, open with a peak at l=1). The small green circles mark the additional points due to the (2×1) reconstruction.
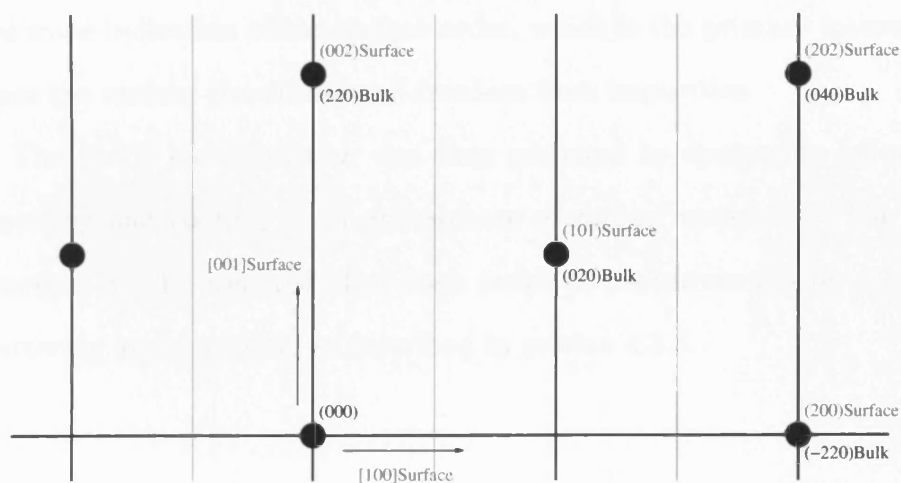
(b) Crystal truncation rods (black lines) and (2×1) reconstruction rods (green lines) in the (h 0 l) plane. Bragg peaks are marked by black circles and are labeled in bulk (black) and surface (blue) notation

Figure 6.3: Ni(110)-(2×1)–2CO Reciprocal space

the *in-plane* peaks, the exit angle is approximately the same. While this reduces the intensity of the diffraction peaks when compared to measuring at the critical angle, it considerably reduces any systematic error caused by misalignment.

The carbon monoxide was 99.997% pure supplied by Air Liquide. It was further cleaned by a distillation procedure described in section 4.3.1 where details of the impurities are also listed.

The chamber was baked for 48 hours, and the sample heater, and residual gas analyser (RGA) and argon gun filaments outgassed. The sample was then sputtered for nine hours with a sputter current of 1.3μA. Finally, the sample was sputtered with a current of 2.6μA and a temperature of $500°$ C for eight hours.

The chamber is not equipped for Auger electron spectroscopy, or other technique to directly measure the surface cleanliness, so the width and integrated intensity of the (1 0 0.1) and (0 1 0.1) peaks were measured. These give some indication of the surface order, which is the primary interest, and hence the surface cleanliness and freedom from impurities.

The (2×1) reconstruction was then prepared by sputtering followed by annealing and cooling in an atmosphere of carbon monoxide. The reconstruction was re-prepared after each series of measurements by a cycle of sputtering and annealing as described in section 4.3.3.

6.2.1 Results

Effect of Pressure

The effect of reducing the carbon monoxide pressure was measured by preparing a fresh (2×1) reconstruction, and monitoring the intensity of the $(\frac{1}{2}1\frac{1}{10})$ peak. Initially, the CO pressure was 7.3×10^{-8} mbar in flow mode. The CO pressure was reduced by shutting the leak valve and letting the gas pump away; it was then increased by opening the leak valve again. As it was not possible to control the leak valve remotely, it was necessary to turn off the X-rays to enter the experimental hutch and change the pressure, resulting in breaks in the measurement.

The effect on the reconstruction of increasing the CO pressure was studied by monitoring a freshly prepared (2×1) reconstruction as the CO pressure was increased from 10^{-5} mbar to 2 bar in 5 steps. The $(\frac{1}{2}1\frac{1}{10})$ reconstruction peak was measured at each pressure step (figure 6.7).

To test the effectiveness of the bias in preventing the rapid damage to the surface reconstruction observed in previous experiments [98], the peak intensity of the $(\frac{1}{2}1\frac{1}{10})$ reconstruction peak was monitored for five minutes with a +300V bias applied, and then a further five minutes with no bias (figure 6.9).

Structural study of (2×1) reconstruction

A fresh (2×1) reconstruction was prepared as described in section 4.3.3 at a CO pressure of 5×10^{-5} mbar. A data set consisting of 46 in-plane reflections resulting in 16 non-equivalent reflections, four crystal truncation

rods and two fractional order rods was then measured. This represented the low pressure data set. The pressure was then raised to 2.3 bar of CO, and the measurements were repeated to produce a high pressure data set. This method should eliminate any differences due to preparation of the reconstruction, and allow a direct comparison of the two structures.

Diffracted intensities were measured by setting the crystal and detector to fulfil the diffraction condition and then rotating the crystal around the diffractometer θ axis (corresponding to a rotation about the sample surface normal).

6.2.2 Peak Integration and fitting method

Analysis of the results takes place in two stages. First, integrated intensities were obtained from the area under the peak. Structure factors are calculated from these integrated intensities by applying the appropriate geometrical and resolution correction factors [125] and taking the square root. A structural model is fitted to these structure factors by a least squares minimisation procedure.

Integrated intensities were obtained by fitting a Lorentzian peak with a linear background to each scan using the computer program ANA ([124] and chapter 5). Given the excellent fit of a Lorentzian to the $(\frac{1}{2}1\frac{1}{10})$ reconstruction peak shown in figure 6.4, the analytic integral of the Lorentzian was used for the integrated intensity. This procedure produced more reproducible results across scans with different numbers of points. To ensure that the same procedure was followed for each peak a "macro" was written to fit all the

peaks in the same manner with the peak width, centre, height of background

and slope of background unconstrained. The results were then examined, and

for a few weak peaks it was necessary to constrain the peak width and peak

centre in order to get a fit that represented the data. ANA also calculated

the structure factors from these integrated intensities by correcting for the

geometric and resolution correction factors described by Vlieg [125].

Lorentzian fit to (0.5 1 0.1) peak
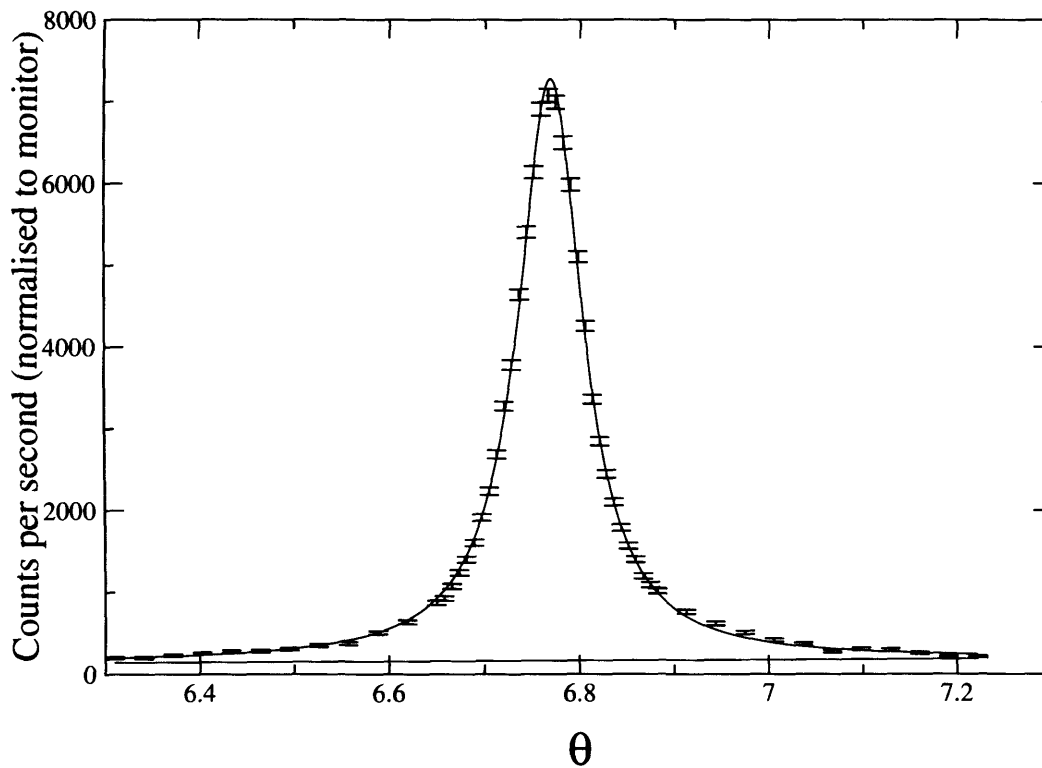
Figure 6.4: ($\frac{1}{2}$10.1) reconstruction peak at 2.3 bar. The Lorentzian and background (solid lines) fitted to the peak shows clearly that the peak has a Lorentzian shape.

6.3 Results and Discussion

6.3.1 Clean Ni(110) surface

Surface contamination results in a disruption of the long range order on the surface. This disruption leads to broader and less intense diffraction peaks which are more difficult to measure accurately. Previous experiments on nickel surfaces have found them particularly sensitive to contamination [52]. Auger electron spectroscopy is often used to measure surface contamination, but as indicated in chapter 4, it was not fitted to the apparatus used in this experiment.

The width of a diffraction peak is determined by a number of factors. For a reconstruction peak, the main effects are correlation length on the surface and mosaicity. The instrumental broadening due to the coherence length of the beam is small. For ordered crystals and highly collimated monochromatic incident X-ray beams, the width of the diffracted peak is inversely proportional to the correlation length on the surface, as described in section 3.3.1. On the clean Ni(110) surface, there are no reconstruction peaks, so the peak widths of the crystal truncation rods with low perpendicular momentum transfer, ie at low l, were measured instead and are shown in figure 6.5. A Lorentzian fitted to these peaks gives a width of $0.11°$ and, ignoring the effect of mosaicity, this gives a surface correlation length of 225Å and 315Å for the $(10\frac{1}{10})$ and $(01\frac{1}{10})$ reflections respectively, which is typical for metal surfaces. A Lorentzian fitted to the $(21\frac{1}{10})$ peak has a width of $0.054°$ which gives a correlation length of 190Å so while there is clearly some effect of mosaicity or instrumental broadening, the major contribution

is from surface correlation length.

6.3.2 Effect of changing the gas pressure

At room temperature, the (2×1) reconstruction is stable only in an ambient CO atmosphere [52, 137]. The intensity of the $(\frac{1}{2}1\frac{1}{10})$ reconstruction peak maximum was monitored as the gas flow was stopped and the CO pumped away, and then the CO pressure returned. Figure 6.6 shows the peak maximum decaying to become indistinguishable from the background over a period of three minutes, when the gas flow was turned off. The figure also shows that when the gas pressure is returned, the reconstruction peak rapidly re-forms, though with reduced intensity.

It was not possible to change the gas pressure remotely, so the X-ray beam was interrupted each time the pressure was altered. The periods in figure 6.6 with zero intensity correspond to the time taken to enter the hutch, alter the pressure, and then lock the hutch again, which took about one minute.

The $(\frac{1}{2}1\frac{1}{10})$ reconstruction peak was measured at six pressure steps from 10^{-5} mbar to 2 bar. Figure 6.7 shows the $(\frac{1}{2}1\frac{1}{10})$ reconstruction peak at each of the pressure steps. The structure factor and peak width of this peak are plotted as the pressure increases in figure 6.8. The figure shows a 30% increase in the structure factor of the peak as the pressure increases to 10 mbar. On increasing the pressure further to 2 bar however, the structure factor drops by 6%. There is also a slight rise in peak width (and hence fall in domain size) as the pressure increases.

The increase in structure factor as the pressure increases to 10 mbar can
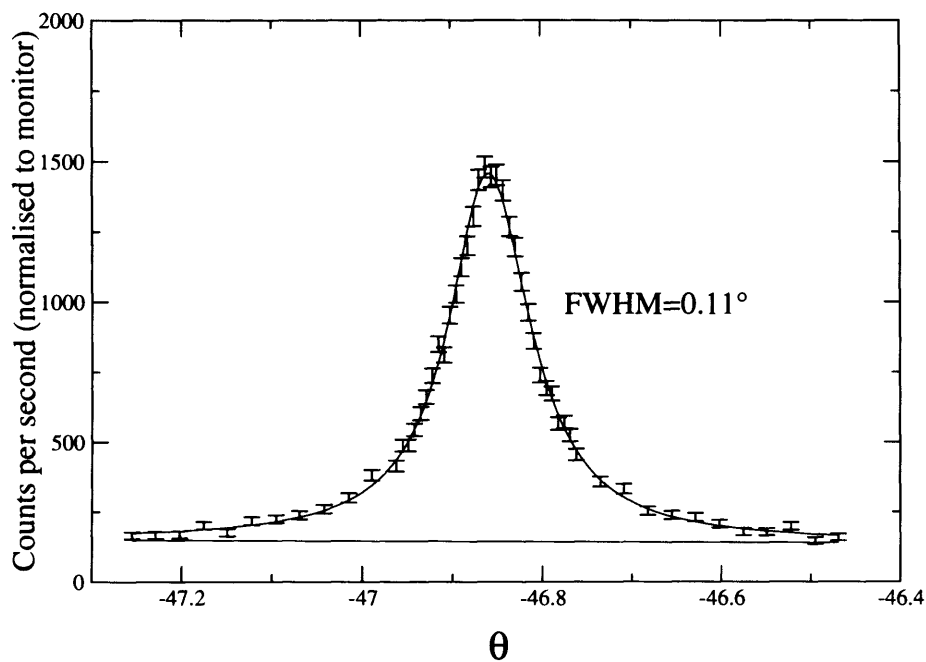
(a) (1 0 0.1)
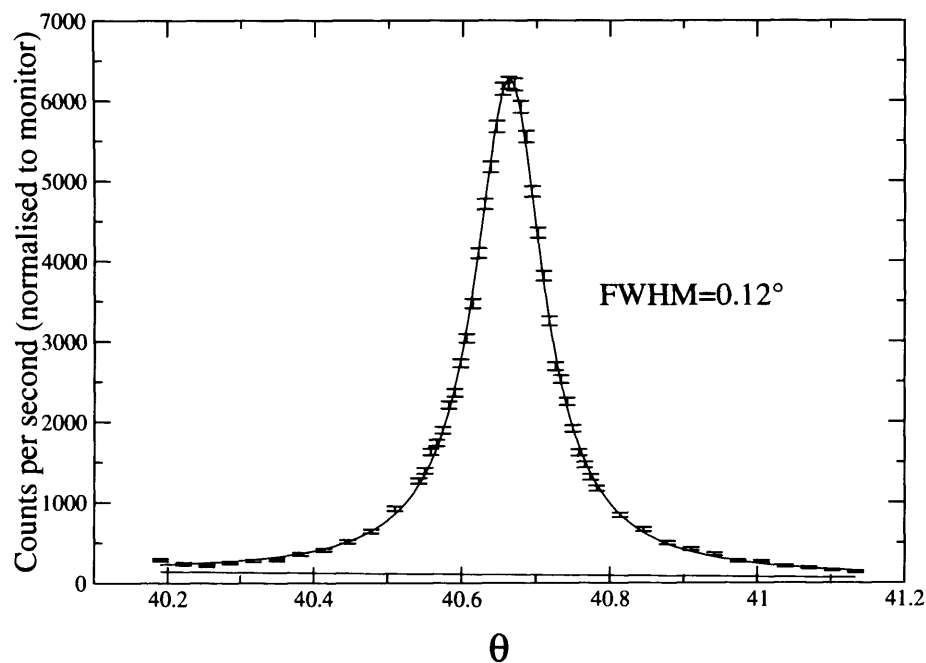
(b) (0 1 0.1)

Figure 6.5: Lorentzian fits with background to θ scans of reference peaks on the clean Ni(110) surface. These give surface correlation lengths of 225Å and 315Å for the $(10\frac{1}{10})$ and $(01\frac{1}{10})$ reflections respectively
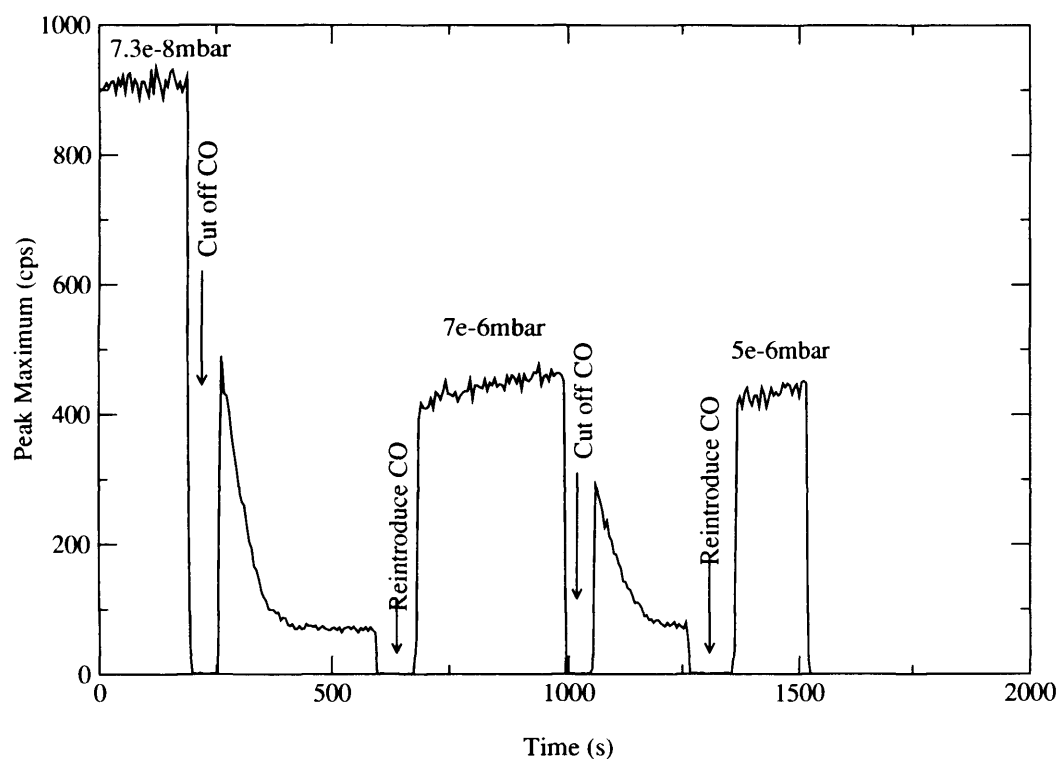
Figure 6.6: Intensity of $(\frac{1}{2}1\frac{1}{10})$ reconstruction peak of (2×1) reconstruction. When CO pressure is removed, the reconstruction decays; when it is returned, the reconstruction is reformed, though the peak is of reduced intensity.
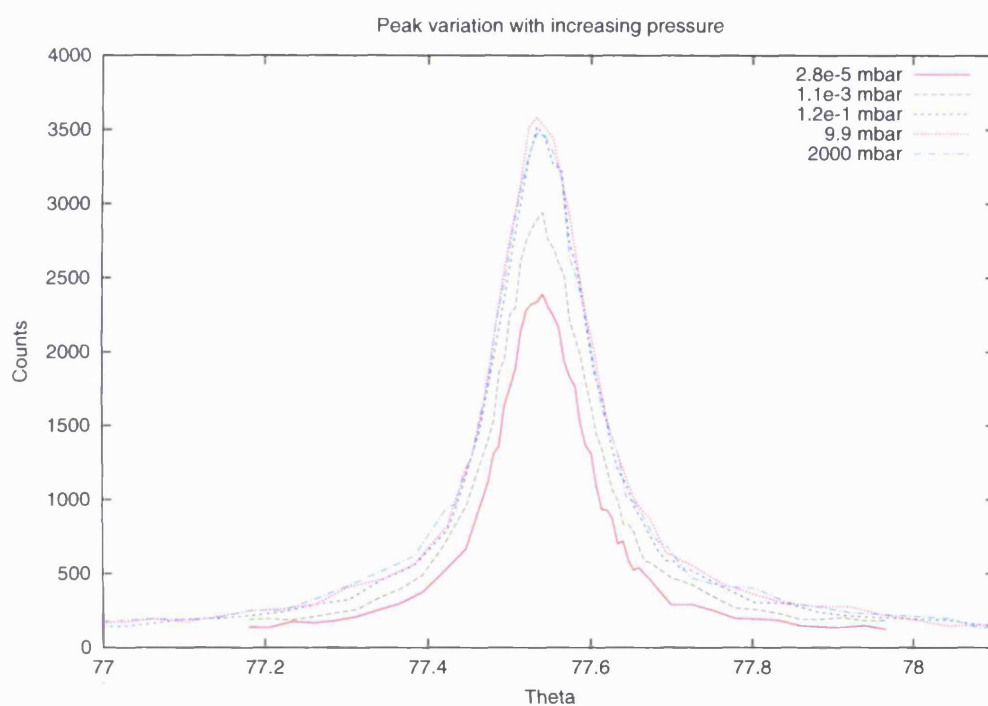
Figure 6.7: θ scans of the $(\frac{1}{2}1\frac{1}{10})$ reconstruction peak at pressure steps from 10^{-5} mbar to 2 bar. The integrated intensity can be seen to be increasing as pressure increases.
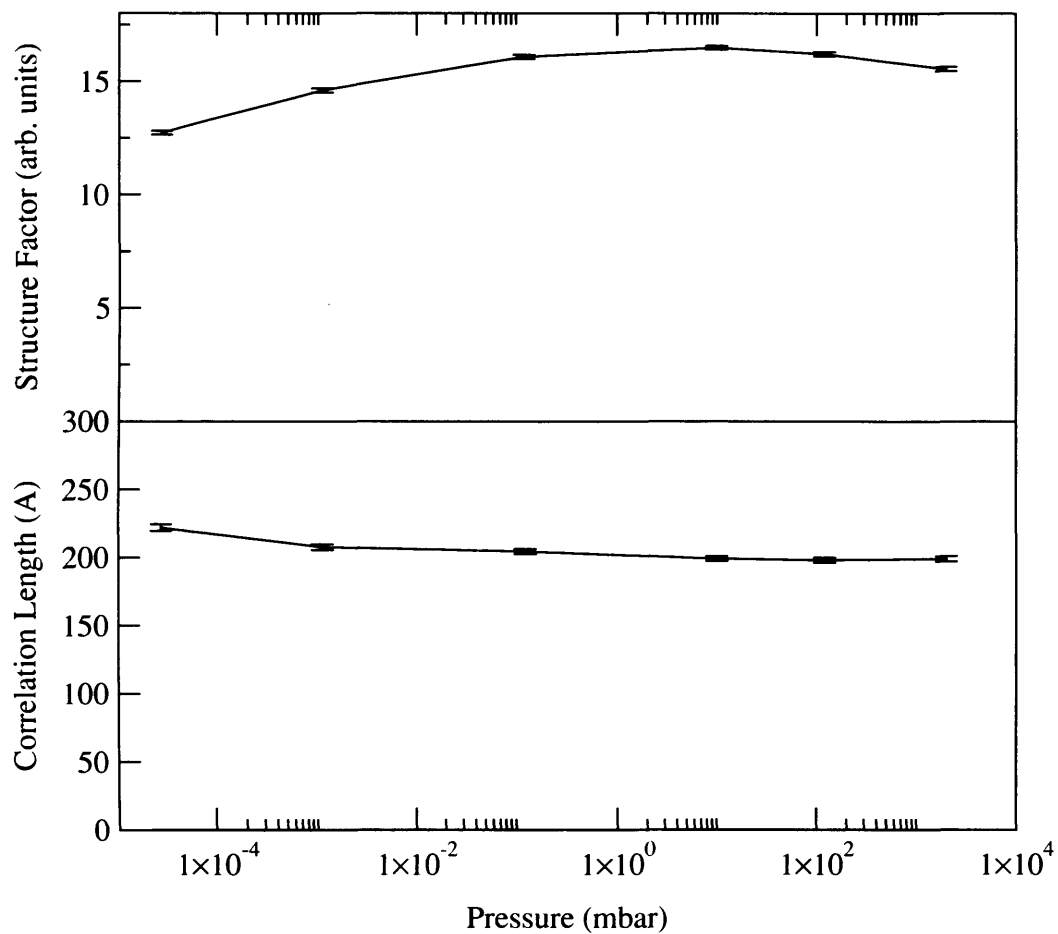
Figure 6.8: Structure factor and peak width of the $\left(\frac{1}{2}1\frac{1}{10}\right)$ reconstruction peak as pressure is increased from 10^{-5} mbar to 2 bar. The structure factor increases by 30% as the pressure increases to 10 mbar, and then starts to fall slightly. There is a small increase in peak width as pressure increases.

be explained in terms of higher occupancy of the surface. The subsequent decrease is more difficult to explain. Several possibilities suggest themselves:

- attenuation by the gas;

- formation of facets;

- disordering of the surface due to impurities;

- a second layer of CO.

Attenuation of the gas can only account for a reduction in structure factor of 1% (the beam is attenuated by around 2% at this pressure). Formation of facets, or an increase in surface impurities, would be accompanied by a decrease in domain size and consequent increase in peak width which is not observed. A second layer of CO may have an effect, though the fractional rods at high pressure (figure 6.11) give no evidence of additional oscillations that would be expected were this the case.

Further experiments looking at symmetry-equivalent peaks, and other reflections will be necessary to determine the cause of the small intensity decrease.

6.3.3 Effect of sample bias on beam damage

Previous experiments [98] show a significant beam effect on the surface at pressures of 20mbar of CO over the Au(111) surface. Those experiments also showed that this effect can be minimised by biasing the sample to +300V with respect to the chamber walls.

To test the effectiveness of this bias, the $(\frac{1}{2}1\frac{1}{10})$ peak maximum of a freshly prepared (2×1) surface was monitored as the surface was exposed to the X-ray beam first with, and then without sample bias. The results of this are plotted in figure 6.9. It clearly shows that, in contrast to the CO/Au system [98], the bias was unnecessary for surface stability over short timescales. This may be due to the Ni(110)-(2×1)-2CO surface being more tightly packed, making it more difficult for CO^+ ions to cause surface damage.
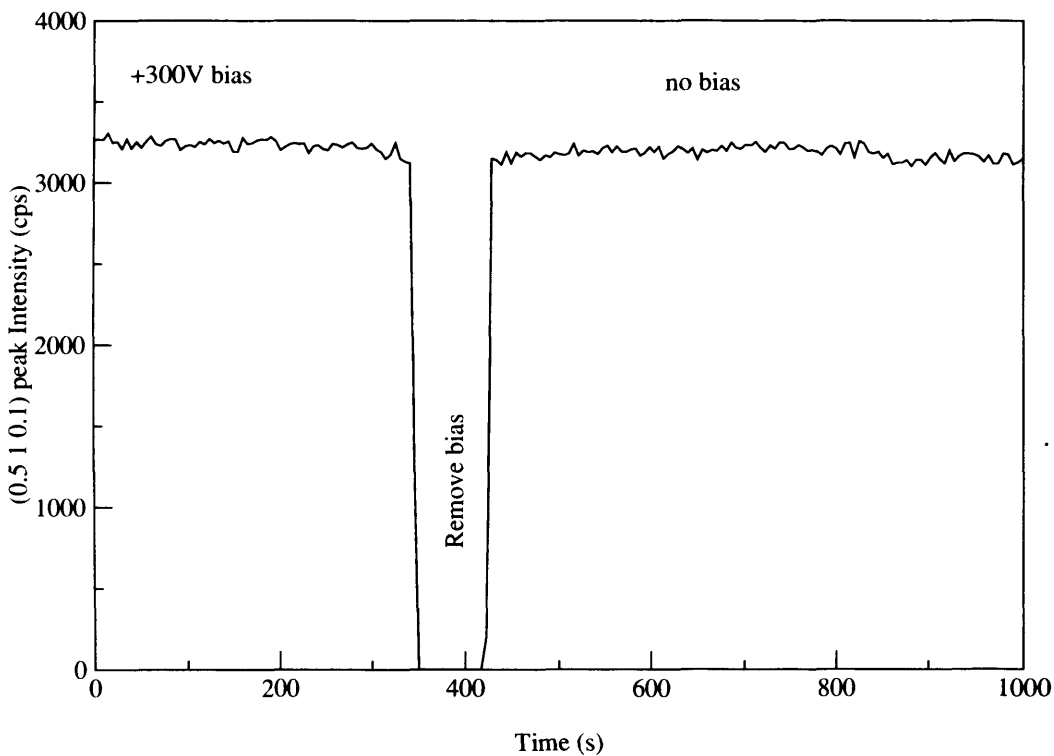
Figure 6.9: Intensity of the $(\frac{1}{2}1\frac{1}{10})$ reconstruction peak monitored over time. The peak shows no decay with or without sample bias.

Although these measurements show little surface degradation over short time periods, a bias of +300V was applied to the sample throughout the high pressure measurements of the (2×1) structure to minimise any possi-

ble degradation over the much longer timescale of the experiment. In the comparison between the UHV and high pressure structures which took over 24 hours, there was little degradation of the $(\frac{1}{2}1\frac{1}{10})$ peak used as a reference and regularly re-measured throughout the experiment. Some beam damage effect must have occurred, however, since when the sample was subsequently cleaned by sputtering at elevated temperature, a darker spot was clearly visible in the center of the sample. This is evidence for the deposition of impurities, possibly carbon, on the sample surface over a longer time period. It is likely that this was a beam effect, as the spot was darker at the centre than the edges. The centre of the sample is illuminated by the beam whatever the position in reciprocal space, whereas the edges need a specific value of θ.

6.3.4 Structural study of (2×1) reconstruction - comparison between UHV and high pressure

The in-plane ($l = 0.1$) fractional order structure factors measured at low and high pressure are tabulated in table 6.2 along with values calculated from the structure that best fitted the high pressure data. These in-plane structure factors are shown graphically in figure 6.10 with the high pressure data in black, the low pressure data in blue, and the model calculations in red. Figure 6.11 shows the structure factors of six diffraction rods, four with h and k integer corresponding to the substrate lattice and two fractional rods arising from the CO (2×1) periodicity. The continuous red curve shows the values calculated from a model fitted to the data by varying the parameters
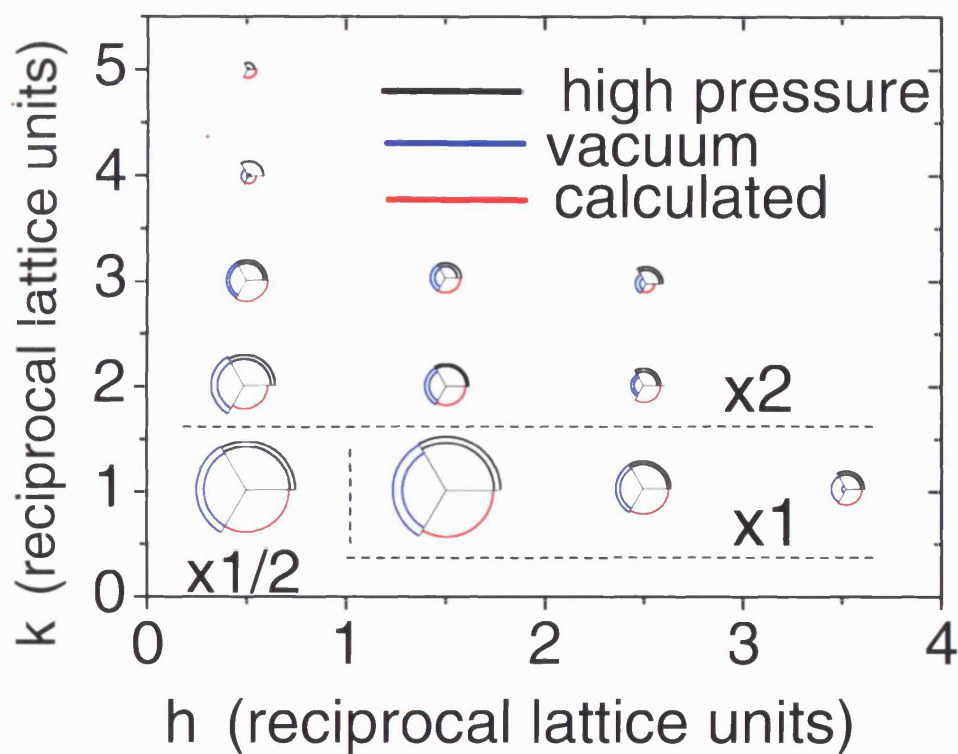
Figure 6.10: In-plane fractional order structure factors measured at $l = 0.1$. The radius of the $120°$ sectors are proportional to the structure factors of the reflections. The two radii represent the error, ie $F \pm \sigma$ is plotted. The black sectors represent the structure factors in 2.3 bar of CO, the blue the vacuum structure and the red ones are calculated from the fit to the high pressure data. It can be seen that the calculated values are a very good fit to the data measured at both high and low pressure
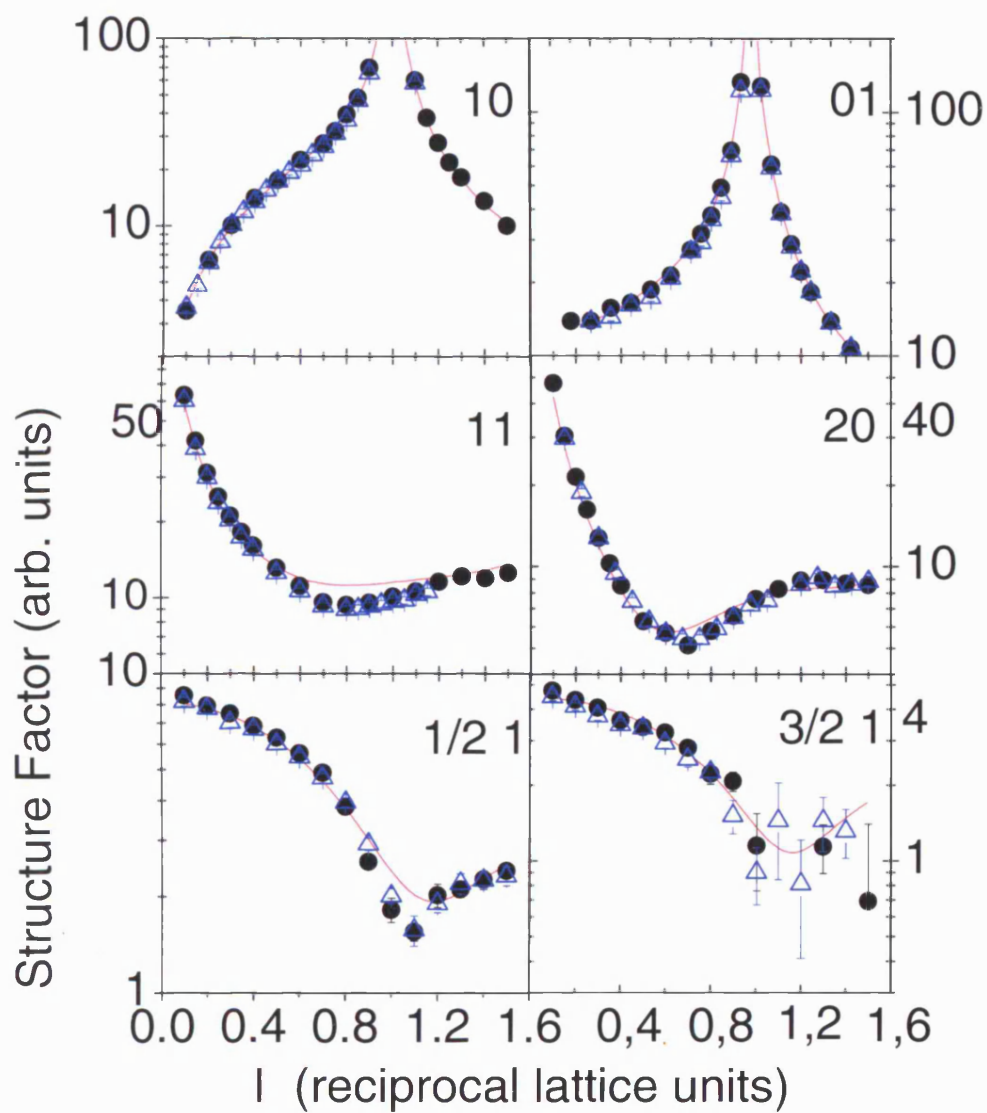
Figure 6.11: Crystal truncation and fractional order rods. Black circles: 2.3 bar, Blue open triangles: 10^{-5}mbar. Red solid lines are calculated from the model giving the best fit to the high pressure data.

			Low Pressure	High Pressure	Model
h	k	l	$F \pm \delta F$	$F \pm \delta F$	F
0.5	1	0.1	8.61 $\pm$ 0.83	8.74 $\pm$ 0.54	8.86
0.5	2	0.1	1.40 $\pm$ 0.14	1.36 $\pm$ 0.09	1.23
0.5	3	0.1	0.87 $\pm$ 0.09	0.88 $\pm$ 0.06	1.12
0.5	4	0.1	0.40 $\pm$ 0.08	0.73 $\pm$ 0.09	0.47
0.5	5	0.1	†	0.10 $\pm$ 0.21	0.46
1.5	0	0.1	0.10 $\pm$ 1.00	†	0.00
1.5	1	0.1	4.55 $\pm$ 0.44	4.83 $\pm$ 0.30	4.88
1.5	2	0.1	0.90 $\pm$ 0.09	1.00 $\pm$ 0.07	1.00
1.5	3	0.1	0.61 $\pm$ 0.09	0.65 $\pm$ 0.08	0.75
2.5	1	0.1	2.40 $\pm$ 0.23	2.48 $\pm$ 0.16	2.70
2.5	2	0.1	0.53 $\pm$ 0.08	0.73 $\pm$ 0.09	0.88
2.5	3	0.1	0.24 $\pm$ 0.13	0.10 $\pm$ 0.58	0.40
3.5	1	0.1	0.92 $\pm$ 0.51	1.54 $\pm$ 0.13	1.72
4.5	1	0.1	0.10 $\pm$ 1.00	†	1.10

Table 6.2: Comparison of in-plane structure factors for the structure measured at low pressure and high pressure, and the model fitted to the high pressure structure. († Data point not measured)

in figure 6.1 using a least squares minimisation procedure.

It is immediately apparent that the vacuum and high pressure data shown in blue and black are identical, demonstrating that the structures are the same. The structure factors calculated from a model fitted to the data are shown in red, and fit very well to the data, giving confidence in the model.

From these results we conclude that the equilibrium structure at room temperature of CO on Ni(110) at 2.3 bars of CO ambient pressure is the same that the structure obtained under UHV conditions by dosing the Ni(110) surface at saturation with 10^{-5} mbar of CO.

(a) High pressure
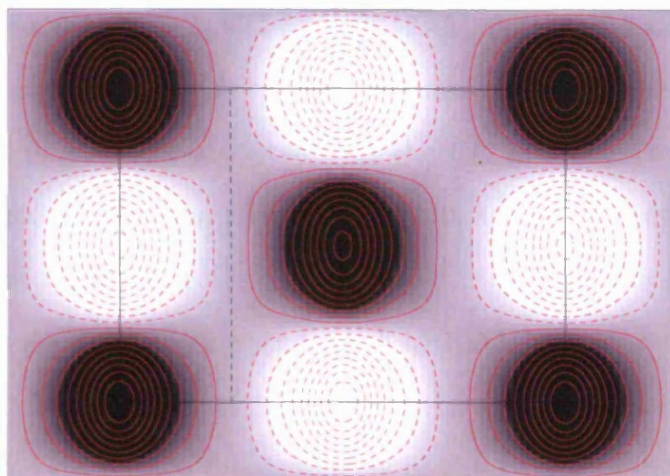
(b) Low pressure
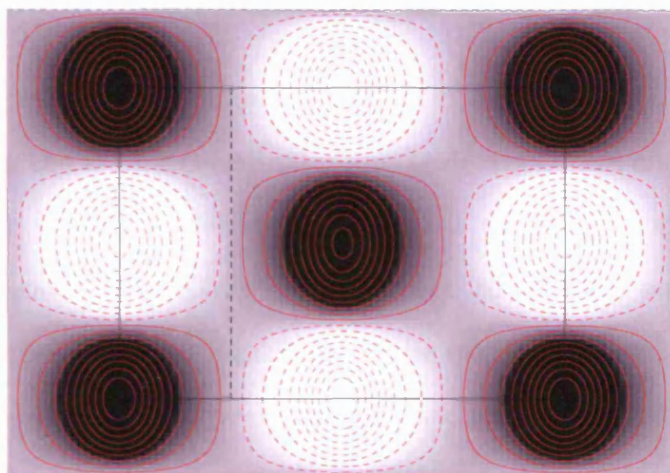
(c) Model
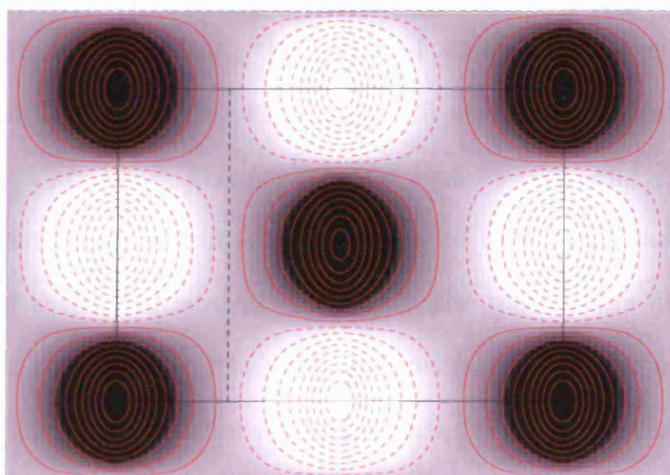
Figure 6.12: Patterson functions for the (2×1) CO/Ni(110) reconstruction. The experimental data at at 2.3 bar and 1×10^{-5} mbar matches the best fit model to the structure. The unit cell is shown by the black square, with the reduced unit cell indicated by the dotted line.

6.3.5 Fitting

As depicted in figures 6.1 and 6.2, CO forms a (2×1) superlattice consisting of an alternate zig-zag arrangement of tilted CO molecules adsorbed on the nickel substrate. It is generally accepted that the CO molecules are in the short bridge sites [103], though an EELS study [130] suggested they may be adsorbed in top sites (figure 2.2).

The most recent crystallographic study with LEED [147] gave a tilt angle of 20 ± 4°, a Ni-C bond length of 1.85 ± 0.04 Å, a C-O bond length of 1.15 ± 0.07 Å and no detectable displacements of the Ni atoms induced by the CO.

The model proposed in this thesis, as shown in figure 6.1, had five parameters to describe the atomic coordinates plus scale, roughness and Debye-Waller factors. The zig-zag model of figure 6.2 was the starting model for the structure refinement. The X-ray data was used to fit the y position of the carbon and oxygen, and the z position of the carbon, oxygen, and top layer of nickel in addition to Debye-Waller factors, and a scale parameter. The x position of the carbon and oxygen are constrained by symmetry.

In order to avoid local minima, three sets of starting parameters with different CO position and tilt angles were used. The starting parameters were those of Robinson *et al.* [103], Hannaman and Passler [50], and Zhao and Passler [147]. To counter any effect from the order of fitting the parameters, each starting model was fitted several times with the parameters fitted in a different order each time. Some fits were also performed by fitting to the inplane data first. The Debye-Waller factor for bulk Ni was fixed throughout

the analysis at 0.34, the value given by Peng *et al.* [97].

The χ^2 value is the weighted sum of squares of the errors, and was used to determine the goodness of fit. A $\chi^2 = 1$ indicates a fit that is a good match to the errors of the data. A $\chi^2 < 1$ is indicative of overfitting the data. In some cases, the fits did converge to false minima, as evidenced by the χ^2 value, but most of the fits resulted in the same atomic parameters. Errors in parameters given are the change in parameter value needed to increase χ^2 by $1/(N - p)$ from its minimum value [34] where N is the number of data points, and p is the number of parameters.

To provide further confirmation that the assignment to short bridge sites was correct, the least squares minimisation procedure described above was used with the CO molecule initially placed in the other possible sites. As can be seen from table 6.3, the short bridge site has the lowest χ^2, and therefore is the most likely.

Position	χ^2
short bridge	2.95
long bridge	91.5706
atop	90.8278
hollow	6.7635

Table 6.3: χ^2 value of best fits at different of adsorption sites. See figure 2.2 for a diagram indicating these sites. The short bridge site is clearly the favoured site, in agreement with recent measurements using other techniques

As shown in table 6.4 the model parameters agree well with the later LEED results from Zhao and Passler [147]. The parameters are also similar to those of Hannaman and Passler [50] and Robinson *et al.* [103].

The difference in Debye-Waller parameter from the fit of Robinson *et*

	LEED		Robinson [103]		This study	
	Hannaman [50]	Zhao [147]	Model I	Model II	High Pressure	Low Pressure
y_C	0.68(7)	0.47(8)	0.67(4)	0.60(6)	0.49(1)	0.50(1)
y_O	1.01(9)	0.86(9)	1.08(2)	1.05(2)	0.98(1)	0.97(1)
z_C	1.33(5)	1.30(4)	1.33(5)	1.30(3)	1.31(2)	1.31(2)
z_O	2.40(7)	2.38(7)	2.39(4)	2.40(3)	2.41(2)	2.41(2)
z_{Ni}	0.02(2)		0.035(4)	0.045(4)	0.058(2)	0.052(3)
B_{bul}			1.32(2)	1.3		
$B_{C(xy)}$			10.8(9)	16(2)	0.6(2)	0.9(2)
$B_{C(z)}$				0		
$B_{O(xy)}$			5.8(3)	5.4(4)	1.2(1)	1.3(1)
$B_{O(z)}$				3.7(10)		
$B_{Ni(xy)}$			2.0(2)	2.4(3)	0.21(5)	0.06(5)
$B_{Ni(z)}$				1.7(1)		
C-Ni bond	1.95(5)	1.85(4)	1.92(5)	1.87(3)	1.83(2)	1.84(2)
C-O bond	1.12(5)	1.15(7)	1.13(5)	1.20(4)	1.21(3)	1.19(3)
C-Ni angle	27(3)	20(4)	27(2)	26(3)	21.3(5)	21.7(5)
CO angle	17(3)	20(4)	21(3)	26(4)	23.9(7)	23.5(9)

Table 6.4: Model Parameters for the best fit models to the experiments described here, compared with previous experiments. The experimental results agree well with the later LEED model of Zhao and Passler [147].

al. [103] can be explained in terms of a larger data set extending further in q available to us. The large Debye-Waller parameters in the model of Robinson *et al.* predict much smaller intensities for the $k = 4$ and $k = 5$ diffraction peaks than were observed in our experiments. These diffraction peaks were not measured by Robinson, and in our model were fitted by an adjustment of the y position of the CO molecule. This may also explain why the anisotropic Debye-Waller parameters found necessary by Robinson did not make a significant difference to the goodness of fit for our data.

6.4 Discussion

The study reported here is the first to measure the *p2mg* (2×1) reconstruction of CO on Ni(110) at high gas pressures. The experiments clearly show the existence of the (2×1) reconstruction at 2.3 bar. There is no significant difference in the structure of the reconstruction between high and low pressures, as the structure factors measured at both pressures agree within the experimental errors. A model fitted to the data using least squares regression results in a structure that is in agreement with, though more accurate than, previous studies [50, 76, 103, 147].

At low coverage, the CO molecules are perpendicular to the surface [137] and have high mobility [115] with an incoherent structure being observed by LEED [52]. At higher CO pressures and therefore greater CO coverage, a (2×1) reconstruction is formed with tilted CO molecules in short bridge sites. The increase in gas pressure has thus caused the molecules to become tilted. It might be expected that increasing the pressure to 2.3 bar would

increase the tilt angle further, however this was not observed. The tilt angle is therefore not dependent on the pressure, but on the adsorption site. This is consistent with the X-ray photoelectron diffraction study by Wesner *et al.* [137], which shows the presence of two distinct adsorption sites with different CO tilt angles.

In the Ni(111)c(4×2)–CO reconstruction [6, 78], CO molecules occupy threefold hollow sites. The position of the CO molecule in the Ni(110)-(2×1)–2CO reconstruction is near this threefold hollow site. The displacement of the CO from this hollow site can be explained by the large size of the molecule causing repulsion from the nickel and other CO molecules, as can be seen in figure 6.1.

6.5 Conclusions of room temperature CO/Ni(110) study

The experiments described here have confirmed the presence of the (2×1) reconstruction of CO on Ni(110) at a CO pressure of 2.3 bar; they have demonstrated that it is possible to use X-ray diffraction to measure surface reconstructions at pressures greater than 1 bar. At room temperature, the structure at 2.3 bar is unchanged from that measured at 10^{-5} mbar. The structure measured is a minor refinement of the established vacuum reconstruction. In particular, the assignment of the CO molecule to the short bridge site [50, 76, 103, 147] is confirmed.

These experiments provide some justification to the low pressure mea-

surements that have been performed to date, as they show that observations at low pressure may extend to high pressure, though it should be noted that chapter 7 provides an example of where they differ.

Chapter 7

Faceting of CO/Ni(110)

7.1 Summary

This chapter will show that heating the Ni(110) surface to 150°C in 2.3 bar of carbon monoxide results in a dramatic change of the surface morphology with the formation of micro-facets with {111} faces. This result is in contrast to that at low pressures, where heating destroys the reconstruction. Analysis of the micro-facets shows they have a size of ≈ 100Å, and that the surface of the micro-facets is disrupted from perfect bulk-like (111) surface. This disruption has been fitted by two different models, a relaxation of the top nickel layer, and also by strain within the micro-facet. Both of these features suggest an enlargement of the lattice near the surface, possibly due to the dissolution of carbon.

The results described in this chapter have been published in Physical Review Letters [100].

7.2   Introduction

The $p2mg(2\times1)$ reconstruction of CO/Ni(110) can be prepared at 100K by simply dosing [103] with carbon monoxide. At higher temperatures, such as room temperature, the reconstruction exists in equilibrium with a background pressure of the carbon monoxide. Experiments by Madden et al. [52] showed that the isostere (the pressure required for constant coverage) at 40-70°C was $10^{-7} - 10^{-5}$ mbar. The aim of the experiments described in this chapter was to measure the effect of heating in the presence of gas. It seemed unlikely that the isostere would apply at these vastly different pressures, and the experiments were designed to test the extent to which it applied, and the changes in surface structure that occurred on heating.

Chemisorbed atoms and molecules can have a profound influence on the structure of metal surfaces. Small displacements of the metal atoms due to the formation of chemical bonds with the adsorbate, known as relaxations, are common [5, 11]. In the Ni(111)c(4×2)-CO reconstruction there is evidence for significant disruption of the surface, and the distortion of the facets from perfect (111) surfaces is possibly due to this persisting after the removal of the CO, or the presence of interstitial carbon due to dissociation of the CO on the surface.

Adsorbates can also give rise to morphological changes, for example restructuring of stepped surfaces. Oxygen deposited on stepped platinum surfaces has been observed to produce double height steps, and faceting has also been observed under these circumstances [109]. Faceting has also been observed by Gaussmann and Kruse [41] who show the interaction of CO with

palladium particles with surfaces containing high index planes between {111} and {100} causes faceting to form the {111} and {100} planes. Ozcomert *et al.* [90] measured oxygen-induced breakup of vicinal Ag(110) surfaces into (110) facets and step bunches using scanning tunnelling microscopy.

Changes to platinum field ion microscopy (FIM) tips have been observed by Voss and Kruse [131]; they noted the growth of {111} planes at the expense of high index planes in the presence of NO but only in the presence of a strong electric field. Experiments by Bar *et al.* [3] show major reshaping of silver FIM tips resulting in growth of the densely packed {111} and {100} planes in preference to high index planes.

More dramatic changes have also been observed to result in the formation of microfacets. STM studies by Somorjai [109, 112] on the Pt(110) surface show the formation of a missing row reconstruction in the presence of hydrogen, the formation of (111) microfacets in the presence of oxygen, and an unreconstructed surface in the presence of carbon monoxide. Sulphur restructures the (111) face of nickel until the metal surface assumes the (100) orientation [114].

7.3 Experimental

Two periods of beamtime on the Surface Diffraction beamline of the ESRF (beamline ID3) [35] were used. The synchrotron was operating in 16 bunch mode [31], and a photon energy of 17.0 keV (0.729 Å) was used. The Ni(110) crystal was mounted in the UHV/High Pressure chamber described in chapter 4 and elsewhere [35].

The 99.997% pure carbon monoxide was supplied by Air Liquide. It was further cleaned by a distillation procedure detailed in section 4.3.1. A high purity (99.995%) nickel (110) crystal (supplied by Surface Preparation Laboratory, The Netherlands) was used for the experiments. The surface miscut was less than 0.1°. After a final 0.05 micron polishing step, the rms surface roughness was less than 0.03 micron [67].

For both periods of beamtime, the sample surface was initially cleaned by cycles of sputter-annealing lasting at least twelve hours, with final sputter-annealing in the UHV/HiP chamber. The (2×1) reconstruction was then prepared by sputtering followed by annealing at 800°C for two minutes and cooling in an atmosphere of 10^{-5} mbar carbon monoxide.

The effect of heating on the (2×1) reconstruction was measured by monitoring the $(\frac{1}{2}1\frac{1}{10})$ reflection which is due to the reconstruction and also the $(01\frac{1}{10})$ due to the CTR as the sample was heated. This was performed at carbon monoxide pressures of 1×10^{-5} mbar and 2.3 bar. Initially, attempts were made to monitor the reconstruction by measuring the peak intensity of the $(\frac{1}{2}1\frac{1}{10})$ peak as the sample was heated; thermal expansion however caused the height of the sample to change and move out of alignment with the X-ray beam. To avoid this alignment problem the integrated intensity was measured using a rocking scan, and the height of the sample was realigned every two integrated intensity scans.

Information on the nickel surface was obtained from CTRs from the bulk crystal measured before and after heating in CO. Truncation rods from the micro-facets were also measured after heating. Reciprocal space scans along the k direction were measured (these show the presence of micro-facets).

After this second experiment an AFM study of the surface was performed.

Diffracted intensities were measured by setting the crystal and detector to fulfill the diffraction condition, and then rotating the crystal around the diffractometer θ axis (corresponding to a rotation about the sample surface normal).

As well as the conventional CTRs, truncation rods from the microfacet surfaces were also measured. Integrated intensities along these facet rods were measured by rotating the crystal around the diffractometer θ axis which corresponds to a rotation around the (110) surface normal.

Integrated intensities were obtained by subtracting the background and analytically integrating the area under a Lorentzian fitted to the peak. The peaks have a clear Lorentzian shape, as shown in the previous chapter, and this procedure was necessary to fit the long tails of the Lorentzian and obtain a good estimate of the background. This peak shape is characteristic of a surface correlation given by an exponential pair distribution function [129]. Structure factors were obtained by taking the square root of these integrated intensities and applying the resolution and geometrical corrections described by Vlieg [125]. This was performed using the computer program ANA described in section 5.1.2.
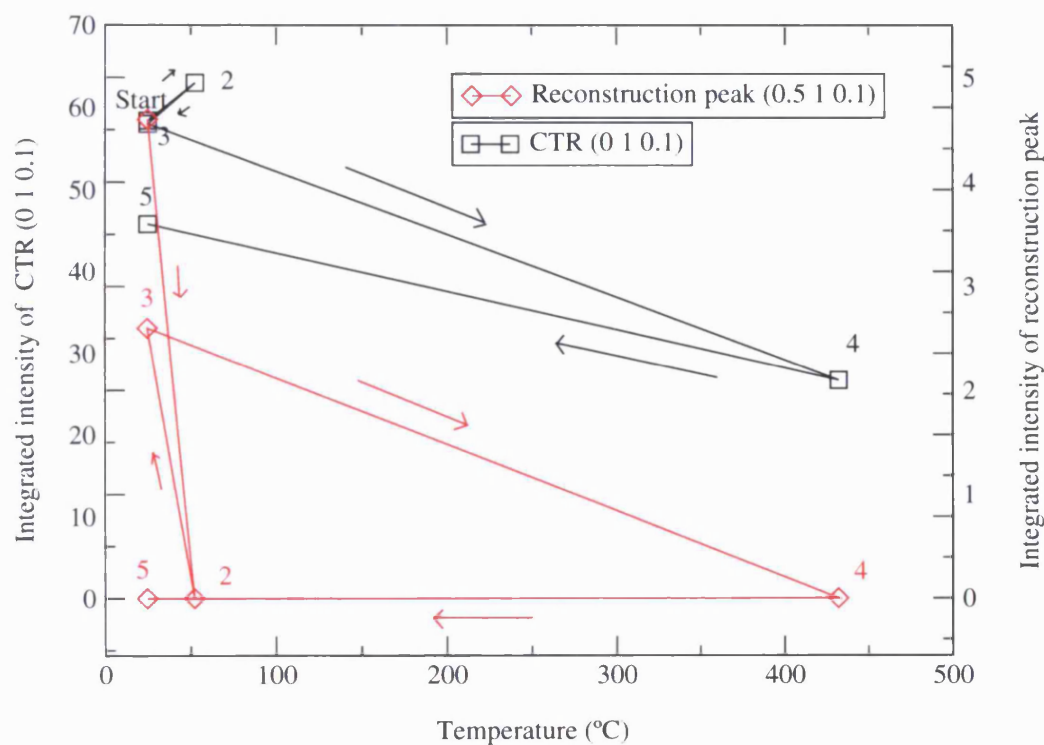
Figure 7.1: Variation of the integrated intensity due to the Ni(110)-(2×1)-2CO reconstruction as the sample is heated in a carbon monoxide pressure of 1×10^{-5} mbar. The $(\frac{1}{2}1\frac{1}{10})$ reflection due to the reconstruction is shown in red and the $(01\frac{1}{10})$ due to the CTR in black. Heating above 50°C destroys the reconstruction peak, however on cooling the reconstruction returns though with lower intensity. The CTR which is due to the termination of the bulk was however unchanged. Heating to 430°C caused the reconstruction to disappear permanently and a small decrease in the CTR suggesting some disruption of the nickel surface.

7.4   Effect of heating on the reconstruction and CTRs

The effect of heating the CO/Ni(110) reconstruction at a carbon monoxide pressure of 1×10^{-5} mbar was measured by monitoring the $(\frac{1}{2}1\frac{1}{10})$ peak due to the (2×1) reconstruction and the $(01\frac{1}{10})$ peak from the crystal truncation rod, and the results are shown in figure 7.1. Heating to 50°C (point 2) destroys the reconstruction peak and there is a small increase in the intensity of the CTR peak. On cooling (point 3), the reconstruction peak is reformed with a 30% loss in intensity, and the CTR peak shows no change from its original intensity. Heating causes the CO to desorb from the surface and the (2×1) reconstruction covers less of the surface and hence the diffraction peak is weaker. The reduction in intensity after cooling is due to a lower coverage of the (2×1) reconstruction.

Heating to 430°C in 1×10^{-5} mbar CO (point 4) results in permanent loss of the reconstruction peak and a reduction by 50% of the intensity of the CTR peak though it recovers to some extent on cooling (point 5). Thus there is little change to the CTR peak on heating to 50°C, but heating to 430°C in 1×10^{-5} mbar CO does result in a small degradation in the surface, possibly due to roughness or impurities on the surface, and this prevents an ordered (2×1) reconstruction from reforming.

At the much higher pressure of 2.3 bar the effect of heating is shown in figure 7.2 and the results are significantly different. In contrast to the result at 1×10^{-5} mbar, heating to 50°C has little effect on the reconstruction peak. Above 100°C, both the reconstruction and CTR peaks decrease irreversibly

Facet Reaction -- 2.3 bar CO/Ni(110)
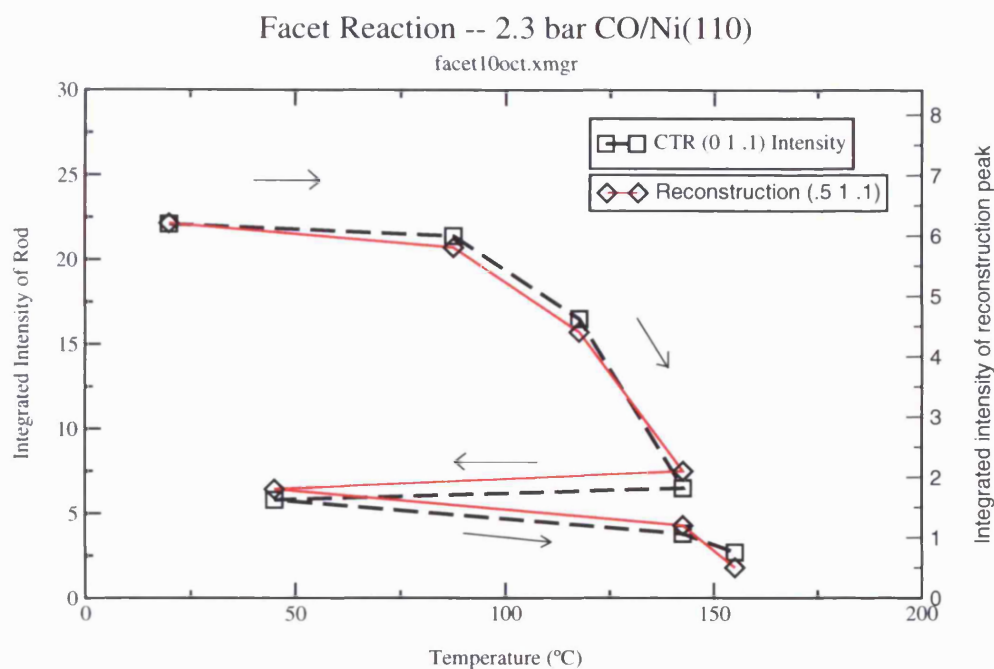
Figure 7.2: Integrated intensity of reconstruction $(\frac{1}{2}1\frac{1}{10})$ and CTR $(01\frac{1}{10})$ peaks as sample is heated. Little change occurs to a temperature of 100°C, then the intensity dramatically reduces. Cooling the sample does not increase the intensity of either the reconstruction or CTR, so the change is irreversible.

almost to zero. The loss of the CTR peak is due to a radical reorganisation of the (110) surface to form {111} facets. As the destruction of the (2×1) and CTR peaks occur at the same rate, the decay of the (2×1) peak is due to destruction of the (110) surface, rather than desorption which was the case at 1×10^{-5} mbar.
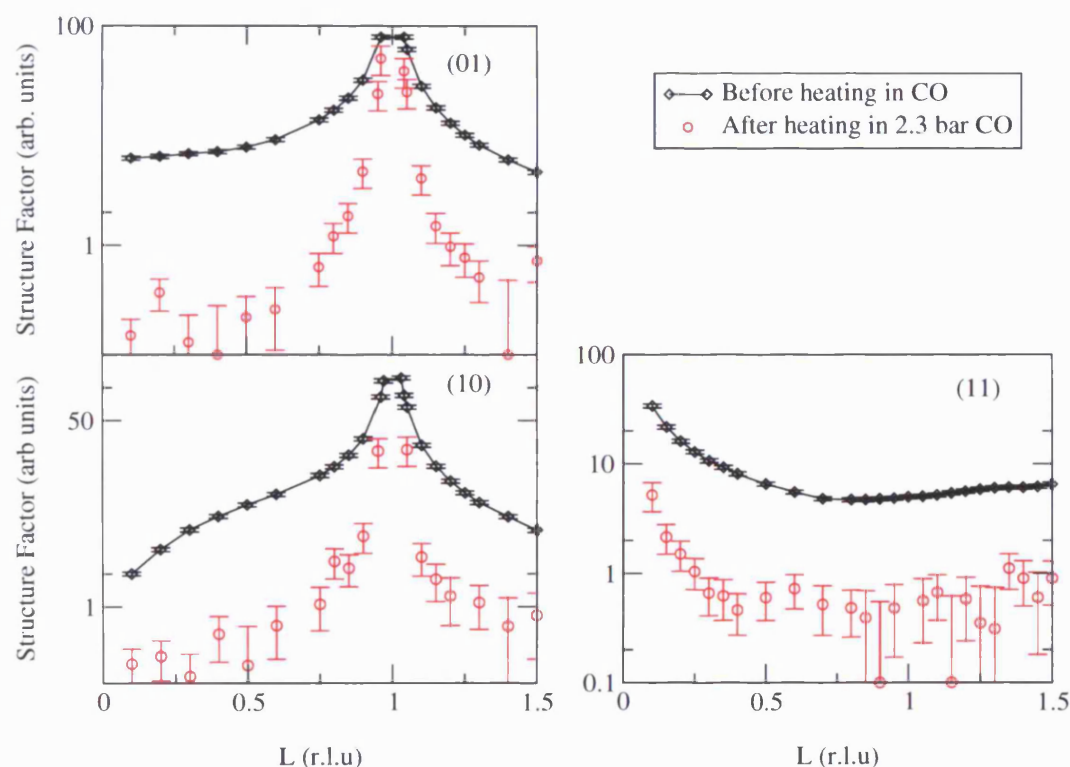
Figure 7.3: Crystal truncation rods of Ni(110) crystal before and after heating in CO at 2.3 bar. After heating, the intensity falls away from the Bragg peaks more rapidly, which is an indication of increased surface roughness.

7.5 Analysis of surface after heating in 2.3 bar CO

7.5.1 Crystal truncation rods (CTRs)

The previous section has shown that heating to 150°C in 2.3 bar of CO results not only in destruction of the $(\frac{1}{2}1\frac{1}{10})$ peak due to the reconstruction, but also to the $(01\frac{1}{10})$ peak due to the CTR. The change in the CTR peak, which is irreversible on cooling, suggests a radical roughening of the nickel surface has occurred.

To study the changes in the surface, crystal truncation rods were measured before and after heating in 2.3 bar of CO. Figure 7.3 shows these truncation rods and demonstrates a dramatic decrease in intensity of the CTR though there is no noticeable change in shape. This is evidence for considerable disruption of the surface. Later in this chapter it is shown that this disruption takes the form of a change in the surface morphology to produce (111) microfacets.

7.5.2 Reciprocal space scans

After heating in 2.3 bar CO at 150°C for ten minutes, the sample was cooled, reciprocal space scans along the k axis with $h = 0$ were then performed and are shown in figure 7.4. The figure shows that the crystal truncation rod is present, though the peaks are weak at $k = 1$. The important feature however is the presence of additional peaks along lines at $k = l$, and $2 - k = l$. These additional peaks are truncation rods arising from the surface of microfacets
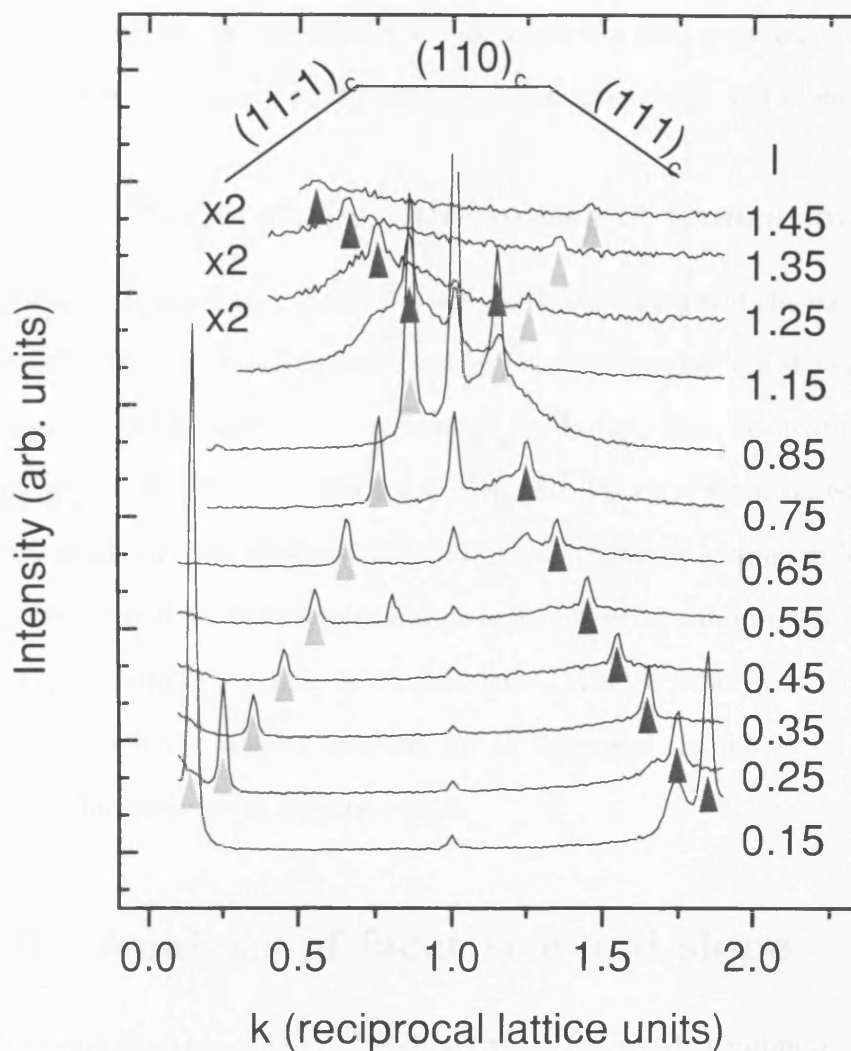
Figure 7.4: Scans along the k direction in reciprocal space for different values of perpendicular momentum transfer l (h was held at $h = 0$), obtained after annealing the Ni(110) crystal for ten minutes at 150° C in 2.3 bar of CO. The peaks marked with light and dark grey arise from the (111) and (11$\bar{1}$) facets respectively. The bulk crystal truncation rod at k=1 is present, though weaker than the rods due to the facets except close to the Bragg peak ($k = l = 1$).

rather than the (110) surface of the bulk crystal. The position of these peaks in reciprocal space is shown schematically in figure 7.5. Figure 7.6 is a model of the surface that would give this scattering. The peaks due to the truncation of surface by facets correspond to the close packed $(111)_{cubic}$ and $(11\bar{1})_{cubic}$ planes in the standard face centred cubic notation for the nickel crystal. No additional peaks were observed when scanning along the h axis.

7.5.3   Crystal shape - the source of truncation rods

Crystal truncation rods occur because of the truncation of the bulk crystal, as described in section 3.3.2; they are the Fourier transform of the crystal shape function. If the surface is terminated by facets, then truncation rods will appear perpendicular to the facet surfaces. This has been noted previously in the study of "hut clusters" [87, 117], small regularly shaped dislocation-free islands formed by heteroepitaxial growth, of germanium on silicon (001) for example. Similarly a miscut surface has CTRs perpendicular to the surface [51, 84] with the miscut showing up as increased roughness on the surface due to fluctuations in terrace width.

7.6   Analysis of facet size and slope

Close examination of figure 7.4 shows there is a small asymmetry in the sizes of the peaks at the same l. The peak at $k = 0.85$ is larger than that and $k = 1.15$ for example. This is especially pronounced near the Bragg peak at $k = l = 1$; the peaks at $k < 1$ are more intense than the peaks at $k > 1$. This is an indication that the surface is disrupted from bulk-like (111) facets. If the
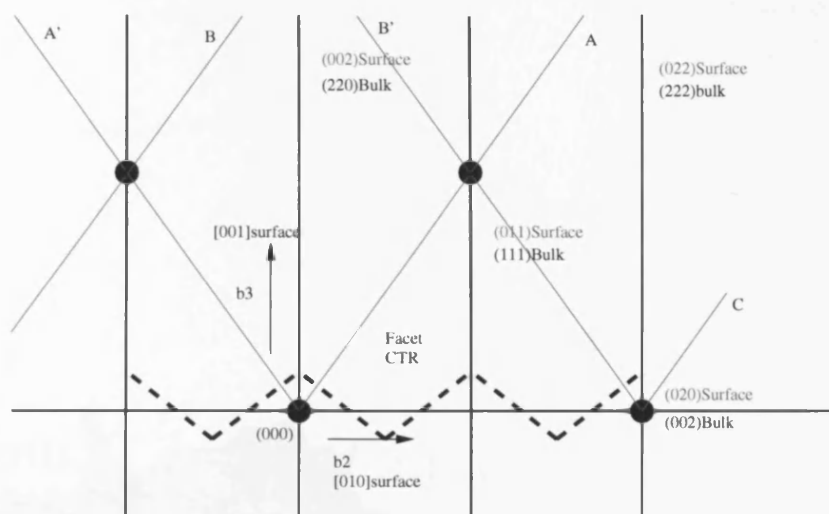
(a) (0 k l) plane
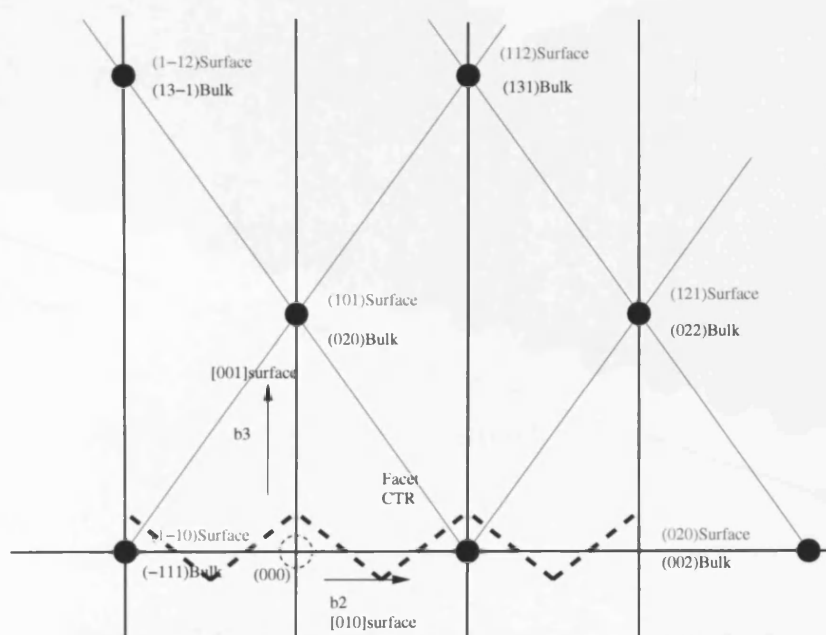
(b) (1 k l) Reciprocal space in plane showing CTRs and facet rods

Figure 7.5: Reciprocal space plot of CTRs (black) and CTRs arising from {111} facets (red) on a Ni(110) surface after heating in 2.3 bar CO.
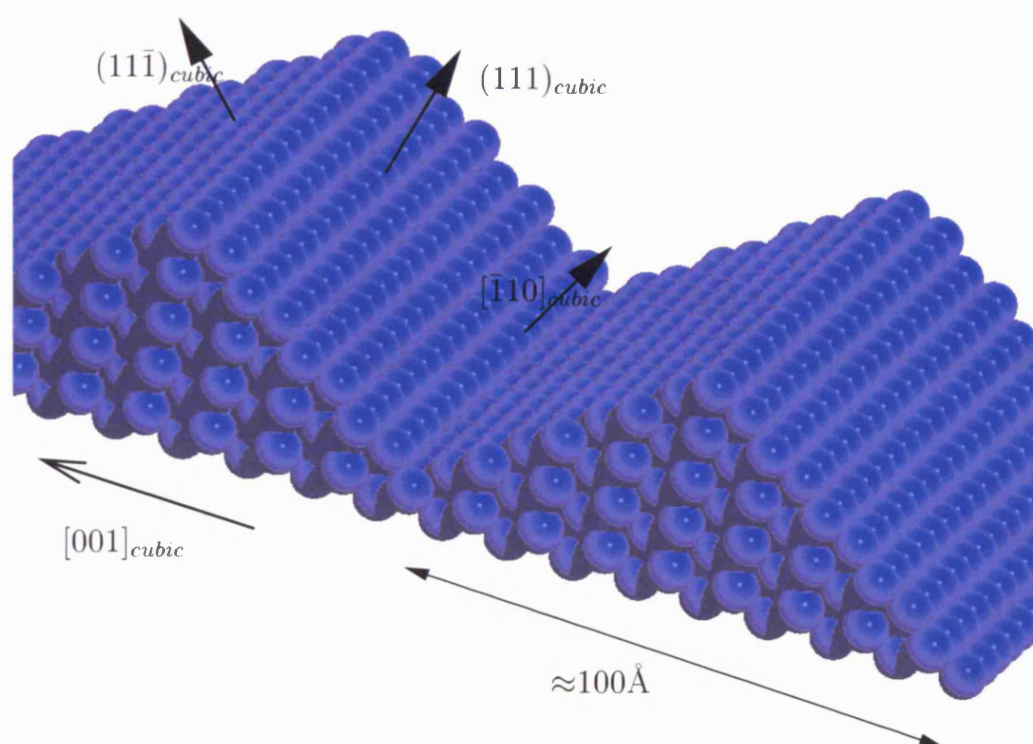
Figure 7.6: Model of (111) facets on (110) surface

Real space: Reciprocal space:

$$\mathbf{a_1} = \tfrac{1}{2} \quad [\bar{1}10]_{cubic}$$

$$\mathbf{a_2} = \tfrac{1}{2}[0\bar{1}1]_{cubic}$$

$$\mathbf{a_3} = [111]_{cubic}$$

$$\mathbf{b_1} = \tfrac{1}{3}(\bar{4}22)_{cubic}$$

$$\mathbf{b_2} = \tfrac{1}{3}(\bar{2}\bar{2}4)_{cubic}$$

$$\mathbf{b_3} = \tfrac{1}{3}(111)_{cubic}$$

$$|\mathbf{a_1}| = |\mathbf{a_2}| = \frac{a_0}{\sqrt{2}} = 2.492\text{Å}$$

$$|\mathbf{a_3}| = \sqrt{3}a_0 = 6.104\text{Å}$$

$$a_0 = 3.524\text{Å}$$

$$|\mathbf{b_1}| = |\mathbf{b_2}| = \frac{2\pi}{a_0}\sqrt{\frac{8}{3}} = 2.91\text{Å}^{-1}$$

$$|\mathbf{b_3}| = \frac{2\pi}{a_0\sqrt{3}} = 1.03\text{Å}^{-1}$$

Table 7.1: Coordinate transforms between face centred cubic and (111) surface notation

(111) facets had been bulk-like, then the peaks at $k < 1$ and $k > 1$ would be of the same size. There is therefore some modification of the facet from this perfect model. The disruption from perfect (111) faces has been modelled in two ways in sections 7.6.1 and 7.6.2. In section 7.6.1 the facet truncation rods are modelled by considering a model with a perfect {111} surface and allowing the top layer of nickel atoms to relax outwards. In section 7.6.2 an alternative model based on an expansion of the lattice parameter (which could be due to dissolved carbon) in the facets is used, resulting in a strained system.

These are simple models and make a number of assumptions, but they give some indication of the effects that are taking place. It should be noted that one possible cause of asymmetry would be a miscut surface, so that the (111) surface area was bigger than the (11$\bar{1}$) surface. This is not the case here however as this would cause asymmetry of the peaks at $h = 1$, which

was not observed.

Further work on the CO/Ni(111) system is planned and may give more information on the changes to the surface and this may allow distinguishing between the two models.

7.6.1   Fitting the truncation rods from facet surfaces

As has been discussed in section 7.5.3, the formation of {111} facets results in crystal truncation rods perpendicular to the facets. Integrated intensities were measured along the lines marked A, B, C from the (111) face, and A',B' from the (11$\bar{1}$) face in figure 7.5. These integrated intensities were fitted in terms of a (111) surface by transforming the coordinates as described below.
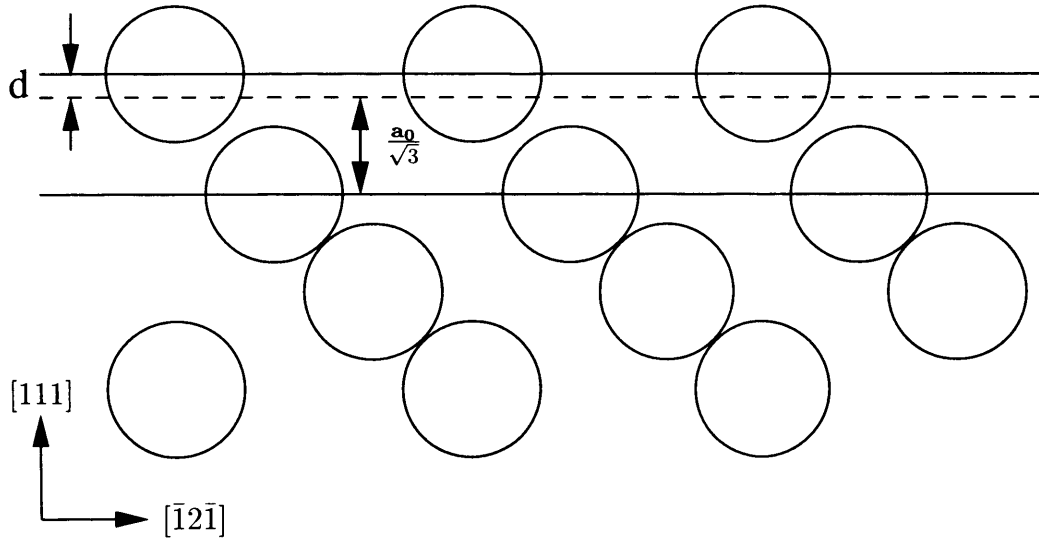
Figure 7.7: Simple model of relaxation of top layer of atoms in facet. Top layer of nickel atoms is relaxed by varying their displacement perpendicular to the surface by the distance d from the position in the ideal bulk. In the bulk the interlayer spacing is $\frac{a_0}{\sqrt{3}}$.
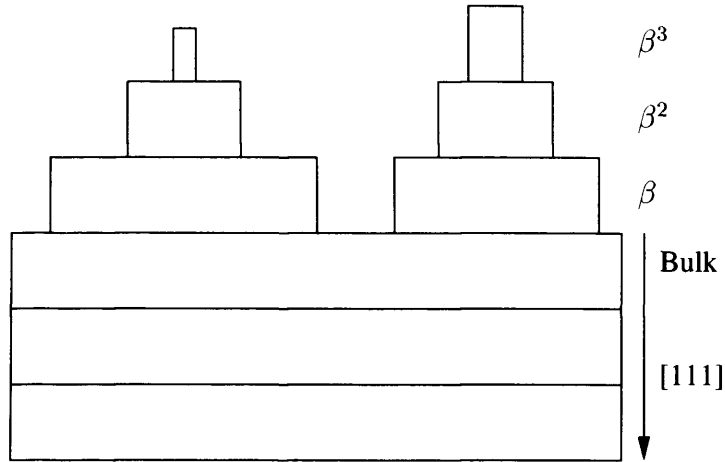
Figure 7.8: Surface roughness on a facet according to the so-called β model

Coordinate transforms

Throughout most of this chapter, the (110) surface coordinate system given in section 6.1.2 and used in the previous chapter has been used. In this, l is perpendicular to the $(110)_{cubic}$ surface.

Just as the analysis of the surface can be simplified by following the LEED convention and using l as the momentum transfer vector perpendicular to the surface, the analysis of the facets has been simplified by using a coordinate system where l is the momentum transfer perpendicular to the (111) surface of the facet. The relationship between this system and the standard cubic notation is given in table 7.1. Figure 7.5 shows schematically the truncation rods from the surface and the facets.

$$F_{sum} = F_{surf} + F_{bulk} \tag{7.1}$$

with

$$F_{surf} = \overset{\text{surface unit cell}}{\underset{j}{\sum}} f_j \theta_j e^{2\pi i(hx+ky+lz)} \tag{7.2}$$

$$F_{bulk} = \sum_{-\infty}^{0} F_u e^{2\pi ilj} e^{j\alpha} \tag{7.3}$$

$$\tag{7.4}$$

and

$$F_u = \overset{\text{bulk unit cell}}{\underset{j}{\sum}} f_j e^{2\pi i(hx_j+ky_j+lz_j)} \tag{7.5}$$

The β-roughness model was used to fit the roughness. In this model, surface layer n has an occupancy of β^n as shown in figure 7.8.

Fitting the relaxation d of the top layer of nickel atoms (figure 7.7) and the roughness parameter β (figure 7.8) to the truncation rods from the micro-facets (figure 7.9) result in a surface relaxation d of 0.11Å from the bulk position, which is reasonable, and consistent with other studies of the Ni(111)˙ surface. A β roughness parameter of 0.08 is also found which implies significant surface roughness, as would be expected for small facets.

7.6.2 Modelling the facets based on surface strain

To a first approximation, the width of the peaks in figure 7.4 is determined by the facet size, and the asymmetry in their intensity is due to the strain. This asymmetry was fitted following the procedure of Steinfort et al. [117] as applied to "hut clusters". The clusters were modelled as long and narrow triangular prisms with (111) and (11$\bar{1}$) faces as shown in figure 7.6. The interatomic distance along the a_2 axis was allowed to vary quadratically
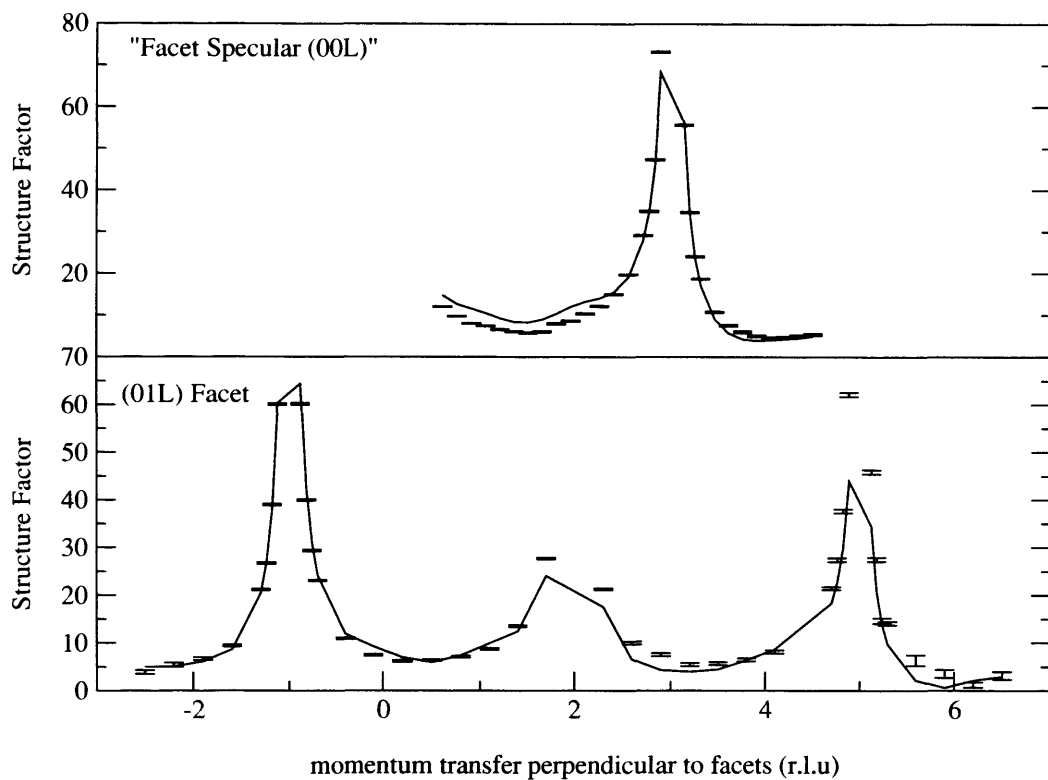
Figure 7.9: Fit to truncation rods from the (111) facet. Top: the "facet specular", ie $k = l_{(110)}$. Bottom: $(01l)_{(111)}$ equivalent to $2+k = l$ and $2 - k = l$
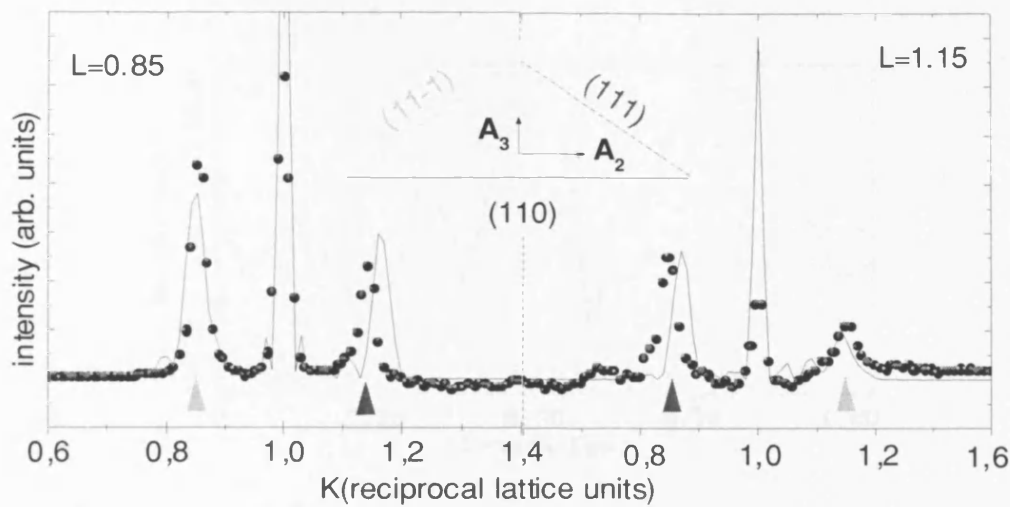
Figure 7.10: Comparison of model calculations to experimental data. The model prediction (solid line) corresponds to a model of strained facets with a base of 100Å and strain of 4%.

with height from zero strain at the base to maximum strain at the apex. The deformations along the a_3 axis were calculated from the Poisson ratio. The continuous line in figure 7.10 which approximately fits the data had a strain value of 4% at the apex. This value of the strain is consistent with a solid solution of about 1% carbon atoms in the Ni crystal.

7.6.3   AFM

After the final experiment, atomic force microscopy (AFM) was perfomed *ex-situ* on a $1\mu m^2$ area of the sample by Peters [99] using a Digital Instruments Nanoscope and the tapping mode. The results of this study are given in figure 7.11. In figure 7.11(a), a cross-section of the local surface height shows large local height variations in the form of steeply sloped valleys up to 20nm
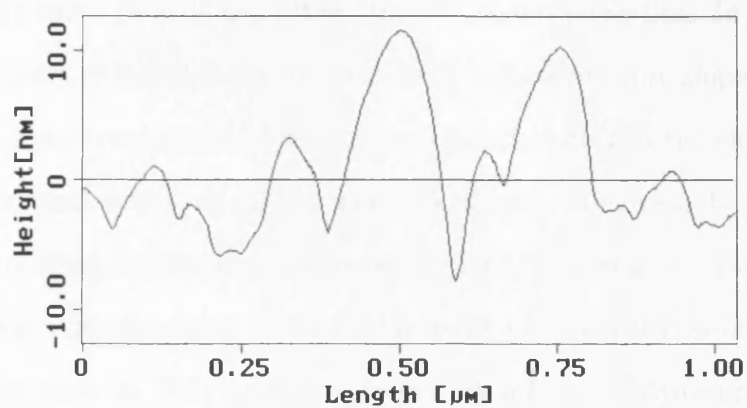
(a) Cross-section of surface height along solid line in (b)
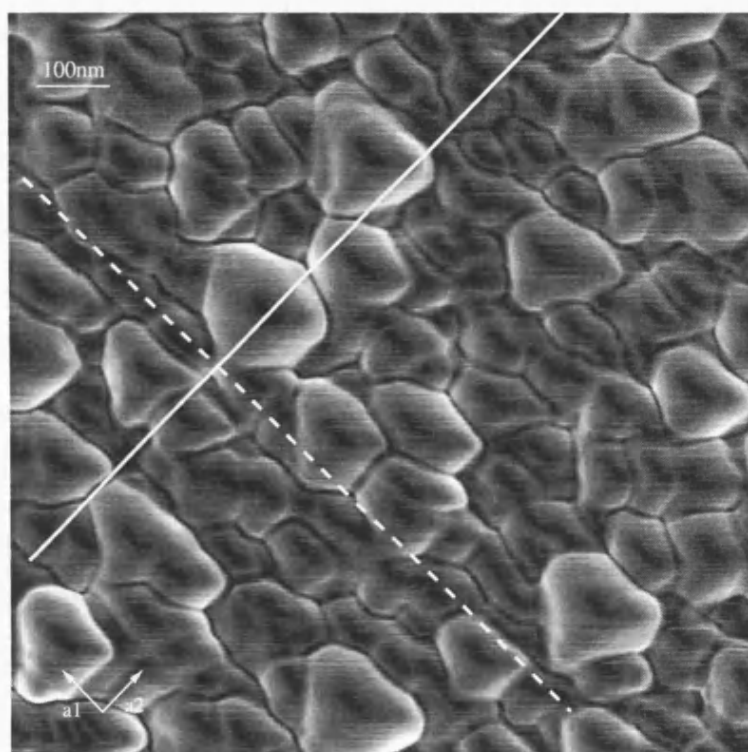
(b) Surface image of local slope obtained from height data. Black areas have zero slope and white $\approx 25°$. Dashed line indicates a preferred direction of valleys, hill tops and white steeply sloped areas. The height profile along the solid white line is shown in (a).

Figure 7.11: AFM results of surface morphology of $1 \times 1 \mu m^2$ area of partially reacted CO/Ni(110)

deep, which outline hills of 50-200nm diameter. Figure 7.11(b) reveals the morphology more clearly and allows further characterisation. In this image, the height data is transformed so that black represents zero slope, and white represents maximum slope. The bottom of each valley is therefore black as it has approximately zero slope. The top of each hill has only a small flat area of zero slope, indicating how little the Ni(110) terraces persist after the CO reaction. Most surface area has instead transformed to other surface orientations such as Ni(111) micro-facets, as follows: White areas deep in the valleys have the steepest slope. The measured slope, up to 25°, compares with the expected (111)-(110) interplanar angle of 35°, and the difference can be understood in terms of the size of the AFM tip. Also apparent is the preferred orientation (parallel to dashed line) of many valleys, steeply sloping areas (shown in white), and hill tops. This is the a_1 direction along the imperfect micro-facets. The AFM image (figure 7.11) illustrates that the surface is otherwise rather disordered and more complex than might seem apparent from the X-ray data. The AFM image appears to show larger facets than the X-ray data, these could be due to intermediate faces that are much smaller than the {111} domains. These intermediate faces will scatter throughout reciprocal space and add to the background. Figures 7.4 and 7.7 thus show an intermediate state of micro-facet formation and ordering, following an elevated-temperature elevated-pressure reaction of 2.3 bars CO over the Ni(110) surface.

7.7 Discussion

7.7.1 Effect of gas pressure when heating

The gas pressure needed for a stable (2×1) reconstruction depends upon the temperature. The experiments in this chapter have shown that heating the (2×1) reconstruction in a pressure of 1×10^{-5} mbar of CO (figure 7.1) results in a lifting of the reconstruction. This is consistent with the isostere of Madden et al. [52] which predicts that for pressures from 10^{-7} mbar to 10^{-5} mbar, the (2×1) reconstruction is stable at temperatures of 40-70°C.

At higher pressures the results are significantly different however. Extrapolating the isostere measured by Madden et al. to a pressure of 2.3 bar, an extrapolation of eight orders of magnitude, desorption is predicted at a temperature of 400°C. This extrapolation was not found to be correct however. Experimentally, at this pressure a dramatic change in the surface morphology was observed at around 150°C (figure 7.2). The diffraction peak due to the reconstruction decreased at the same rate as that due to the CTR. The (2×1) reconstruction was therefore not destroyed by desorption of the CO at 400°C as predicted by the isostere, and as happens at lower pressures, but by the destruction of the underlying (110) surface. This isostere therefore doesn't correctly predict the decay of the (2×1) reconstruction due to some other physical effect (the destruction of the underlying surface) occurring first.

7.7.2   Gas induced faceting

After heating to 150°C in a pressure of 2.3 bar of carbon monoxide, the intensity of the crystal truncation rods due to the (110) surface is decreased (figure 7.2). This is due to there no longer being a sharp (110) interface. Additional peaks are present in reciprocal space scans in k (figure 7.4), though none are observed in reciprocal space scans along h. These additional peaks are due to the formation of {111} micro-facets.

This change in the surface is not unexpected — adsorbate induced changes in surface morphology have been observed previously on a number of systems, as discussed in section 7.2. In the experiments reported in this chapter however the changes are not from high index planes, but from the (110) plane. The Ni(110) surface is restructured to form {111} micro facets. Recent STM experiments at high gas pressures have observed similar effects on related systems. In particular, STM studies on the Pt(110) surface [57, 109, 112] have shown the formation of (111) micro-facets in the presence of oxygen.

7.7.3   Structure of the facets

Asymmetry observed in the intensity of the peaks from the micro-facets near a Bragg peak in figure 7.4 suggests that the there is some deviation from a perfectly bulk-like (111) surface. There is a shift in intensity to lower k that is likely to be due to a distortion of the facet possibly due to interstitial carbon. This shift in intensity cannot be explained by surface miscut resulting in a larger area of (11$\bar{1}$) facets than (111), as this would result in a systematic constant variation in integrated intensity of the facet truncation rods between

those arising from the (111) and (11$\bar{1}$) surfaces, and this was not observed. Two approaches to fit this intensity difference have been explored.

Firstly, truncation rods normal to the facets have been fitted using a simple model (figure 7.7) of the relaxation of the top layer of nickel atoms. The results of these fits shown in figure 7.9 give a relaxation of the top layer of 0.11Å. The width of the rocking scans of the facet truncation rods correspond to a correlation length of approximately 50Å. The effect of tilt of the rod on this width has been neglected. The error depends on the geometry of rod interception, but the maximum is $1/\cos\theta$ where $\theta = 35°$, which would give a maximum difference of 22%.

The second approach is to assume that the facets contained dissolved carbon, and are strained. In a heteroepitaxially grown film, the lattice mismatch can result in strain being relieved either by the formation of dislocation free faceted islands, called "hut clusters", or by dislocations. X-ray diffraction studies of germanium on silicon (001) [87, 117] "hut clusters" have determined some information on their structure. These "hut clusters" are similar to the microfacets observed in this experiment, and the procedure of Steinfort *et al.* [117] has been used to model the (111) facets on the nickel surface. In this analysis, it has been postulated that the strain is due to interstitial carbon absorbed in the nickel. The size obtained from this calculation is a base length of 100Å. The correlation length of 50Å for the facet face would give a base size of around 100Å, so the results are consistent.

These two simple models both suggest that there is some enlargement of the lattice in the facets. Studies of the interaction of the CO/Ni(111) at high temperatures would enable a more detailed model of the surface to be

measured. Both of the models for the facets are fairly simplistic, however there is not sufficient data for a more complex model to be used. In particular, the strained model assumes that the pyramid of nickel contains a uniform absorption of carbon, and that the underlying nickel contains none. While this may be an unphysical model, it can give some insight into the structure.

In the Ni(111)c(4×2)-CO reconstruction there is evidence for significant movement of the surface atoms [6, 78]. The disruption to the facets from perfect (111) surfaces is possibly due to this persisting after the removal of the CO, or the presence of interstitial carbon due to dissociation of the CO on the surface. An SXRD study of the CO/Ni(111) system at high temperatures and pressures would be able to study the surface in more detail and cast light on the structure of the surface after facet formation, and perhaps give some information on the mechanisms behind this faceting.

7.7.4   Catalytic importance facet formation

The formation of facets is relevant in catalysis as reaction rates can vary dramatically on different surfaces. For example in the synthesis of ammonia using an iron catalyst [111], or the reduction of ethane to methane over a nickel catalyst, Ni(100) is far more active than the close packed Ni(111) [45]. Studies have also shown dramatic rate differences in the hydrodesulphurisation of thiophene over rhenium [110].

Different surfaces can also change the reaction product. In the catalytic reforming of naptha, the product distribution is different depending upon whether Pt(111) or Pt(100) is used [110]. The formation of facets may there-

fore be important to the reaction product.

There is also evidence that steps on a surface are more reactive than the flat surface. Thermal desorption experiments have shown that rough surfaces, which have lots of steps, adsorb and decompose hydrocarbons at lower temperatures than flat surfaces [57]. The reason for this is likely to be that they have a lower coordination than those on terraces. Thus steps are expected to act as sites of special reactivity for adsorption, as sites of modified activation barriers for diffusion, and as sources or sinks for any removal or addition of mass on the surface [139]. Understanding of the mechanisms behind facet formation is therefore important.

7.7.5 Mechanism for formation of the facets

It is well known that nickel reacts with carbon monoxide forming the volatile $Ni(CO)_4$ (equation 7.6), indeed this reaction is used in the Mond process to refine nickel [141].

$$Ni + 4CO \longrightarrow Ni(CO)_4 \qquad (7.6)$$

Preferential etching of the (110) surface in this reaction to leave (111) facets is the likely mechanism of facet formation. (111) facets having a close packed face are likely to be more stable.

A number of reconstructions of CO on the Ni(111) surface are listed in the surface structure database [120]. A (2×2) [24] at low coverage, and $(\sqrt{3} \times \sqrt{3})R30°$ [66], $c(4×2)$ [6, 78] with coverages of 0.33 monolayer (ML) and 0.5 ML respectively.

At high CO pressure, the Ni(111)c(4×2)–CO reconstruction is most likely to be stable. In this reconstruction, CO molecules occupy threefold hollow sites [6, 78]. This is also the case in the lower coverage Ni(111)(2×2)–CO reconstruction [24]. In the previous chapter, the CO molecules in the Ni(110)-(2×1)–2CO reconstruction are described as occupying short bridge sites; they are however slightly displaced from these sites, and could be considered to be in threefold sites of a (111) microfacet, though they are slightly displaced from this because of interatomic repulsion due to the large size of the CO molecule. This may stabilise the (111) surface relative to the (110) surface.

Experiments to determine the rate of formation of nickel carbonyl (equation 7.6) by deGroot et $al.$ [25] reported the observation of (111) microfaceting due to the reaction of CO with Ni(110). These experiments were carried out at low pressure over a period of several days, and show (111) facets of base size around 1μm. They seemed to show that the formation of nickel carbonyl on the (110) surface was 1.3 times as rapid as that on the (111) surface, though later results by Lascelles and Renny [73] find the (111) surface more reactive. It is difficult to see how a greater rate of reaction on the (111) surface than the (110) would lead to the formation of facets. Thus while deGroot et $al.$ [25] find slow formation of facets at low pressure, our results find rapid formation of facets at high pressure. The results of deGroot thus provide evidence for preferential etching to produce nickel carbonyl being the mechanism for facet formation. These results thus support our proposed mechanism for facet formation being preferential etching of the surface.

7.8 Conclusions

X-ray diffraction measurements have been performed to measure the effect of heating on the Ni(110)-(2×1)-2CO surface. The experiments were carried out in-situ both in high vacuum conditions, 10^{-5} mbar, and high pressure conditions, 2.3 bar. The following conclusions were reached:

- At a pressure of 10^{-5} mbar, heating causes disordering of the surface at a temperature of approximately 50°C. This is consistent with the isostere of Madden *et al.* [52].

- At a pressure of 2.3 bar, when the sample is heated to 150°C, a major restructuring of the surface occurs resulting in the formation of micro-facets with {111} faces. AFM measurements (figure 7.11 [99]) support this view, though suggest a more complex surface structure.

- At 2.3 bar, the (2×1) reconstruction disappears as the (110) surface is destroyed, rather than by desorption from the surface.

- The base of the microfacets has a size of approximately 100Å.

- The facet surface is disrupted from the perfect {111} surface. This is consistent with relaxation of the surface layer, or more general expansion in lattice. One mechanism for this is dissolution of carbon in the facets.

- A mechanism for microfacet formation by preferential reaction of the (110) plane with carbon monoxide to form nickel carbonyl, $Ni(CO)_4$, has been proposed. This mechanism is consistent with a previous high

vacuum experiment where reaction of the carbon monoxide flowing over nickel (110) for a period of several days resulted in the formation of {111} microfacets [25].

These experimental findings above room temperature provide an example of a case where the results at high pressure differ dramatically from those at low pressure. This indicates the great value of *in-situ* high pressure experiments such as those described in this chapter.

Chapter 8

A surface X-Ray diffraction study of the cooling of the $c(8\times2)$ reconstruction of the InSb(001) surface

8.1 Introduction

This chapter presents the results of a surface X-ray diffraction and low energy electron diffraction study to measure the effect of cooling the $c(8\times2)$ reconstruction of the InSb(001) surface. No structural changes were observed on cooling from room temperature to 74K. Key features of the structure are derived from the data and suggest variations from the model of Jones *et al.* [62]. The measurements reported here provide evidence for the presence of dimers along both the long (a_1) and short (a_2) axes of the unit cell. Comparisons

are made with previous models and STM measurements.

8.2 Background

Indium antimonide is a compound III-V semiconductor with a narrow band gap (0.18eV). It has attracted much interest because of its potential technological applications in IR detection and high speed electronics. Epitaxial growth for the production of devices is commonly carried out on the (001) surface of III-V semiconductors [8, 80], typically with a V/III flux greater than 1 [4].

The phase diagram in figure 8.1 for the indium antimonide (001) surface shows that a number of reconstructions are formed under different growth conditions. The reconstructions are, in order of increasing antimony content, $c(8\times2)$, asymmetric (1×3), $c(4\times4)$, (1×1). A *pseudo* (4×3) has also been observed.

Dimerisation is a common feature of the (001) faces of elemental and zinc blende-type semiconductors [63]. The antimony rich $c(4\times4)$ reconstruction for example consists of $\approx \frac{3}{4}$ of a monolayer of antimony dimers [63].

8.2.1 The $c(8\times2)$ reconstruction

The $c(8\times2)$ reconstruction is indium rich [60] and observed at all temperatures up to the melting point of indium antimonide [80]. A $c(8\times2)$ reconstruction is also observed on the (001) surface of other III-V semiconductors such as gallium arsenide [8].

Although LEED pictures (such as figure 8.8) show reflections correspond-
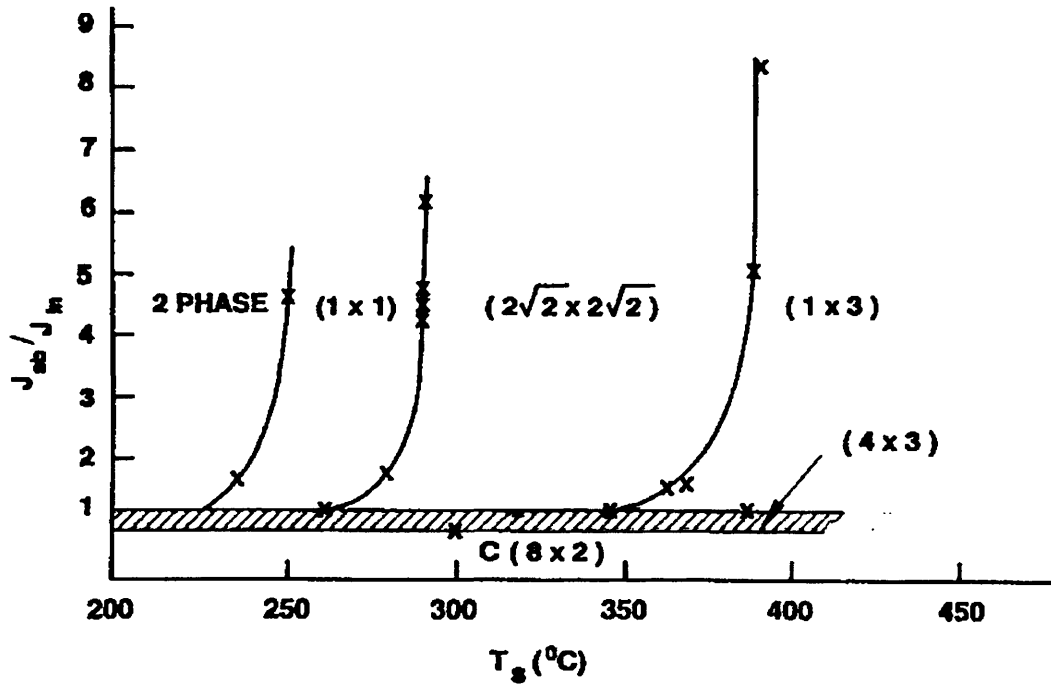
Figure 8.1: Phase diagram for surface reconstructions observed on InSb(001) as a function of the Sb/In arrival rate and surface temperature. Note that $(2\sqrt{2} \times 2\sqrt{2})$ is the primitive unit cell of the $c(4\times4)$ reconstruction. Reproduced from a paper by McConville *et al.* [80] with permission of the authors, Copyright 1990 by The American Physical Society.

ing to a $c(8\times2)$ unit cell, initial STM studies were only able to observe a (4×1) reconstruction (eg figure 8.2), though the empty state images of recent studies do show the full $c(8\times2)$ reconstruction [23, 121] (figure 8.3). The STM pictures show clear bright rows along the [110] direction on the surface in both filled state and empty state images.

Structures for the $c(4\times4)$ [63] and $c(8\times2)$ [62] reconstructions of the InSb(001) surface have been proposed by Jones after a surface X-ray diffraction study. The $c(8\times2)$ structure proposed by Jones consisted of indium chains oriented along the [110] axis separated by antimony dimers on the antimony-terminated bulk (figure 8.4,8.5). This model is consistent with recent STM images [23, 121] and represents a significant departure from the models previously suggested for the $c(8\times2)$ reconstruction on the (001) surfaces of any of the III-V compounds.

The arrangement of indium in the chains closely resembles that of the bulk metal, suggesting the chains form one-dimensional conducting paths. The possibility of quasi-1D conducting paths on top of a semi-insulator is of fundamental technological interest. Other examples of quasi-1D surface structures such as thallium on copper (001) [9] involve metallic substrates which tend to mask the conduction properties of these chains. The dramatic changes from the bulk in this structure may also explain why the $c(8\times2)$ surface, though well ordered, is not used as the starting point for the growth of device structures.

Figure 8.2: Filled state STM image of the $c(8\times2)$ reconstruction of indium antimonide showing bright double rows along the [110] direction (labelled [0$\bar{1}$1] on the diagram as the surface is described as (100) instead of (001). Reproduced from a paper by McConville *et al.* [80] with permission of the authors, copyright 1990 by The American Physical Society.
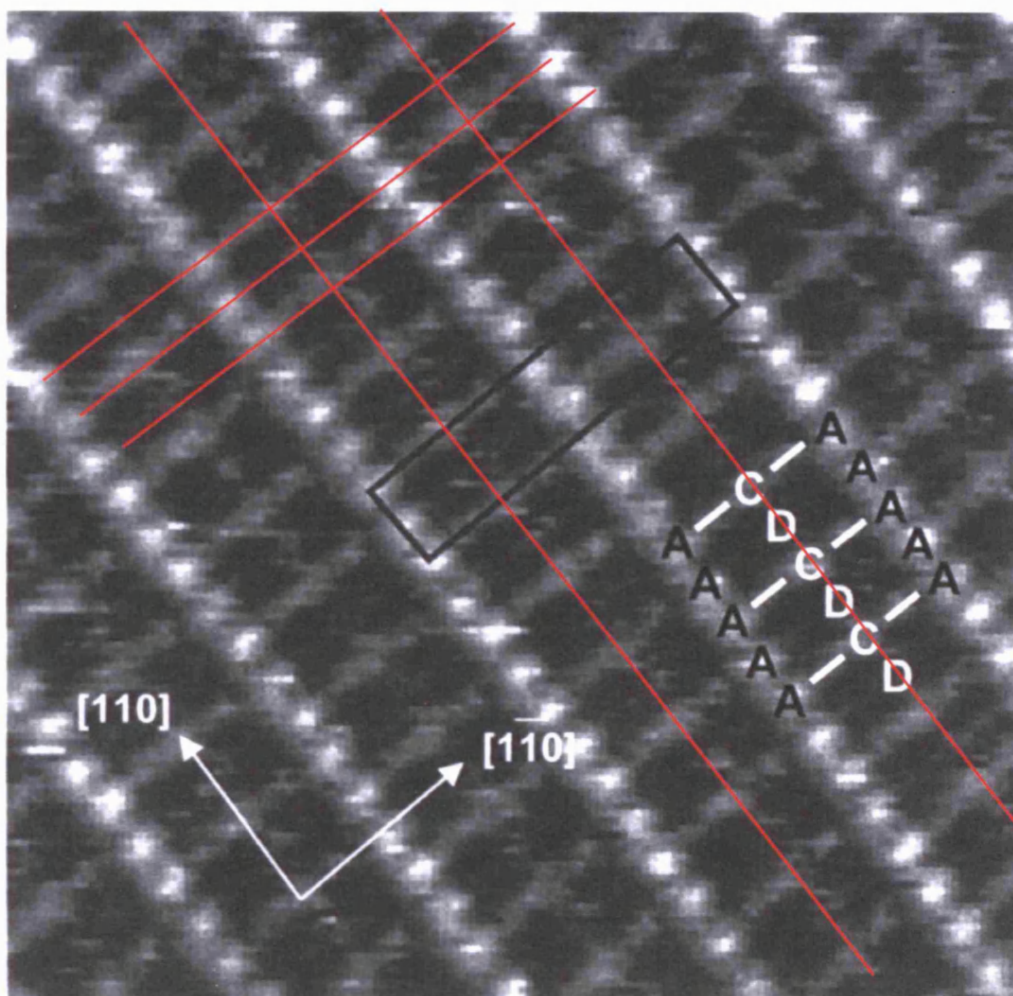
Figure 8.3: Empty states image (90Å×90Å) of InSb(001)-c(8×2) with mirror planes shown in red. Based on a paper by Davis *et al.* [23] with the permission of the authors.
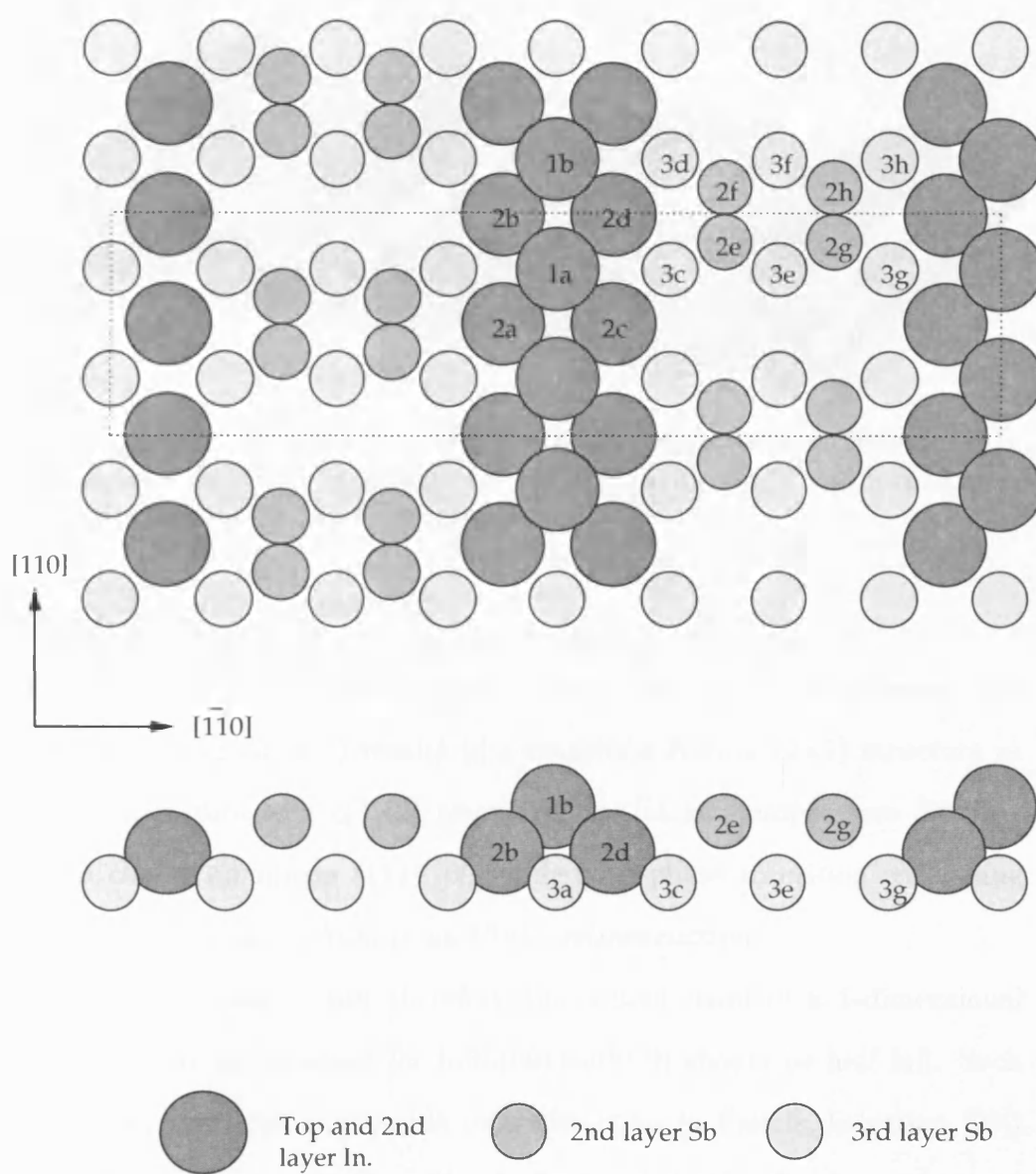
Figure 8.4: Model proposed by Jones et al [62] for the $c(8\times2)$ reconstruction of the (001) surface of indium antimonide. The broken line marks the c(8x2) unit cell
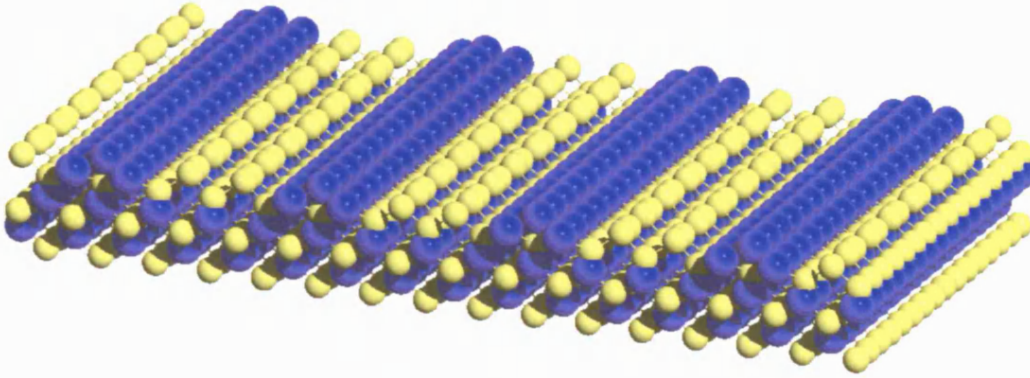
Figure 8.5: Jones's Model of the $c(8\times2)$ reconstruction. Indium is blue, and antimony is yellow. The indium chains that could form 1d conducting paths can be seen in blue.

8.2.2   Effect of cooling

Cooling induces structural changes on some semiconductor systems. For example, cooling Ge(001) results in a transition from a (2×1) structure at room temperature to a $c(4\times2)$ reconstruction at low-temperature [36, 65]. Indium chains on silicon (111) [69] undergo a phase transition on cooling from a (4×1) reconstruction to an (8×2) reconstruction.

Indium is trivalent and therefore the second band of a 1-dimensional chain structure as proposed for InSb(001)-$c(8\times2)$ should be half full. Such a structure would be susceptible to a distortion (a Peierls distortion [96]) which opens a gap at the Fermi level. Such a distortion has been observed for thallium on copper (001) [9]. The aim of this work was to search for this distortion.

8.3 InSb Lattice

8.3.1 Symmetry of the InSb(001) surface

Indium antimonide has the zinc blende structure and is in space group 216 $F\bar{4}3m$ [55]. A projection along [001] has symmetry $p4mm$, and the (001) surface has symmetry $p2mm$. The $c(8\times2)$ reconstruction has $c2mm$ symmetry [62] which is a subgroup with a larger unit cell of the $p2mm$ symmetry of the surface. The symmetry relations of this space group are given in table 8.1. Positions of reduced multiplicity are those where the symmetry operations map points onto themselves. This restricts the position of atoms - an atom on a mirror plane cannot move off that mirror plane without breaking the symmetry. It also means that atoms cannot be too close to mirror planes or twofold axes unless they are actually on these planes or axes.

The $c(8\times2)$ unit cell, and $c2mm$ symmetry, has been observed in STM studies by Davis $et\ al.$ [23] and Varekamp $et\ al.$ [121]. Because it has a centred unit cell, only the reconstruction peaks with $8h + 2k = 2n$, with n integer, are present. This is shown in appendix E. The systematic absence of the peaks is confirmed by the results of LEED (figure 8.8, 8.9) and also by reciprocal space scans (figure 8.11). The intensity of the diffraction peaks measured by X-ray diffraction in this experiment were consistent with $c2mm$ symmetry.

Multiplicity	Wyckoff letter	Site Symmetry	Position
8	f	1	(x,y) (-x,-y) (-x,y) (x,-y)
4	e	.m.	(0,y) (0,-y)
4	d	..m	(x,0) (-x,0)
4	c	2..	$\left(\frac{1}{4},\frac{1}{4}\right)$ $\left(\frac{3}{4},\frac{1}{4}\right)$
2	b	2mm	$\left(0,\frac{1}{2}\right)$
2	a	2mm	(0,0)
and as above +(1/2,1/2)			
Asymmetric unit cell		$0 < x < \frac{1}{4}$ and $0 < y < \frac{1}{2}$ or $0 < x < \frac{1}{2}$ and $0 < y < \frac{1}{4}$ or $0 < x < \frac{1}{2}$ and $0 < y < x$		

Table 8.1: c2mm symmetry table [48]

Figure 8.6: Symmetry diagram for *c2mm* symmetry of the *c*(8×2) reconstruction. Symmetry elements shown in red, with mirror planes as solid lines and glide planes by dotted lines. Twofold axes are also indicated. Lightly shaded is the asymmetric unit cell which consists of two unreconstructed unit cells.

Real space: Reciprocal space:

$$\mathbf{a_1} = \tfrac{1}{2} \; [\bar{1}10]_{cubic}$$
$$\mathbf{a_2} = \tfrac{1}{2} \; [110]_{cubic}$$
$$\mathbf{a_3} = \tfrac{1}{2} \; [001]_{cubic}$$

$$\mathbf{b_1} = (1\bar{1}0)_{cubic}$$
$$\mathbf{b_2} = (110)_{cubic}$$
$$\mathbf{b_3} = (001)_{cubic}$$

with   with

$$|\mathbf{a_1}| = |\mathbf{a_2}| = \frac{a_0}{\sqrt{2}} = 4.581\text{Å}$$
$$|\mathbf{a_3}| = a_0 = 6.479\text{Å}$$

$$|\mathbf{b_1}| = |\mathbf{b_2}| = \frac{2\sqrt{2}\pi}{a_0} = 1.3715\text{Å}^{-1}$$
$$|\mathbf{b_3}| = \frac{2\pi}{a_0} = 0.9698\text{Å}^{-1}$$

Table 8.2: Relationship between surface unit cell vectors used to describe the InSb(001) surface, and the conventional cubic unit cell.

8.3.2 Coordinate transforms

For the analysis of the diffracted intensity, the atomic structure of the InSb(001) surface is described by a tetragonal unit cell defined by three base vectors $\mathbf{a_i}$, and corresponding reciprocal lattice vectors $\mathbf{b_i}$. Using this convention $\mathbf{a_1}$ and $\mathbf{a_2}$ are in the surface plane, and $\mathbf{a_3}$ is perpendicular to the surface. The relationship of these vectors to the conventional face centred cubic cell is given in table 8.2.

The momentum transfer vector $\mathbf{Q}$ is defined by the Miller indices (hkl) with $\mathbf{Q} = h\mathbf{b_1} + k\mathbf{b_2} + l\mathbf{b_3}$. General reflections are labelled by (hkl) and in-plane reflections $(l \approx 0)$ by (hk)

8.4   Explanation of the $k = \frac{5}{2}$ "missing" reflections

The model of Jones *et al.* [62] predicts the diffraction peaks with $k = \frac{5}{2}$ will be weak. The only contribution to the $k = \frac{n}{2}$ order reflections comes from the antimony dimers (labelled 2e,2f,2g,2h in figure 8.4), as the other atoms in the model only contribute to a (4×1) reconstruction. The structure factor, $F(hkl)$ for a reflection is given by:

$$F(hkl) = \sum_{\text{unitcell}} f e^{2\pi i(hx+ky+lz)} \qquad (8.1)$$

Taking the coordinate origin as the centre of these four antimony atoms, they have positions $(x, y), (x, -y), (-x, y), (-x, -y)$. All the atoms have the same z coordinate. The structure factor is then as given in equation 8.2.

To simplify the formulae, the other four antimony atoms in the unit present by the translational symmetry of $(\frac{1}{2}\frac{1}{2})$ are not considered. Appendix E shows that their only contribution is to cause the systematic absence of $\frac{h}{8}\frac{k}{2} = 2n + 1$ reflections.

$$
\begin{aligned}
F(hkl) &= \left[e^{2\pi i(hx+ky+lz)} + e^{2\pi i(hx-ky+lz)} + \right. \\
&\qquad \left. e^{2\pi i(-hx+ky+lz)} + e^{2\pi i(-hx-ky+lz)} \right] \\
&= e^{2\pi ilz} \left[\left(e^{2\pi ihx} + e^{-2\pi ihx} \right) \left(e^{2\pi iky} + e^{-2\pi iky} \right) \right] \\
&= 4e^{2\pi ilz} \cos(2\pi hx) \cos(2\pi ky) \\
&= 0 \quad \text{when:}
\end{aligned}
\qquad (8.2)
$$

$$cos(2\pi ky) = 0$$

$$\Rightarrow \quad ky = \frac{2n+1}{4}$$

Taking $k = \frac{5}{2}$ which corresponds to the missing reflections, if the antimony atoms have a position of $y = \frac{2n+1}{10}$ and a separation of twice that. If $n = 1$, this separation corresponds to 2.74Å for the missing reflections. In the model of Jones *et al.*, the separation is measured to be 2.72 ± 0.07Å. The dimers are assigned to antimony, as the separation is very close to the nearest neighbour separation in bulk antimony of 2.87Å, whereas the nearest neighbour separation in bulk indium is 3.24Å[143].

Most previous models have suggested dimerisation occurs by bond bending, and the preferred direction for this to occur for antimony is along $\mathbf{a_1}$, not along $\mathbf{a_2}$ as in the model of Jones *et al.*. This is explained in terms of antimony dimers on an antimony layer, though this is difficult to reconcile with an indium rich surface [60, 80]. It seems more likely that this near zero intensity is due not just to pairs of atoms, but to a more complex structure of three or more atoms. Indeed the fractional order rods shown later in the chapter provide evidence for this.

8.5 Experimental

8.5.1 Sample

The InSb(001) wafer was prepared by cleaning the wafer, then epitaxially growing InSb, followed by capping with a protective antimony overlayer ap-

proximately 1000Å thick. This protects the sample from contamination when transferring to the UHV chamber on the diffractometer. A small miscut has been found to improve device properties [61], so this sample had a miscut of 1.4°. A sample with dimensions 8×8×0.5mm was cleaved from the wafer, and mounted on a molybdenum backing plate using indium solder (fig 8.7).
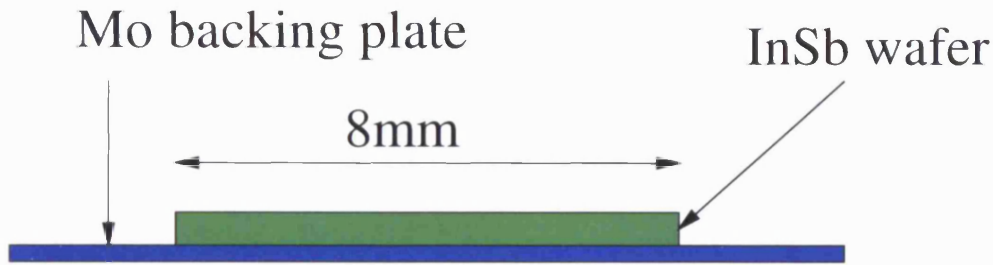
Figure 8.7: Schematic of InSb(001) sample on a Molybdenum backing plate

8.6 Cooling InSb(001)-c(8×2): a LEED study

8.6.1 Experimental

The LEED experiments were performed in a UHV chamber described by Nicklin *et al.* [86]. The antimony-capped indium antimonide sample was cleaned by several cycles of sputtering followed by annealing. After each cycle, LEED was used to examine the surface. When a well ordered surface was obtained, photographs were taken of the LEED pattern at various energies, at both room temperature and when the sample was cooled with liquid nitrogen. Although it was not possible to measure the temperature directly, previous experiments [86] show that the sample reaches a temperature of approximately 86K on cooling with liquid nitrogen. Some patterns were

subsequently photographed after the sample had warmed up to room temperature. There were no noticeable differences, indicating that the sample order had not been increased by cooling.

8.6.2   LEED Results

A comparison between sputtering at room temperature followed by annealing, and sputtering at elevated temperature, showed a much sharper LEED pattern in the latter case. This is consistent with work by Jones *et al.* [64] on oxide removal from indium antimonide, and suggests that this procedure is valuable even for capped samples.

The LEED patterns of the $c(8\times2)$ reconstruction are shown at room temperature, and when cooled by liquid nitrogen, in figure 8.8. The LEED patterns at low temperature show brighter diffraction spots, especially at higher energies. This is to be expected, as cooling reduces the thermal vibration, and hence the Debye-Waller factor, and therefore reduces thermal diffuse scattering. Other than this brightening of the diffraction spots, there are no changes visible in the diffraction pattern between room temperature and liquid nitrogen cooled. There is thus no major structural change. The symmetry of the diffraction pattern observed is *c2mm*.

The model of Jones *et al.* predicts that the diffraction spots at $k = \frac{5}{2}$ are absent due to the spacing of the antimony dimers in the model. These spots are not visible at 76.7eV or 96.5eV in figures 8.8, 8.9 even when cooled; this is consistent with the model of Jones.
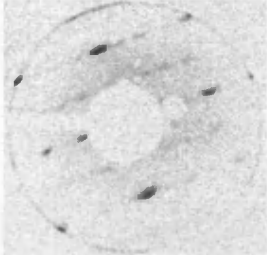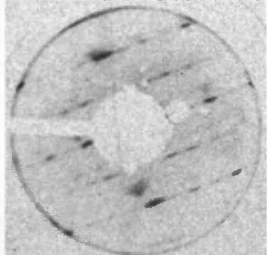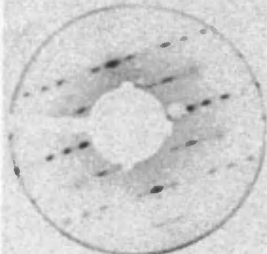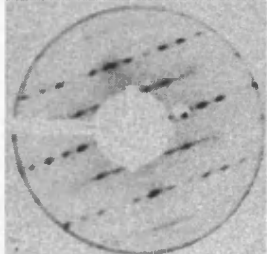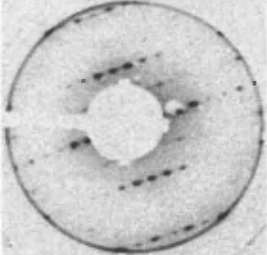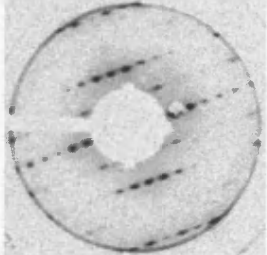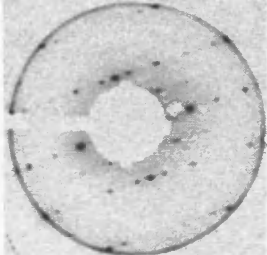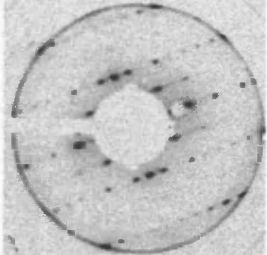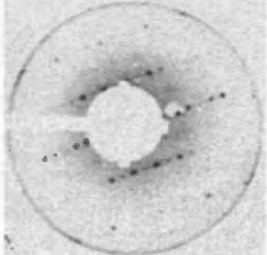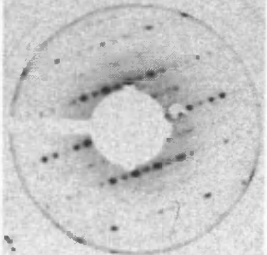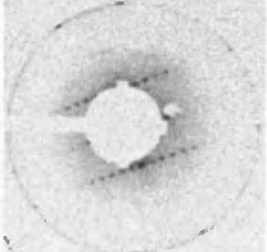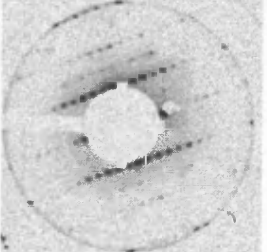
Energy (eV)	Room Temperature	Liquid Nitrogen cooled (≈ 86K)
22.8		
31.8		
44.3		
52.7		
76.7		
96.5		

Figure 8.8: LEED at liquid nitrogen temperature and room temperature
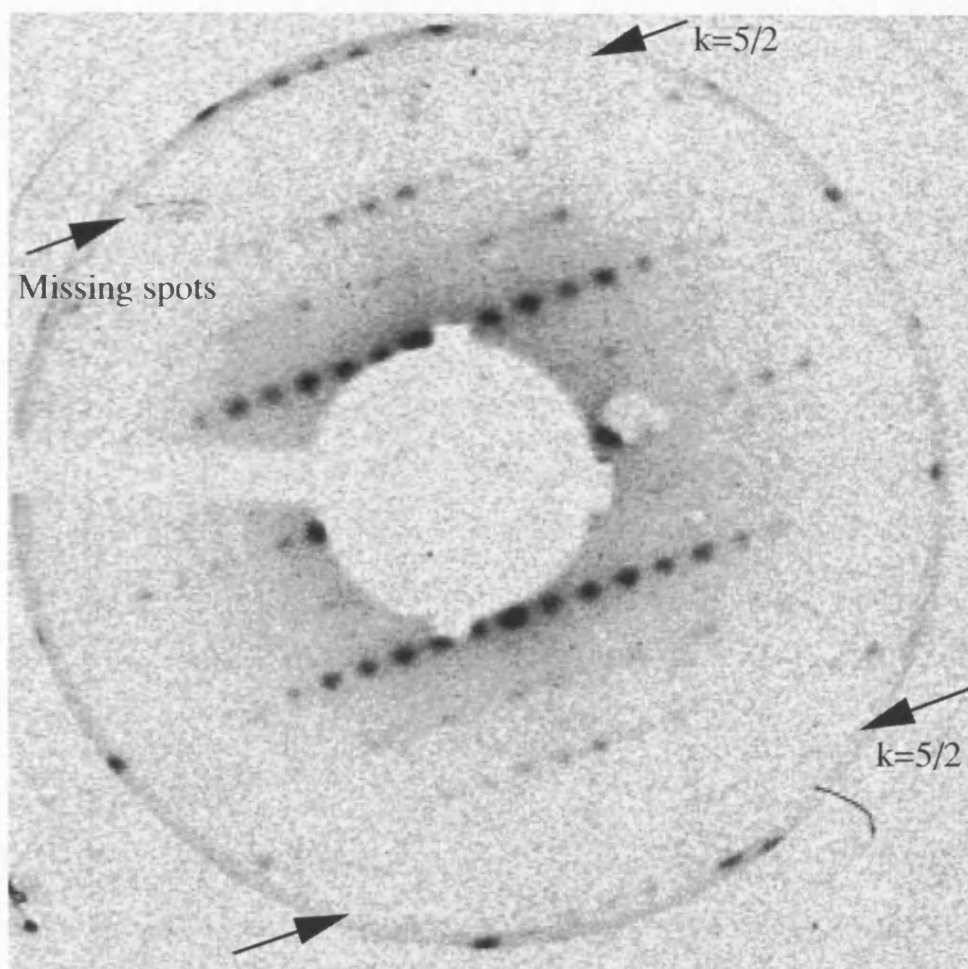
Figure 8.9: LEED pattern of InSb(001)-$c(8×2)$ at 96.5eV. A missing row of diffraction spots at $k = \frac{5}{2}$ is labelled

8.6.3 LEED Conclusions

No major structural changes occur on cooling to low temperature, and the c2mm symmetry of the diffraction pattern is maintained. The diffraction spots however are brighter due to reduced thermal vibration and hence reduced Debye-Waller factor.

8.7 Cooling InSb(001)-c(8×2): an SXRD study

8.7.1 SXRD

Six days of beamtime were allocated on the surface diffraction beamline [35] ID 3 at the ESRF in Grenoble to study the structural changes that occur on cooling of the c(8×2) surface of InSb(001). A wavelength of 1.209Å was selected using a sagittally focused double-crystal Si(111) monochromator [19]. This wavelength corresponds to the third harmonic of the undulator.

8.7.2 Sample

The antimony capped InSb(001) sample was mounted in the UHV chamber and outgassed. Cycles of argon bombardment (500eV, ≈ 30μAcm^{-2}) and annealing at 250°C were used to remove surface contamination (mainly carbon and oxygen). Auger Electron Spectroscopy (AES) was used to check the level of contamination, and six cycles consisting of 30 mins of bombardment followed by 15 mins of annealing were necessary to remove the surface contamination. The sample was then heated to 300°C to desorb the antimony capping layer. Finally, the sample was sputtered at 350°C while the intensity

of the (1 1.25 0.2) reconstruction peak was monitored.

After the intensity of this reconstruction peak was maximised and the sample cooled to room temperature, a data set of in-plane and out of plane data, as detailed below, was measured. The sample was then cooled to 74K using pumped liquid nitrogen, and a second data set was taken at this temperature.

8.7.3 Diffraction Measurements

Initially, a room temperature data set was measured to enable a thorough comparison with the low temperature data. A total of 212 in-plane fractional order reflections were measured, resulting in 99 non-equivalent reflections. In addition, five integer order rods were measured.

The sample was then cooled to 74K. Following a realignment, 274 in-plane fractional order reflections were measured, resulting in 130 non-equivalent reflections. In addition, five integer order and four fractional order rods were measured. Friedel's law [105] (equation 8.4) was used to combine the these into two fractional order, and two integer order rods extending over both positive and negative l values.

$$|F(\mathbf{q})| = |F(-\mathbf{q})| \qquad\qquad (8.3)$$

$$|F(hk\bar{l})| = |F(\overline{hk}l)| \qquad \text{Friedel's rule} \qquad (8.4)$$

The (1.25 1 0.2) peak was regularly scanned to monitor surface degradation. The intensity of this peak dropped by a factor of two over the 24 hours

of measurement.

8.7.4 Diffraction Setup

Often in surface X-ray diffraction, the sample is flooded by the incident beam with the pre- and post- sample slits defining the active sample area (see section 5.1.2). If the in-plane scattering angle, 2θ, is small, the X-ray beam visible to the detector extends off the sample, and an additional correction factor for the sample size is necessary. Although a correction for this is included in ANA for a circular sample, correction for a square sample is not included, and would need to take into account the sample orientation as well as dimensions; it would also be subject to errors if the sample was not aligned exactly in the centre of the diffractometer. The wavelength and slit settings were chosen to avoid the need for these correction factors and thereby reduce the possibility systematic errors and uncertainties with them. In the experiment described in this chapter, the width of the incident beam (ie perpendicular to the sample) defined the illuminated area. The angle of the incident beam to the sample surface, β_{in} was 1° for all scans except the low temperature out of plane scans where it was 2° as the sample seemed to be held less rigidly at this temperature.

At angles near the critical angle, $\beta_c = 0.25°$, small alignment errors will lead to significant systematic errors in the measured intensity. To eliminate these errors, peaks corresponding to exit angles less than three times the critical angle were rejected (ie $\beta_{out} < 0.75°$). This was a particular problem in this experiment due to the sample miscut. In the future, it is anticipated that

more precise alignment, possibly by measuring the position of the specularly reflected beam, will allow the use of the increased intensity and reduced background near the critical angle.

Diffracted intensities were measured by setting the crystal and detector to fulfil the diffraction condition and then rotating the crystal around the sample surface normal by rotating the diffractometer θ axis.

8.7.5   Data reduction

Analysis of surface X-ray diffraction data takes place in two stages. First, structure factors are calculated by integrating the measured intensities and applying correction factors. Second, a model structure is fitted to these structure factors using techniques such as the Patterson function in the computer program ROD [123].

Peak Integration

As can be seen from figure 8.10, the peak shape is neither Lorentzian, nor Gaussian, but contained components of each. A Lorentzian or Gaussian peak shape is due to a correlation function on the surface that is exponential or Gaussian respectively. A Gaussian component may also arise due to a contribution from the instrumental resolution. To obtain the most accurate results, the peak was therefore numerically integrated using the following procedure: the background was calculated by removing the centre ($\pm 2 \times$ $HWHM_{Gaussian}$) and fitting a Gaussian profile to the remaining points. The integration range was $\pm 12 \times HWHM_{Lorentzian}$ fitted to the peak - this will

contain 95% of the intensity for a Lorentzian profile, whilst minimising the effect of errors in the background.

Once the peaks have been integrated, the structure factor is calculated by taking the square root of these integrated intensities and applying the resolution and geometrical corrections described by Vlieg [125, 126]. This was performed using the computer program ANA described in section 5.1.2 and in reference [124].

(a) Gaussian fit with background   **(b)** Lorentzian fit with background
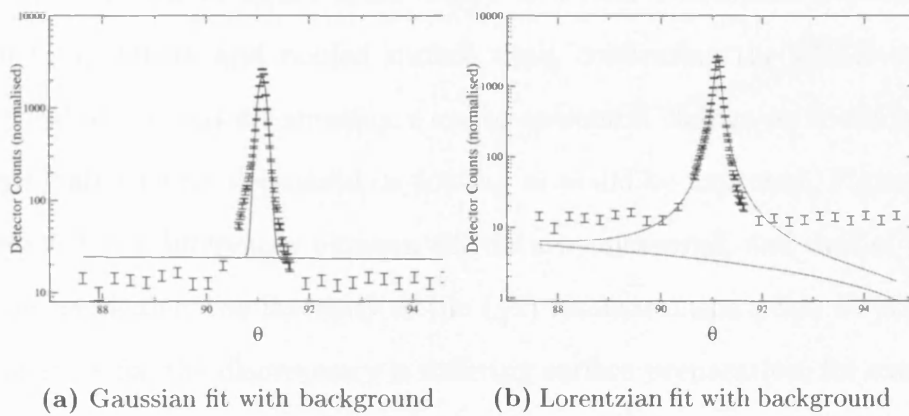
Figure 8.10: Fit to the peak shape of the $\left(\frac{5}{4}1\frac{1}{5}\right)$ reconstruction peak. The peak shape contains both Gaussian and Lorentzian components.

8.8 Results

8.8.1 Reciprocal space scans

Reciprocal space scans along the $(h0)$, $(h\frac{1}{2})$ and $(0k)$ axes performed after cooling the $c(8\times2)$ reconstruction are shown in figure 8.11. The scans clearly show the presence of $8h + 2k = 2n$ diffraction peaks; the absence of other

sharp peaks clearly indicating that the cell is a centred unit cell. The weak diffuse half order peak at $(0\frac{1}{2})$ is due to the presence of $c(4\times4)$. As this peak is weak and diffuse, it is likely only to have contributed to the background, and therefore had no influence on the analysis.

In-plane scans

A comparison between the data measured at room temperature, and cooled to 74K, is shown in figure 8.12. There is a clear correlation between the room temperature and cooled surface data, confirming the LEED results described above and discounting a major structural change on cooling. The Debye-Waller factor decreased on cooling as would be expected. Figure 8.13 however shows differences between the data we measured, and that of Jones [62], in particular, the intensity of the $(\frac{7}{4}1)$ reconstruction peak. A possible explanation for the discrepancy is differing surface preparation, for example a different amount of argon bombardment or annealing. This might lead for example to a difference in the antimony content of the surface. Indeed it was to avoid this sort of problem that a reference data set was measured at room temperature. Jones [63] prepared the $c(4\times4)$ reconstruction under antimony flux, and used further argon bombardment and annealing to produce the $c(8\times2)$ surface.

The $k = \frac{5}{2}$ reconstruction peaks are predicted to be very weak by the model of Jones [62] due to the antimony dimer separation (section 8.4). Figure 8.14 shows the $(\frac{15}{8}\frac{5}{2}\frac{1}{5})$ reconstruction peak measured at 74K is weak, but clearly present. Other peaks with $k = \frac{5}{2}$ are also present, though weak as can be seen from figure 8.12. These weak peaks are significant, as they pinpoint
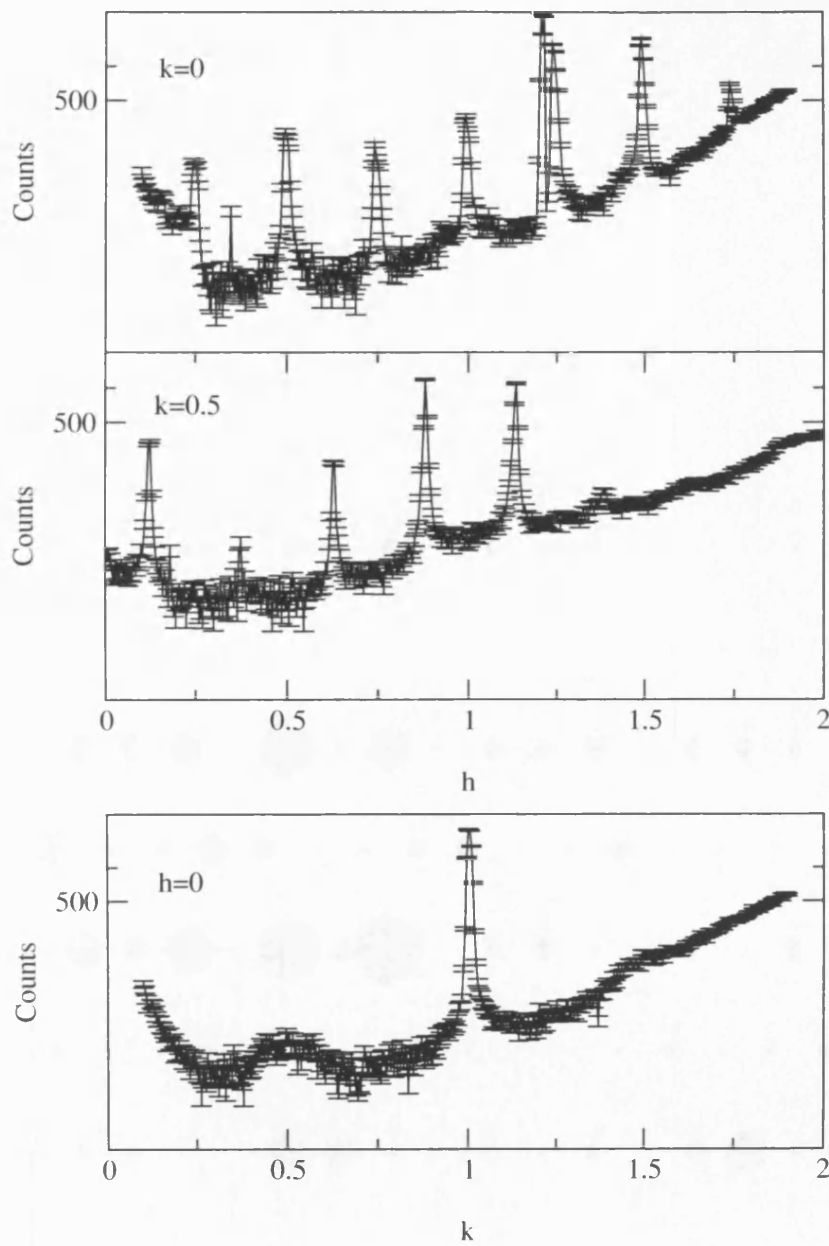
Figure 8.11: Reciprocal space scans on cooled InSb(001) showing $c(8\times2)$ reconstruction peaks. The presence of $\left(\frac{2n}{8}0\right)$ and $\left(\frac{2n+1}{8}\frac{1}{2}\right)$ reconstruction peaks confirms the structure is $c(8\times2)$.
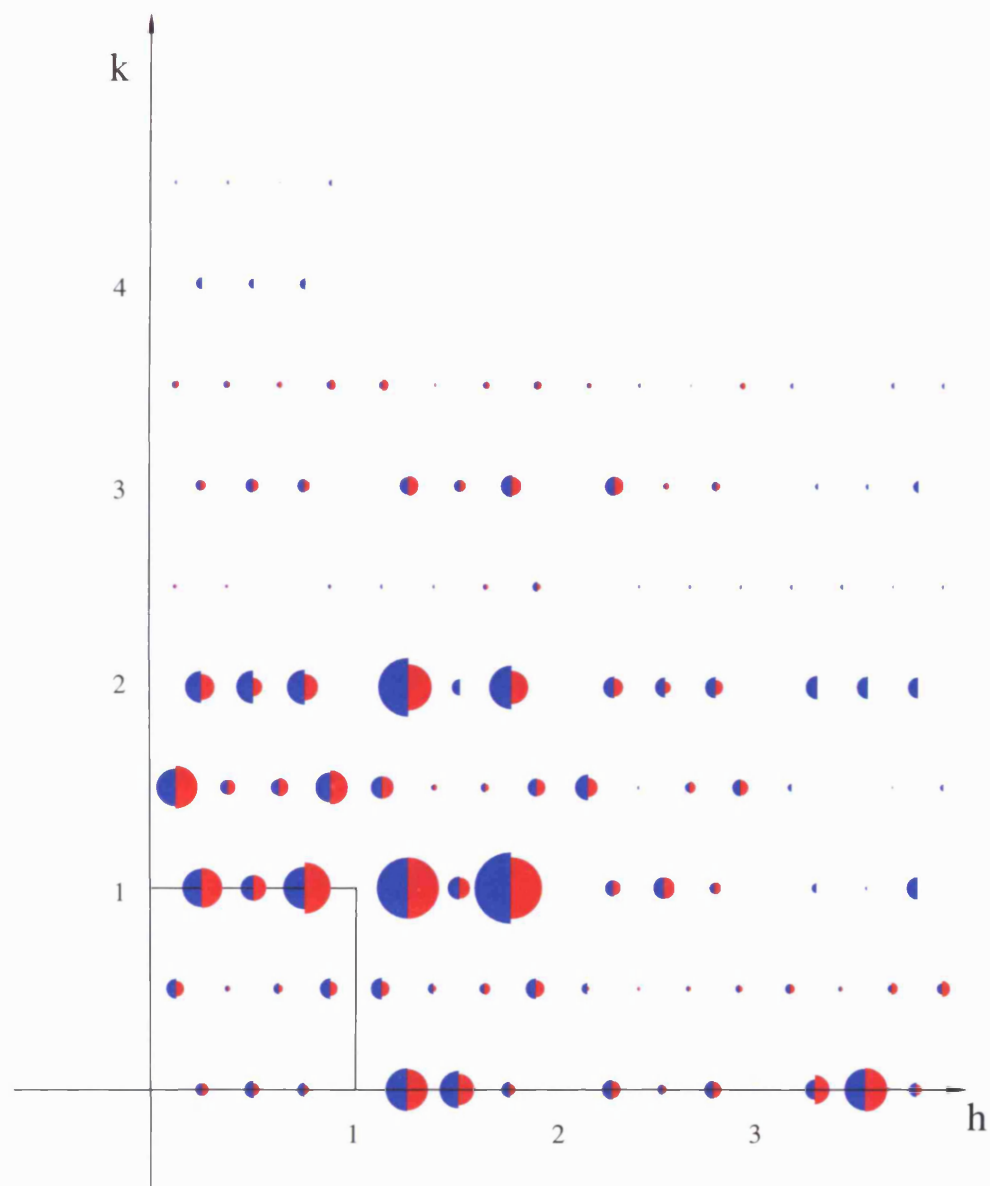
Figure 8.12: Experimentally measured structure factors scaled to $(\frac{5}{4}1\frac{1}{5})$ peak. Structure factor is represented by radius, integrated intensity by area. Sample cooled to 74K shown in blue on the left, room temperature in red.
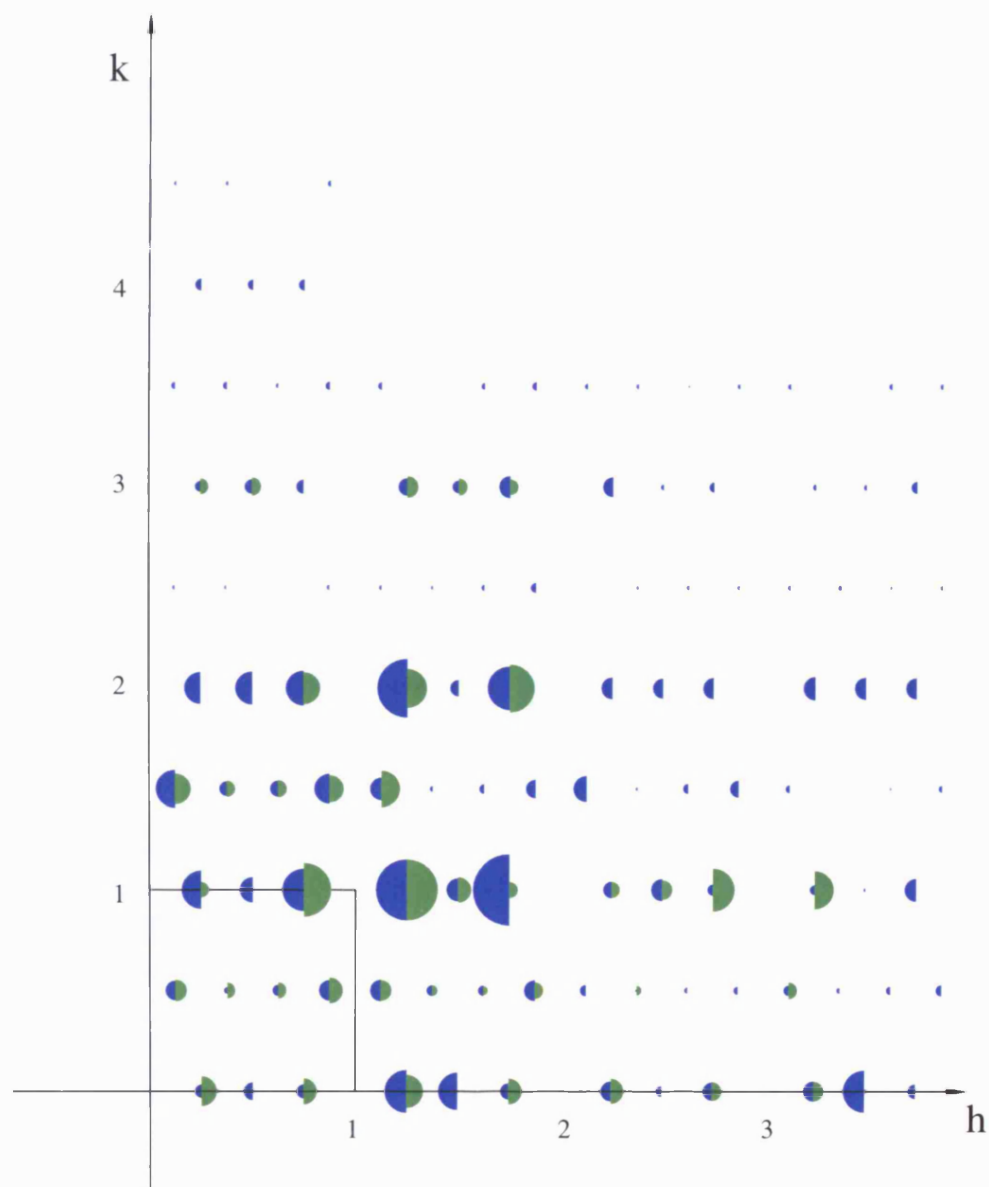
Figure 8.13: Comparison between experimentally measured structure factors and those measured by Jones et al [62] scaled to $\left(\frac{5}{4}1\frac{1}{5}\right)$ peak. Structure factor is represented by radius, integrated intensity by area. Data measured at 74K is shown in the lefthand semicircles in blue, data measured by Jones in green.

a particular distance present in the reconstruction. In the model of Jones *et al.*, for example, they fix the spacing of the antimony dimers.
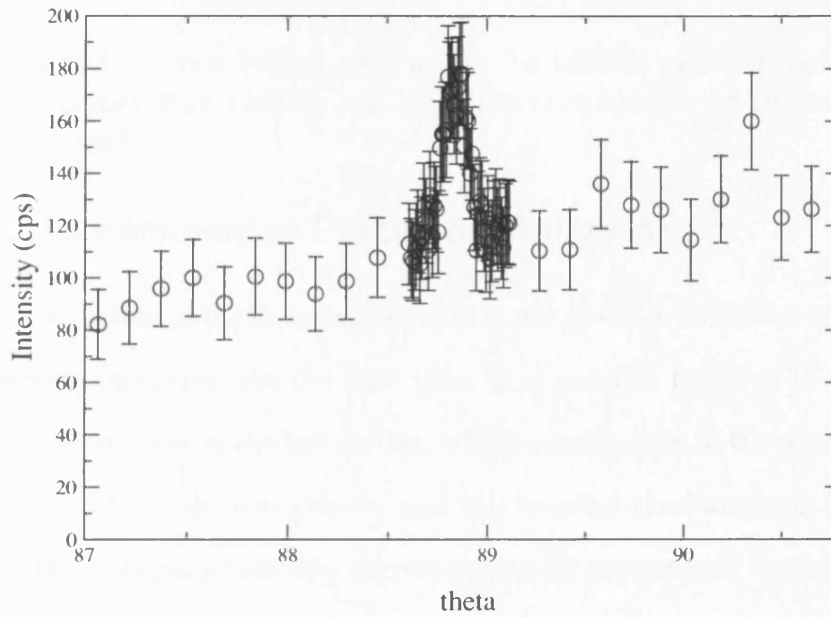
Figure 8.14: Rocking scan of the $(\frac{15}{8}\frac{5}{2}\frac{1}{5})$ reconstruction peak measured at 74K. This peak is clearly present, though weak.

8.8.2   Debye-Waller Factor

As discussed in section 3.5, thermal vibration causes a reduction in the integrated intensity of diffraction peaks. Debye-Waller factors shown in table 8.3 at room temperature and 74K were calculated from the parameterisation by Gao and Peng [40].The bulk indium and antimony atoms were constrained at these values in the fitting procedure. The Debye-Waller factors for surface atoms were fitted, because surface atoms have different, usually weaker, bonding to those in the bulk and therefore have a larger thermal vibration than bulk atoms.

Element	Temperature		Ratio
	74K	293K	
Indium	0.3708	1.342	3.62
Antimony	0.3132	1.120	3.58

Table 8.3: Debye Waller parameters for indium and antimony at room temperature (293K) and 74K (the temperature of the cooled InSb sample).

8.8.3 Experimental Patterson functions

Because of the loss of phase information it is not possible to fourier transform the structure factors to get the structure. It is possible however to compute the fourier transform of the intensities, which corresponds to the autocorrelation function of the electron density and this is called the Patterson function. Peaks in the Patterson function correspond to an interatomic vector. Figure 8.15 shows the Patterson functions calculated from the experimental indium antimonide data at room temperature and 74K. The reduced unit cell contains all the peaks not related by symmetry. There are several equivalent choices for this cell, (see table 8.1) one of which is shown in the figures by a triangle.

The Patterson functions for the room temperature, and low temperature data (figs 8.15(a), 8.15(b)) show the same features; these features are better defined in the low temperature measurements due to reduced thermal vibration, and also the larger data set. There is thus no evidence of a structural change on cooling.

A comparison between the Patterson functions of the experimental data, and the model and data of Jones *et al.* [62] (fig 8.16) shows marked similarities. There are however differences between the model of Jones and the

(a) 74K   (b) Room Temperature
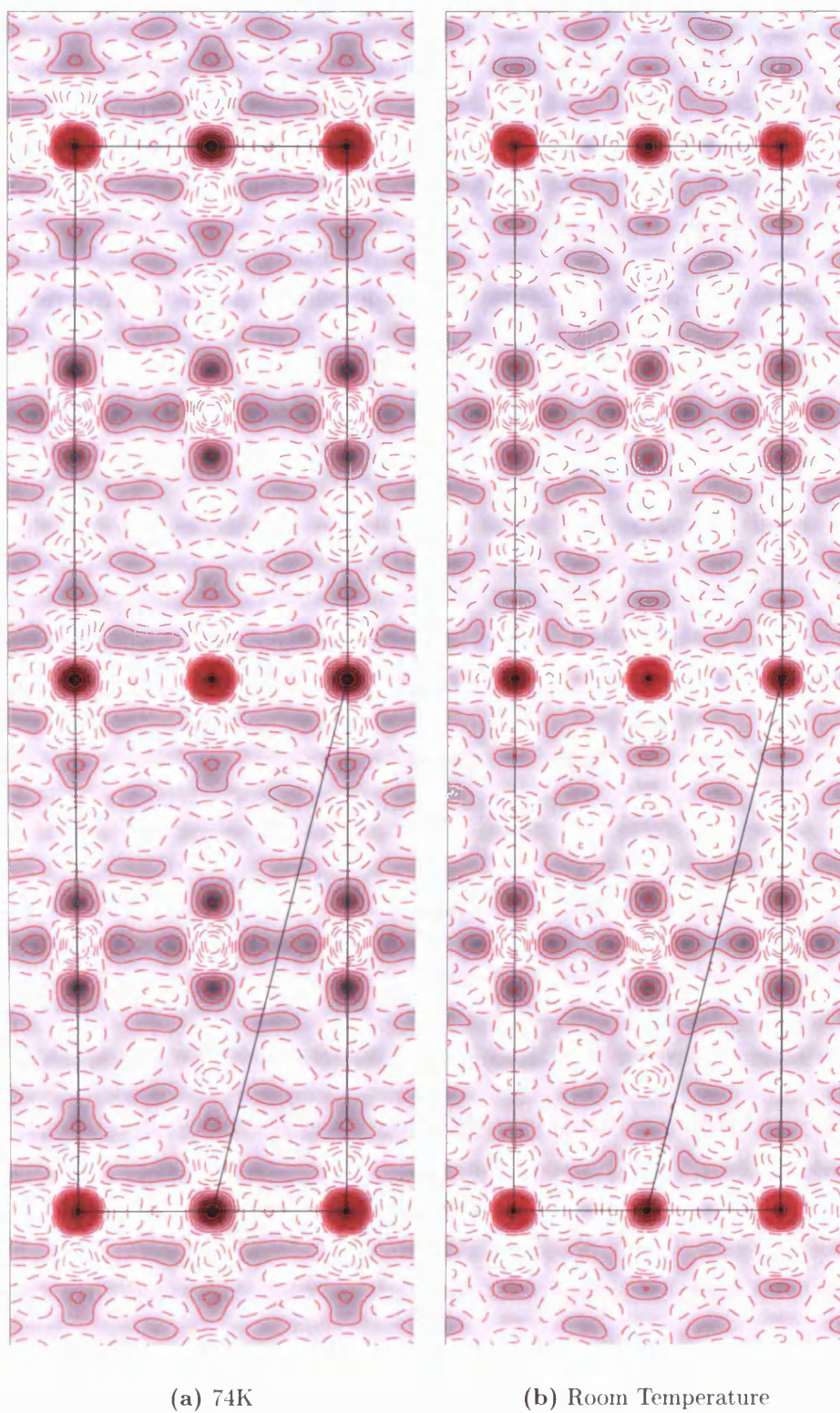
Figure 8.15: Patterson map for InSb(001)c(8×2). Full unit cell shown by black rectangle, asymmetric unit cell by black triangle. Dotted contours show negative peaks

data. The coordinates of the points labelled in this figure are given in table 8.5.

Fractional order rods

Figure 8.17 shows a comparison of the fractional rods with the data of Jones. It is clear that the model of Jones doesn't fit some of the features of the fractional rods. In particular in Jones's model, the (0.875 1.5 l) rod is contributed to only by the antimony dimers. These dimers are at one level, and would produce a rod profile shaped like figure 8.17(d) with no oscillations, whereas oscillations are observed in the experimental data in figure 8.17(b). Similarly for the (1.25 1 l) rod, the structure is different from that predicted by Jones *et al.*. From this it is possible to conclude that the reconstruction is deeper than that suggested by Jones, and that the $k = \frac{n}{2}$ peaks are due to more than one layer of atoms.

8.8.4 Effect of sampling on Patterson functions

The Patterson function is sensitive to the data used to generate it. In surface diffraction, some in-plane peaks have a contribution both from the surface, and from the CTR. As it is not possible to remove this CTR component, these peaks are usually excluded from the analysis and a "fractional" Patterson function is used. Excluding these peaks implicitly sets them to zero, and results in regions of negative intensity in the Patterson. It has been shown [10] that all peaks in the fractional Patterson are peaks in the full Patterson. It is certainly possible to compare the experimental Patterson function with
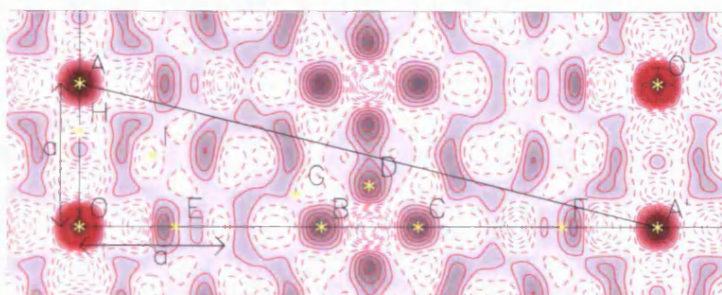
(a) 74K - This study
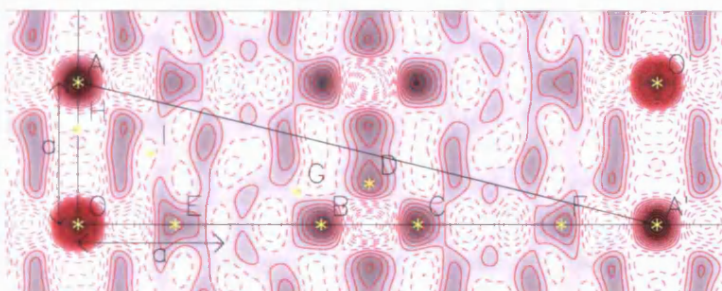
(b) Room Temperature - This study
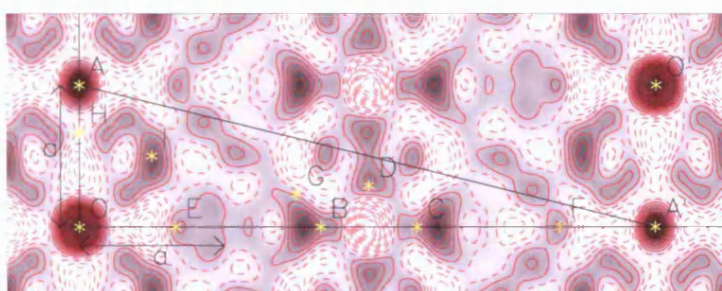
(c) Jones's Data (Room Temperature)
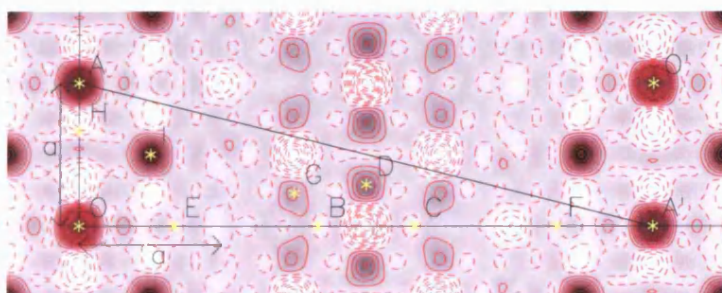
(d) Theoretical - Jones Model (Cold data points)

Figure 8.16: Patterson maps for indium antimonide
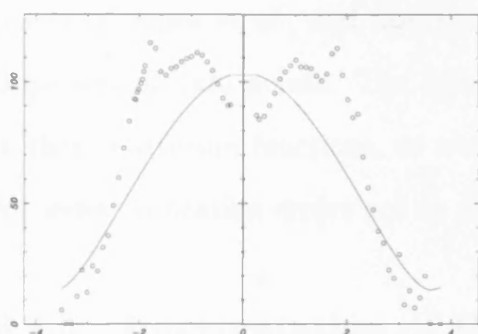
(a) (1.25 1) rod - Experimental data and Jones's model
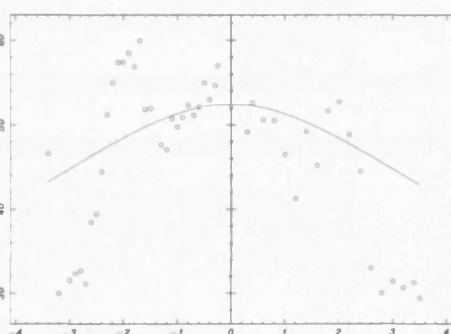
(b) (0.875 1.5) rod - Experimental data and Jones's model
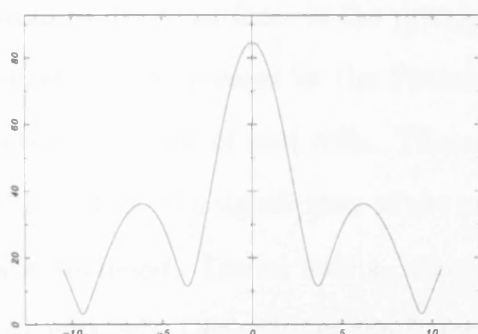
(c) Jones's prediction for (1.25 1) rod shown over a longer range in l than in (a)
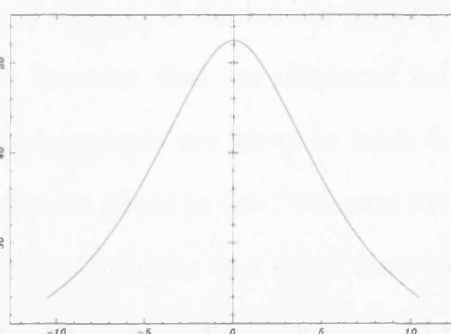
(d) Jones's prediction for (0.875 1.5) rod shown over a longer range in l than in (b)

Figure 8.17: Fractional rods: Comparison of measured rods with those predicted by Jones

model calculations, but care must be taken to ensure that the same reflections are used in both calculations. The Patterson function is discussed in more detail in section 3.4.1.

The differences caused by sampling are shown in figure 8.18. This compares the full data set of the cooled sample with one using only the data points of Jones *et al.*, and also the model predictions of Jones using both these sets of data points. The principal interatomic vectors are unchanged in these Patterson functions, so we have sampled sufficient reciprocal space for series truncation errors not to present a major problem.

8.8.5 Interpretation of Patterson maps

One of the common features of previous models [4, 15, 62, 63] of reconstructions on III-V surfaces is the presence of dimers. If dimers are present, then peaks will be present in the Patterson function that are displaced from an integer number of unit cells. These displacements are given in table 8.4. In this section, the significance of the prominent peaks in the Patterson function are discussed. The a_1 and a_2 direction are the long and short directions in the unit cell. Distances in the Patterson are given in multiples of a substrate unit cell (ie $|a_1|$).

The coordinates of the labels on the Patterson plots are given in table 8.5. In this table, O is the origin, and O' is a translation of this peak by $4a_1 + a_2$, and is equivalent to the centred symmetry of the reconstructed unit cell.

A and A' are equivalent and correspond to a displacement of 1 unit cell
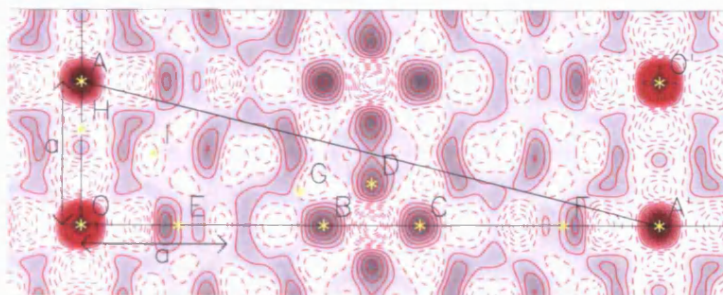
(a) Cold full data set
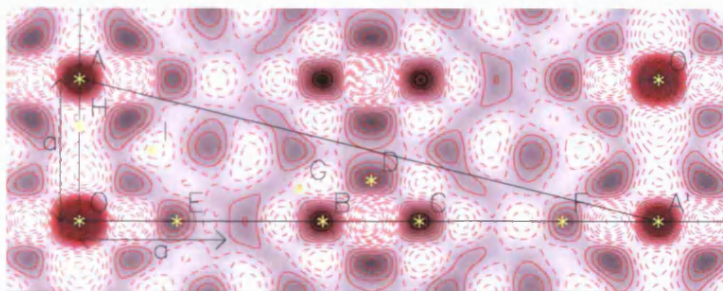
(b) Cold (Jones's data points)
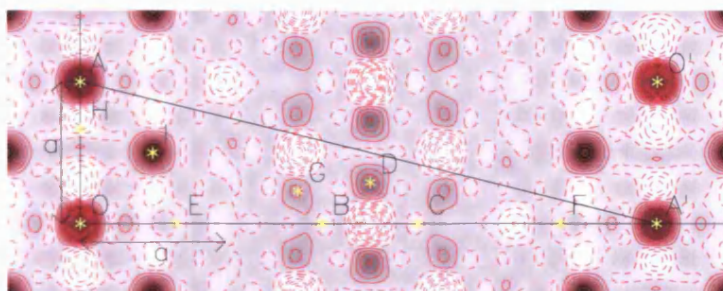
(c) Theoretical - Jones Model (Cold datapoints)
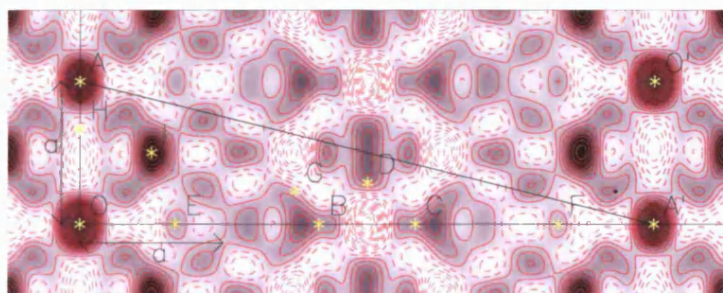
(d) Theoretical - Jones Model (Jones *et al.* data points)

Figure 8.18: Effect of sampling on Patterson

Atom	Atomic diameter [135],[143]		Maximum displacement	
	Å	Fraction of unit cell	of atom	of peak in Patterson
In	3.24Å	$0.709|a_1|$	0.145Å	<0.291
Sb	2.87Å	$0.633|a_1|$	0.183Å	<0.367

Table 8.4: Interatomic distances in indium and antimony dimers, and the corresponding displacement of peaks in the Patterson function caused by dimerisation.

Label	Position (unit cells)		Position (Å)	
	$x/|a_1|$	$y/|a_2|$	x(Å)	y(Å)
O	0	0	0	0
O'	4	1	18.32	4.58
A	0	1	0	4.58
A'	4	0	18.32	0
B	$1\frac{2}{3}$	0	7.64	0
C	$2\frac{1}{3}$	0	10.69	0
D	2	0.29	9.16	1.33
E	$\frac{2}{3}$	0	3.05	0
F	$3\frac{1}{3}$	0	15.27	0
G	1.5	0.23	6.87	1.05
H	0	$\frac{2}{3}$	0	3.05
I	$\frac{1}{2}$	$\frac{1}{2}$	2.29	2.29

Table 8.5: Position of peaks labelled in Patterson function in figure 8.16. O is the origin, and O' is also the origin transformed by $\frac{1}{2}\frac{1}{2}$ cell. Coordinates are given in terms of the unreconstructed surface unit cell $|a_1|$, and in Å. A-F are present in the experimental Patterson, G-I are present in some models, but not experimentally.

in a_2. Peaks E and F correspond approximately to the indium-indium dimer separation. Peaks B and C are also related to the indium-indium dimer separation and are discussed in more detail later. The other major feature is at D. In the model of Jones *et al.*, this interatomic vector is between antimony dimerised in the a_2 direction, and indium in non bulk positions (eg atoms labelled 2e and 2a in figure 8.4). The peak is also consistent with indium dimerised in the a_2 direction separated by 2 unit cells in a_1.

The model of Jones *et al.* [62] reproduces the peak at D. The peak at B is however displaced towards G, and C is likewise displaced. There is also a pronounced peak at I which is not present in the experimental data. Thus although there is general agreement, there are significant differences.

8.8.6 Possible models

The differences in Patterson function between the model of Jones *et al.* and the data, along with the difference in fractional rods means that it is necessary to find a better model. A comparison with other models (figure 8.19) leads to the Patterson functions given in figures 8.21. Clearly the model of John *et al.* [60] does not reproduce the experimental Patterson in figure 8.16. As found by Jones, the model of Skala *et al.* [107] is more promising, but this does not reproduce all the features either, in particular the peaks labelled B,C. The features at B,C,E,F are not reproduced well by the models of Jones *et al.*, or Skala *et al.*, so the analysis began with a study of those.

The models given in figure 8.23 reproduce the peaks at B and C in the Patterson, and are identical, except for their placement relative to the sym-
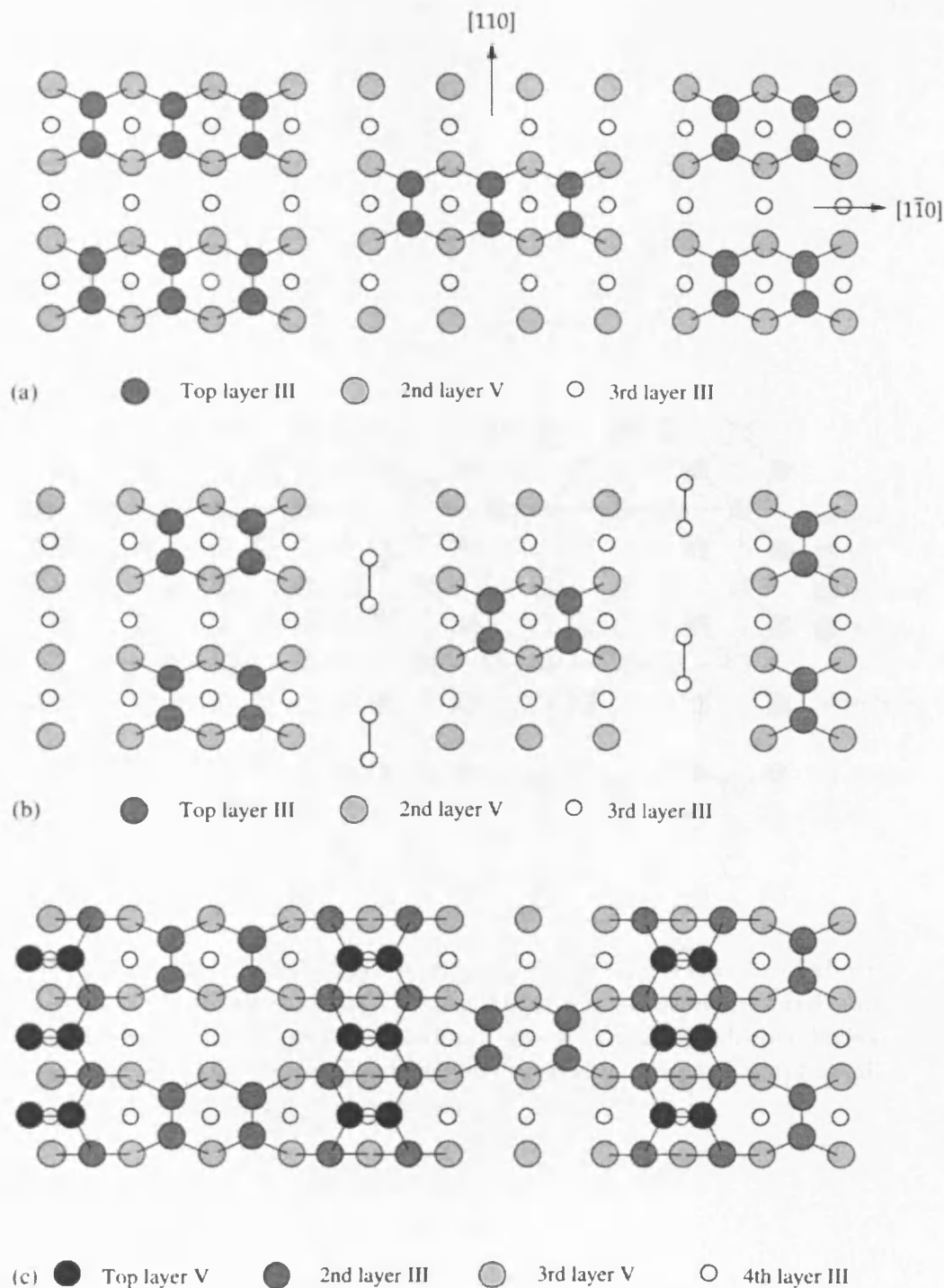
Figure 8.19: Structural models proposed for the $c(8\times2)$ reconstruction of the (001) surface of III–V semiconductors, (a) missing dimer model of John *et al.* for InSb(001) [60], (b) the model of Biegelsen *et al.* for GaAs(001) [8], and (c) the model of Skala *et al.* [107] for GaAs(001). Figure reproduced from Jones *et al.* with permission of the authors.
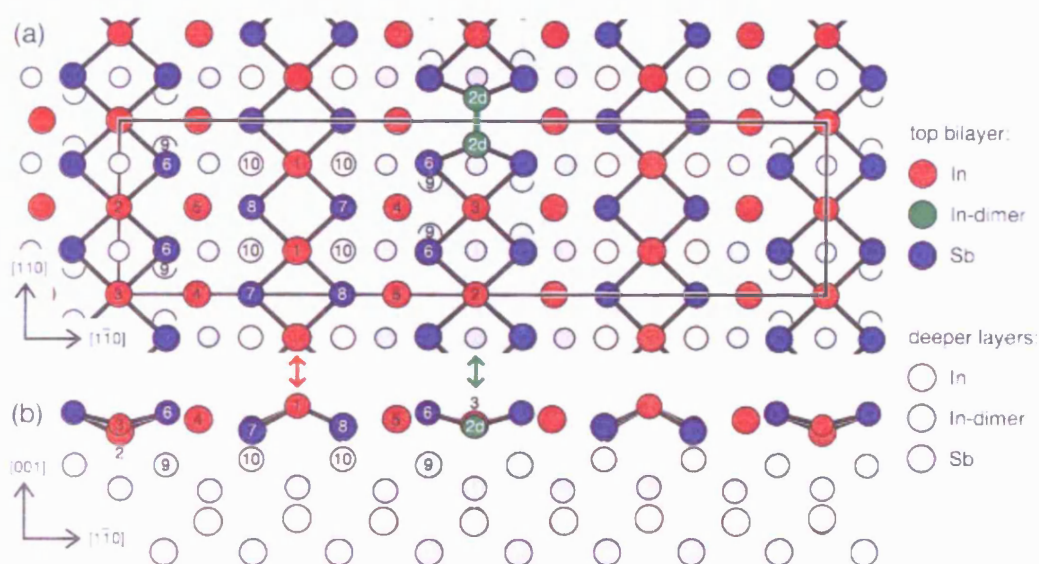
Figure 8.20: The model of Kumpf *et al.* [70, 71]. Views from above (a) and from the side (b). In and Sb atoms are shown as red and blue circles. In dimers are coloured green. Atoms in deeper layers are indicated by pale colours. Figure reproduced from Kumpf *et al.* [71] with permission of the authors.
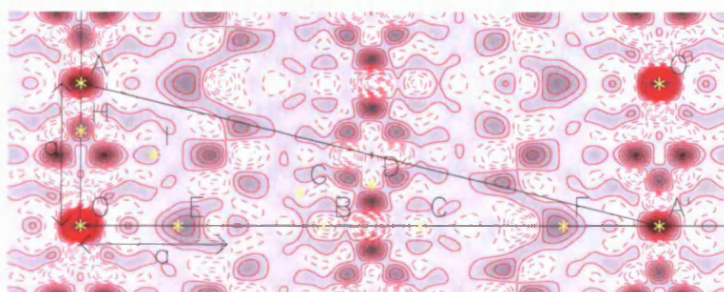
(a) Skala *et al.* [107]
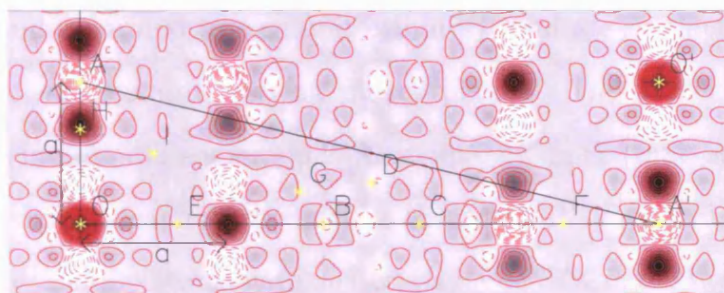
(b) John *et al.* [60]
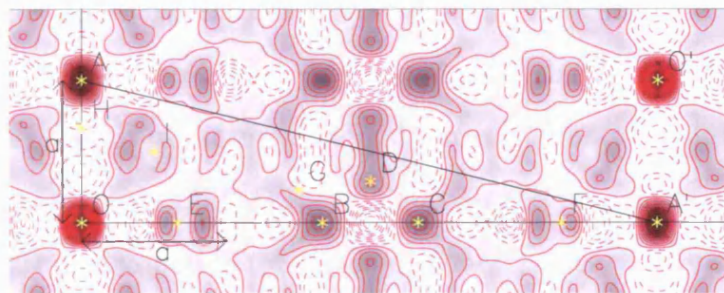
(c) Kumpf *et al.* [71]

Figure 8.21: Patterson functions for other models

metry elements of the unit cell. To reproduce the peaks at E and F requires a different model, and figure 8.24 represents one such model. In this model, the dimer separation is $\frac{2}{3}$ unit cell which corresponds to 3.05Å. This is shorter than the nearest neighbour distance in bulk indium of 3.24Å, though longer than the nearest neighbour distance of 2.87Å of antimony.

Subsequent to much of the analysis, a model was proposed by Kumpf *et al.* [70, 71] (figure 8.20) for the $c(8×2)$ reconstruction of InSb, InAs and GaAs surfaces. A novel feature of this model is that the main building blocks are subsurface indium dimers in the second bilayer rather than dimers on the surface as in many previous models. These indium atoms are dimerised along $\mathbf{a_2}$ and separated by one unit cell in $\mathbf{a_1}$, and are symmetry equivalent due to the adjacent intersecting mirror planes. The model also features disordered indium dimers with a 28% occupancy on the InSb surface though different occupancies are proposed for the other III-V surfaces. The model also features indium atoms with an occupancy of 57% in the twofold rotation sites also with a degree of disorder. The model consists of eleven symmetry inequivalent atoms, significantly more than the three in the model of Jones; in addition both models have small relaxations of the layer below. This model provides the best fit to the experimental Patterson function (figure 8.21), and reproduces features at B,C,D,E,F. The fit to the in-plane structure factors (figure 8.22) is also better than that of Jones *et al.* (figure 8.13), and has $\chi^2 = 5.2$, compared with $\chi^2 = 9.2$ for the model of Jones *et al.*.

The model of Kumpf *et al.* (figure 8.20) contains some of the features from our analysis. In particular, atoms 4 and 5 in the Kumpf model are contained in the model in figure 8.24a, though shifted by half a unit cell
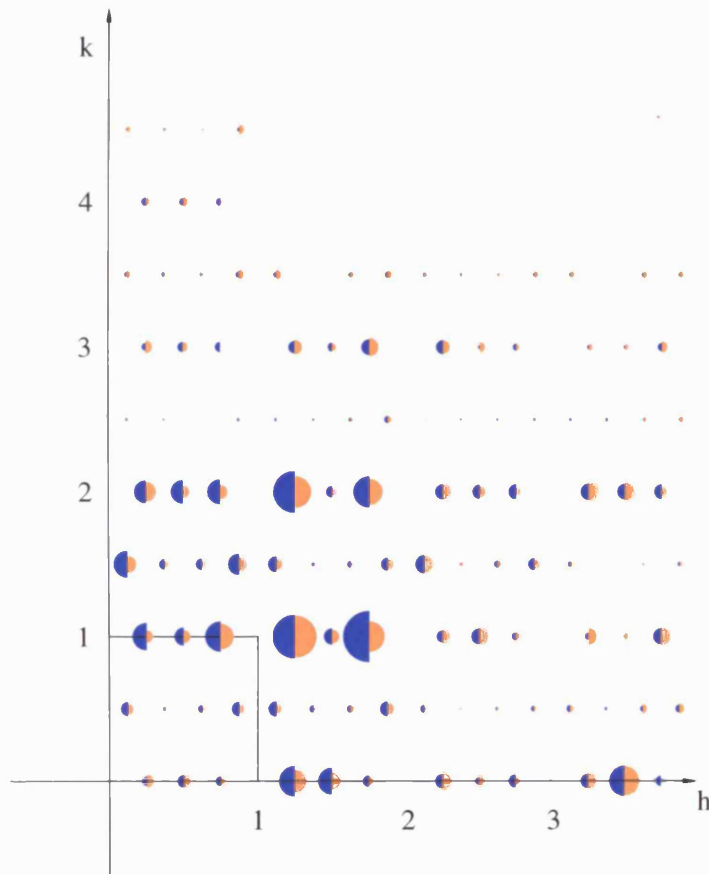
Figure 8.22: Comparison between experimentally measured structure factors and those predicted by the model of Kumpf *et al.* [70, 71]. Data measured at 74K is shown in the blue lefthand semicircles, and the model predictions in the orange righthand semicircles. This model reproduces the data better than that of Jones *et al.* (figure 8.13), and the χ^2 value of the fit is better, $\chi^2 = 5.2$ compared to $chi^2 = 9.2$ for the model of Jones *et al.*.

in y. The interatomic vector between atoms 1 and 2d and also between 9 and 10 is the same as suggested to reproduce the feature labelled D in the experimental Patterson function.

8.9 Discussion

Although initially the aim of the experiment was to measure structural changes that occurred on cooling the InSb(001)-c(8×2) reconstruction, it became apparent that the model of Jones *et al.* did not completely fit the data either at room temperature or at low temperature, so this discrepancy was investigated further. Subsequent to this investigation, a model was published by Kumpf *et al.* that provides a better fit to our data and contains features identified in this work.

X-ray diffraction does not allow us to differentiate between indium and antimony atoms since their atomic numbers are close (49 and 51). Assignment of atoms to specific sites must therefore be based on consideration of physical and chemical factors. In particular, the interatomic distances are limited by the atomic radii. Dimers are a common feature on III-V surfaces [63], and the distance between the atoms in the dimer is unlikely to be less than the nearest neighbour distance in the bulk element; this is 3.24Å for indium and 2.87Å for antimony which correspond to 0.71 and 0.63 substrate unit cells respectively. The second consideration is that the energy penalty of bending an interatomic bond is lower than that for stretching a bond [1, 74], thus reconstructions involving bond bending are more likely than those involving bond stretching. The InSb(001) surface only has twofold symmetry,
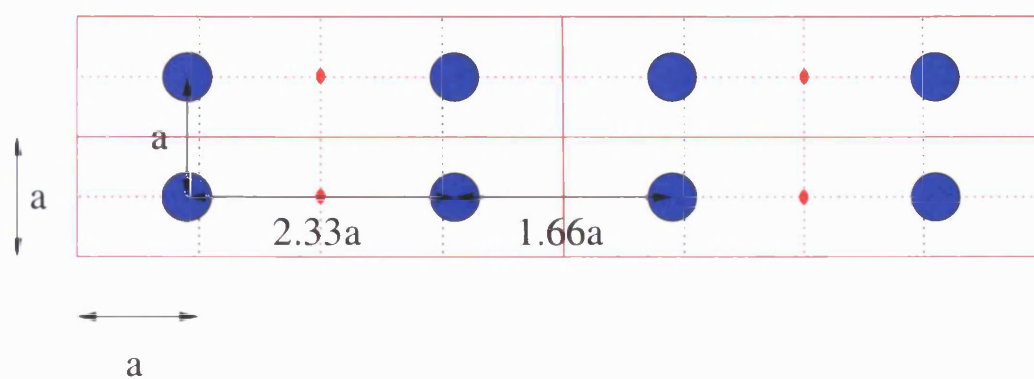
(a) Model
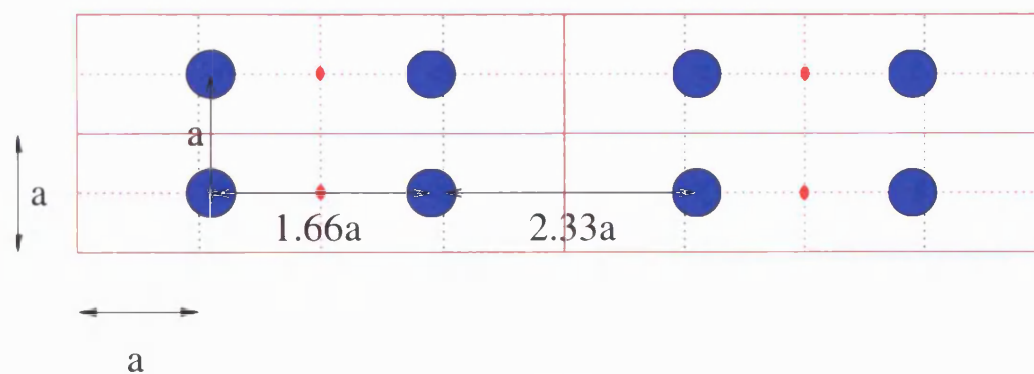
(b) Model
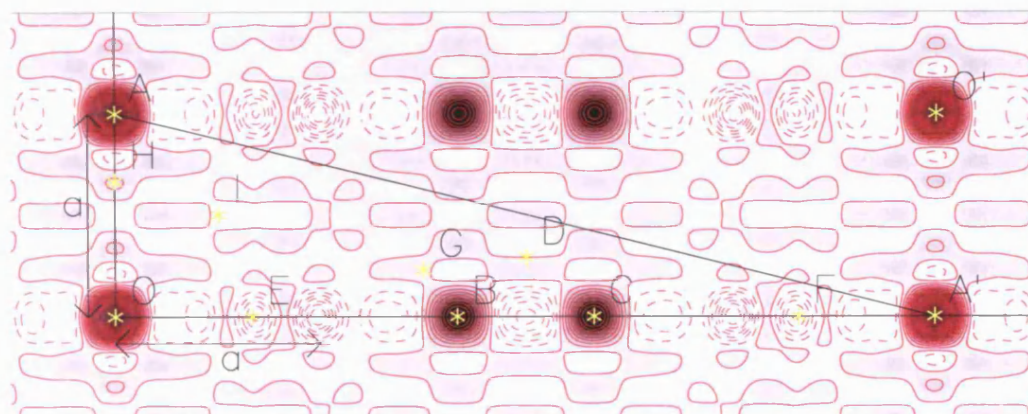
(c) Patterson function

Figure 8.23: A dimer model (a) and (b) that reproduces the peaks at B and C in the Patterson (c). The same model is shown in (a) and (b) but in different positions relative to the symmetry elements of the unit cell.
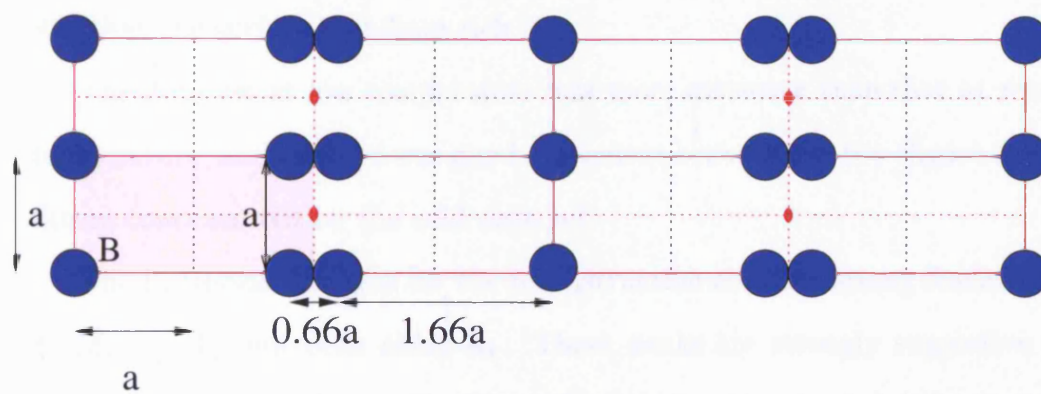
(a) Model
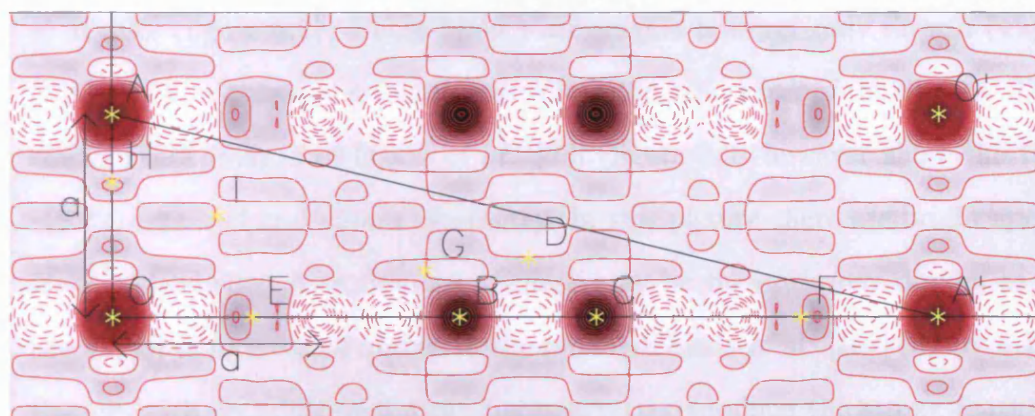
(b) Patterson function

Figure 8.24: Model that fits peaks A,B,C,E,F

the a_1 and a_2 directions of indium antimonide are not equivalent. In the $c(8\times2)$ structure, indium moves along the a_2 direction by bending bonds, and antimony along the a_1 direction. Thus any dimerisation along the a_1 direction is likely to be due to motion of antimony atoms. Finally, it is also clear from the phase diagram (figure 8.1 [80]) and photoemission experiments [60] that the surface is indium rich.

The data set at low temperature was more extensive than that at room temperature, and as there was good agreement between the two (figure 8.12), fitting concentrated on the cold data set.

The Patterson function for the reconstruction contains strong features at $\frac{2}{3}$, $1\frac{2}{3}$, $2\frac{1}{3}$, $3\frac{1}{3}$ unit cells along a_1. These peaks are strongly suggestive of dimerisation along the a_1 direction. One explanation is that it is rows of these dimers that are visible in the filled state STM images of McConville et al. [80] (figure 8.2). These filled state images however only show a (4×1) unit cell, so it is not possible to determine the x position of the dimers. The empty state images of Davis et al. [23] (figure 8.3) however show the full $c(8\times2)$ unit cell and $c2mm$ symmetry. In this picture there are bright spots along a_2, labelled A in figure 8.3; these may be the antimony dimers as in the model of figure 8.24 and as in the model of Skala et al. [107] (figure 8.19) though with an additional atom necessary to reproduce the strong features B and C in the Patterson. There are however a number of structures that would contribute to these peaks in the Patterson function. The peak at D in the Patterson must be due to some dimerisation along a_2. The model of Jones et al. attributes this to antimony dimers, however the fractional order rods (figure 8.17) are strong evidence that the reconstruction is deeper than

that proposed by Jones *et al.*.

In the model recently proposed by Kumpf *et al.* [70, 71], buried indium dimers near the origin of the unit cell are proposed. These buried indium dimers provide an explanation for the difficulty in observing the full $c(8\times2)$ unit cell in STM measurements, a contrast to LEED and SXRD measurements where the $c(8\times2)$ character is clear. The model is significantly more complex than that of Jones, containing eleven symmetry inequivalent atoms compared to the three in Jones's model with both models having small relaxation of the layers below. The model is deeper than that of Jones, and more than one layer contributes to the eighth order peaks, providing an explanation for the structure in the fractional rods. It is however not yet clear how to explain the empty state STM image of Davis *et al.* (figure 8.3) in terms of this model. In this image, there are bright spots at $(\frac{1}{4}\frac{1}{2})$, in other words on the mirror line adjacent to the twofold axis, and it might be expected that these would correspond to indium atoms. In the Kumpf model, the indium atoms are on the twofold axis at $(\frac{1}{4}\frac{1}{4})$, and not on the mirror line; simulated STM images may be able to resolve this ambiguity. A further cause for doubt with this model is the partial occupancy and high Debye-Waller factors of some of the surface sites (200Å^2 in one case). This model does reproduce the features in the experimental Patterson function, and structure in the fractional rods significantly better than any of the other models considered. It is clear therefore that this is the best model so far of the InSb(001)-$c(8\times2)$ reconstruction.

The data at room temperature and at 74K are consistent with reduced thermal vibration at lower temperatures reducing the Debye-Waller param-

eter. Structural changes occur on cooling other semiconductor systems such as Ge(001) [36, 65] or indium on silicon (111) [69]. The indium chains proposed in the model of Jones *et al.* [62] are unstable and would be expected to undergo a Peierls distortion as occurs with another 1-D system, thallium on copper (001) [9]. There was however no evidence for a structural change on cooling the InSb(001)-$c(8\times2)$ reconstruction, and there are a number of possible explanations for this.

A reduction in symmetry caused by cooling might produce additional reflections, but these were not observed by LEED (figure 8.8) or SXRD. The diffuse half order peak in figure 8.11 may indicate some dimerisation along the chains, as would occur in a Peierls distortion. It is however present at room temperature, so this explanation is unlikely, and it seems more probable that the antimony capping layer had not been completely removed, and small domains of the antimony rich $c(4\times4)$ reconstruction remained, or that it is due to disorder in the $c(8\times2)$ reconstruction.

It is not possible to completely rule out a small change on cooling; there is however no evidence for any structural change, and the absence of additional features in the Patterson function at low temperature tends to suggest that there has been no structural change. The relatively poor fit to the data ($\chi^2 = 9.2$) of the model of Jones *et al.* and significantly better fit ($\chi^2 = 5.2$) of the model of Kumpf *et al.* [70, 71] calls into question the presence of the indium chains proposed in that model. If these chains are not present, they cannot undergo a Peierls distortion. It would therefore be desirable to obtain direct evidence for a Peierls distortion, perhaps by the use of photoelectron spectroscopy. It is also possible that a Peierls distortion would be visible if

the experiment were performed at lower temperatures by the use of liquid helium cooling.

8.10   Conclusions

X-ray diffraction experiments have been performed on the $c(8\times2)$ reconstruction of the InSb(001) surface. The aim of the experiment was to determine structural changes on cooling, but no such changes were observed. It became apparent, however, that there were deficiencies in the model of Jones et al. [62]. The model of Kumpf et al. is found to be a significantly better fit to the data. It has not proved possible to find a model that is consistent with all the data, but it is clear that the model of Kumpf et al. is the best model so far. The following conclusions have been reached:

- While the model of Jones et al. fits some features present in the reconstruction, the model of Kumpf et al. is clearly better with $\chi^2 = 5.2$ when compared to $\chi^2 = 9.2$ for the model of Jones. In addition, the model of Kumpf et al. better reproduces the experimental Patterson function.

- Neither SXRD nor LEED show any evidence for a structural change on cooling to 74K, apart from the change in Debye-Waller parameter expected with the reduced thermal vibration.

- There is evidence for dimers along the long axis of the reconstruction. This is consistent with the STM pictures of McConville et al. [80].

- The fractional rods indicate that the reconstruction is deeper than proposed by Jones *et al.* [62] and the model of Kumpf *et al.* [70, 71] provides an explanation for this.

Chapter 9

Conclusions and Further work

9.1 Introduction

The main experimental conclusions, which are presented in the previous three chapters, are summarised here. The reader is, however, referred to these chapters for a more comprehensive description of each experiment. Suggestions for improvements to the technique of surface diffraction and data analysis are made. In addition, possible areas of future research that build on the current work are identified, along with their scientific, environmental or industrial motivation.

The intense X-ray beams produced by synchrotron sources have enabled X-ray diffraction to become an important tool for studying surfaces in UHV [34]. The technique is most effective for the study of heavier elements because the signal increases as the square of the atomic number. The brilliance of third generation synchrotron sources such as the European Synchrotron Radiation Facility (ESRF) in Grenoble has allowed this and other recent

179

studies [103] to extend this technique to the study of light elements such as carbon and oxygen. UHV conditions have been necessary in order to obtain an atomically clean surface free from contaminants. The environmental chamber described in chapter 4 allows samples to be prepared under UHV conditions and subsequently measured in a gas at pressures above atmospheric pressure [98, 116]. These two factors have enabled surface diffraction to bridge the "pressure gap".

9.2 Ni(110)-(2×1)-2CO

The structure of the Ni(110)-(2×1)-2CO reconstruction has been measured at a pressure of 2.3 bar. The structure at this high pressure was the same as that measured at 1×10^{-5} mbar. The atomic positions have been determined to within 0.02 Å, and are consistent with, though more accurate than, the results of previous studies [50, 76, 91, 103, 115, 147]. This is an example where the behaviour at high pressure is unchanged from previous UHV studies.

Heating the Ni(110)-(2×1)-2CO reconstruction however produced a dramatic difference between the results at low and high pressure. At 1×10^{-5}mbar, heating to 50°C destroyed the reconstruction by desorption of the carbon monoxide from the surface. At 2.3 bar however heating caused a dramatic change in morphology of the surface resulting in the formation of {111} facets with a base size of ≈100Å. The surface of these facets was found to be disrupted from the perfect {111} face, consistent with a larger lattice parameter, perhaps caused by dissolution of carbon.

This system shows both the importance of high pressure experiments to

bridge the pressure gap, but also the relevance of the low pressure experiments that have been performed to date.

9.3 InSb(001)-$c(8 \times 2)$

SXRD and LEED were used to measure the effect of cooling the InSb(001)-$c(8 \times 2)$ reconstruction. No structural changes of the reconstruction were observed with LEED on cooling to 86K, or SXRD on cooling to 74K. The model of Jones et al. [62] does not fit the fractional order rods, and there are features present in the Patterson function generated from the in-plane data that are not in the model of Jones, and vice versa. This casts doubt on the model of Jones. It has not proved possible to find a model that fits all the available data, however the recently published model of Kumpf et al. [70, 71] contains some key features identified in this study, and provides the best fit so far.

9.4 Improvements to Techniques

9.4.1 The Critical Angle

If the X-ray beam were incident on the sample surface at the critical angle there would be significant advantages in terms of signal/noise ratio in the diffraction peaks. At the critical angle, the electric field strength at the surface, and hence the diffracted intensity due to the reconstruction is increased. The background from thermal scattering in the bulk is also reduced as the X-rays do not penetrate so far into the crystal. The major disadvantage of this

approach is the significant systematic errors in measured intensities caused by a small misalignment of the crystal. Improvements in sample alignment, perhaps by making use of the reflected beam, to avoid this systematic error would offer significant improvements in the signal/noise ratio.

9.4.2 Data Analysis - Improvements to Current Techniques

There are a number of possible improvements that could be made to ROD (the program used in this thesis to fit a model to the measured structure factors) both in terms of ease of use, and of functionality. Currently it is not possible to constrain a relationship between fitting parameters. For example it is not currently easy to relax the whole surface layer at once away from the bulk. Another aspect of this is when fitting adsorbate molecules. It would be useful to constrain bond lengths and angles individually and allow the whole molecule to rotate. For example in the work reported here it would have been useful initially to constrain the length of the C–O bond and then to fit this later in the analysis. For more complex adsorbates this will become more important. A recent version of ROD [128] allows an adsorbate to be treated as a single unit, and the position and rotational coordinates optimised, but it is not easy to then optimise the atomic positions within the molecule while constraining the structure to one that is chemically reasonable. Another deficiency is the handling of symmetry equivalent atoms. Currently it is possible to construct such a model by hand, however it would be useful if it were possible to automate this in ROD.

It would be useful to enhance the interaction between ROD and molecular visualisation programs such as rasmol [104]. One such use would be to orient a molecule on a surface, perhaps placing certain parts of the adsorbate in particular surface sites. Graphical selection of atoms to move or constrain when fitting would also be useful. A long term aim should be to use the molecular mechanics capabilities of some molecular modelling packages to provide some initial constraints when fitting the data. It would also be advantageous to remove the restriction that ROD and rasmol must share a filesystem. This would facilitate calculations in ROD being performed on a powerful central computer, while permitting the visualisation of the structure on the local computer.

9.4.3 Data Analysis - Future Techniques

The analysis methods currently used rely on the construction and refinement of models. Although use of the Patterson function makes some contribution to the solution of the structure, the use of methods that can systematically solve the structure would be an advance.

Direct methods represent a very exciting possibility for the solution of surface structures. Potentially they can solve surface structures in a systematic manner, without the preconceptions of the experimenter. Possible improvements include enhancements to direct methods techniques to take advantage of the out of plane information available in the fractional order rods, and the known phase information in the crystal truncation rods. These improvements might have permitted solution of the $InSb(001)$-$c(8\times2)$ reconstruction.

Another approach is Reverse Monte Carlo (RMC) modelling [47, 82]. In this method, random modifications are made to a model to generate the best fit. If sufficient unit cells are included, it may also be possible to fit the peak shape and background.

Genetic algorithms [44] can be used as a general optimisation technique, and have been applied to many problems, including the solution of surface structures by LEED [28]. In this approach, models are bred together, and ultimately the best fit structure survives. Application of this to SXRD would again potentially give a systematic way of searching through possible models.

Current methods of fitting a structure involve a two stage process: first structure factors are calculated and then these structure factors are fitted to the data. It would be advantageous to eliminate this intermediate stage, as the errors in the raw data are better understood than the errors in a parameter derived from this data. This could perhaps be accomplished by RMC methods, or by extension of ROD to predict peak width and shape, along with fitting slight diffractometer misalignment.

9.5 Future III-V experiments

To resolve the structure of $InSb(001)\text{-}c(8\times2)$, more work is necessary. Of particular interest would be STM studies carried out on the same sample as studied by other techniques. This would allow direct comparison of the structures, and avoid any questions of a difference in surface preparation. Cooling down to lower temperatures with liquid helium may induce structural changes not observed at liquid nitrogen temperatures.

Studies of the heteroepitaxial growth and the growth of ternary alloys on III-V surfaces is important for the production of semiconductors with tailored band gaps. One potential use is in the manufacture of infra-red lasers. Another use is in gas sensors that measure infra-red absorption spectra. These have applications in monitoring of pollution from vehicle exhausts.

Quantum dots are of fundamental scientific interest as they represent a zero dimensional system; they also have potential applications in optoelectronics and quantum computing. Quantum dots can be produced by heteroepitaxial growth on III–V semiconductors, for example InAs on a GaAs substrate [94]. An understanding of the bulk structure and interface structure is necessary to facilitate calculations of their electronic properties. X-ray diffraction can provide information on the structure *in situ* without the necessity to cleave the crystal as is the case with some STM studies [30].

9.6 Future high pressure experiments

In this section, materials and systems for future research, and their motivation, will be identified. In particular for the high pressure gas–surface systems, there is a huge range of systems of technological interest. Suggestions include the study of different surface planes, different catalyst crystals, different gases, and ultimately the study of a reaction as it is taking place. A study of the surface structure of model catalyst crystals in realistic environments will lead to an improved understanding of the mechanisms behind catalysis. This improved understanding will facilitate the production of more efficient catalysts that are more durable and resistant to poisons than current

catalysts. This improved efficiency will have consequent environmental and commercial benefits.

9.6.1 Choice of Gas

The major pollutants from vehicle exhausts include carbon monoxide, a poisonous gas, unburned hydrocarbons, which contribute to the formation of smog, and have an unpleasant smell and oxides of nitrogen which contribute to acid rain, low level ozone and smog; they also exacerbate respiratory problems [79].

The catalytic removal of oxides of nitrogen is therefore of major importance [93]. Taking nitrogen oxide (NO) as an example, it is a particular challenge because even though the molecule is thermodynamically unstable at 298K and 1 bar the high energy of dissociation (153.3 kcal mol^{-1}) results in extremely low decomposition rates. Current catalysts therefore rely on the presence of unburned hydrocarbons and carbon monoxide to act as reducing agents and react with the NO. The removal of carbon monoxide and hydrocarbons by contrast is relatively simple as they react over a catalyst in the presence of excess air to form carbon dioxide and water.

$$2NO \rightarrow N_2 + O_2 \qquad (9.1)$$

The efficient removal of NOx from vehicle exhausts under lean burn conditions (excess air) is a topic of current research [79]. Some current lean-burn catalysts work by NOx storage [39], that is NOx is stored on the catalyst under lean conditions, and burned off when the mixture becomes richer (ie

excess fuel). The mixture becomes richer during, for example, acceleration; however in long periods at a steady cruising speed, in order to meet NO_x emission limits, it is currently necessary for a car with a lean burn engine to periodically retard the ignition timing (and hence run less efficiently and produce more CO_2) to enable the catalyst to "burn off" the stored NOx.

9.6.2 Choice of catalyst surface

For the experiments described in this thesis, nickel was chosen as being of catalytic importance, and also facilitating the experiments. Many other catalyst systems exist, see for example table 2.1. A particular surface of interest for the study of NOx would be rhodium as it plays the most important role in NOx reduction in an autocatalyst [133].

Rhodium single crystals show a surprisingly wide range of reconstructions induced by light elements such as oxygen and nitrogen [18]. Oxygen-induced $(1 \times n)$ missing/added row structures and nitrogen induced $(n \times 1)$ structures are discussed in the review paper by Comelli *et al.* [18]. In particular oxygen on Rh(110) forms a $(2 \times 1)p2mg$ structure, but when the temperature is high enough to permit Rh diffusion (500-600K) a whole new set of LEED patterns is observed including two $(2 \times 3)p2mg$, a $(2 \times 2)p2mg$ and $c(2 \times 2n)$ superstructures with n=3,4,5. When oxygen is removed from $(2 \times 2)p2mg$ and $c(2 \times 2n)$ surfaces by hydrogen titration at low temperatures a (1×2) and $(1 \times n)$ reconstruction respectively remain due to a reconstruction of the underlying rhodium.

At low temperatures, NO adsorbs molecularly on rhodium, but dissociates

upon heating [106], though at high coverages some NO desorbs molecularly. If NO dissociates on Rh(110), the surface can be dominated by nitrogen induced ($n \times 1$) or oxygen induced ($1 \times n$) reconstructions [75].

Comelli et al. [18] note that a general trend is the higher dissociation propensity of NO on more open and stepped Rh surfaces. The (110) surface is more open and table 9.1 shows that this surface has a lower activation energy for this reaction than the (111) or (100) surfaces. Thus the (110) surface is more active for the elimination of NOx than the other low index surfaces.

Surface	E(kJ/mol)
Rh(111)	40±6
Rh(100)	44±3
Rh(110)	20±2

Table 9.1: Experimentally determined parameters for NO dissociation on rhodium planes.[18]

There is also the possibility of choosing a miscut surface which will have surface steps. Hammer's theoretical calculations on NO dissociation on Ru(0001) suggest that monatomic steps in the ruthenium surface offer completely new reaction pathways with highly reduced energy barriers compared to reaction at a flat surface [49]. Hammer cites an STM study by Zambelli et al. that revealed that at room temperature, the atomic steps are the only active sites for NO bond activation at surfaces vicinal to Ru(0001).

9.6.3 Chiral surfaces

The nature of the crystal surface can determine the predominant reaction product. The study of structures formed by chiral molecules on a surface is of both fundamental and commercial interest, as the formation of a chiral surface could perhaps be used to influence the chirality of reaction products [77]. This is important because different optical isomers of a molecule can have different biological properties. For example the R and S isomers of Limonene, have different taste — orange or lemon [89]. This is of particular importance in the manufacture of pharmaceuticals, as was tragically found in the case of thalidomide where one optical isomer was active, and the other isomer, present as a byproduct of the manufacturing procedure, produced birth deformities [118].

During this thesis, an experiment was attempted on one such system, alanine on copper (110). Unfortunately it was not successful due to difficulties with sample preparation and also the data collection system. Chiral surfaces are however of much potential interest and worthy of further study.

9.6.4 Determination of impurities

As indicated previously, because of the limitations of the experimental apparatus, it is not currently possible to measure the degree of surface contamination, and without this, it is difficult to determine whether there are significant impurities building up on the surface. Auger electron spectroscopy (AES) is often used to measure surface contamination, but the equipment is relatively bulky to be fitted to the small chamber used for these experiments.

In addition, AES will not work in the presence of high pressure gas. As an alternative, Norris [88] suggests that it might be possible to use grazing incidence fluorescence to measure surface contamination. This could work at high gas pressures, though there will be limitations on the elements that can be detected. If it is possible to modify the apparatus to do this, then it could be important in the determination of catalyst poisons.

9.7 Summary

Surface X-ray diffraction is a well established technique for the study of surfaces and interfaces. The technique has been used in a range of environments, including low temperature and high gas pressure. In particular, the experiments described in this thesis, and elsewhere [98, 116], have demonstrated that SXRD can be used to bridge the "pressure gap" and provide structural information on the gas–solid interface at high gas pressures. A number of possible avenues of future research have been identified in systems of scientific, technological and environmental importance.

Appendix A

Glossary

(hkl)	Crystal face or reciprocal lattice point.
$\{hkl\}$	Crystal faces related by symmetry to (hkl)
1 bar	A pressure of 10^5 Pa. This is approximately equal to atmospheric pressure (a standard atmosphere is 101325 Pa = 1013.25 hPa = 1013.25 mb, though the pressure at sea level varies with the weather and pressures between 960 mb and 1030 mb are not unusual)
isostere	A contour on a $p(T)$ plot at constant coverage (see for example Venables [122])
AES	Auger electron spectroscopy
AFM	Atomic force microscopy
ANA	Program to generate structure factors from raw data by integrating and applying geometrical and resolution correction factors (section 5.1.2).
BSD	Berkeley Software Distribution, a "flavour" of UNIX

CO	Carbon monoxide
CTR	Crystal Truncation Rod
DIF	Program for diffractometer alignment (section 5.1.1)
ESRF	European Synchrotron Radiation Facility [32]
EELS	Electron energy loss spectroscopy
LEED	Low energy electron diffraction
rasmol	Molecular graphics program [104], see also rasmol extensions to ROD in section 5.2.2.
RHEED	Reflection high energy electron diffraction
ROD	Program to fit a structural model to experimental structure factors (section 5.1.4).
SXRD	Surface X-Ray Diffraction
STM	Scanning tunnelling microscope
SEM	Scanning electron microscopy
SFG	infrared-visible Sum Frequency Generation
FIM	Field Ion Microscopy
FWHM	Full Width Half Maximum
hutch	Radiation shielded room containing the experimental apparatus.
Insertion Device	Undulator or wiggler in straight section of synchrotron ring producing intense radiation.
NO	Nitric Oxide
NOx	Oxides of Nitrogen such as NO, NO_2, N_2O, N_2O_4
RGA	Residual gas analyser

RMC	Reverse Monte Carlo
SPEC	The diffractometer control software [108].
TDS	Thermal desorption spectroscopy
UHV	Ultra High Vacuum
XPS	X-ray photoelectron spectroscopy
Undulator	Periodic array of magnets in straight section of synchrotron ring - produces very intense radiation.
X-ray Flux	photons s^{-1}
X-ray Brightness	$\dfrac{\text{photons s}^{-1}}{\text{(unit solid angle)(0.1\% Bandwidth)}}$
X-ray Brilliance	$\dfrac{\text{photons s}^{-1}}{\text{(unit solid angle)(0.1\% Bandwidth)(source size)}}$

Appendix B

The convolution theorem

For two functions $a(x)$ and $b(x)$ with Fourier transforms $A(q)$ and $B(q)$ respectively the convolution is defined as

$$a(x) * b(x) = \int_{-\infty}^{\infty} a(x')b(x - x')dx' \tag{B.1}$$

where * is the convolution operator.

The convolution theorem states that the Fourier transform of a convolution of two functions is simply the product of the Fourier transforms of the two functions.

$$A(q) \times B(q) = \int_{-\infty}^{\infty} (a(x) * b(x))e^{iqx}dx \tag{B.2}$$

Appendix C

Formulae used by ANA for error calculations

Peak integration and structure factor calulations for raw data.

Raw data

The ith raw data point for the detector count, monitor count and angular motor position are given by:

$$counts'(i), monitor(i), \varphi(i); i = 1...N$$

Calculated error

The statistical error of a raw data point is then:

$$error'(i) = \sqrt{counts'(i)} \qquad (C.1)$$

Normalisation

The data is then scaled by the monitor to a reference monitor count, $MONITOR$, which can be set in ANA. $MONITOR$ is usually chosen to be the number of monitor counts per second at a convenient storage ring current and slit settings.

$$counts(i) = counts'(i) \times \frac{MONITOR}{monitor(i)} \qquad (C.2)$$

$$error(i) = error'(i) \times \frac{MONITOR}{monitor(i)} \qquad (C.3)$$

Background

The background count rate, bg, and error, Δbg, can be determined from either from a fit to the data, or from N_L and N_R background points on the left and right of the scan respectively. In this latter case, bg and Δbg are given by:

$$bg = \frac{1}{N_L} \sum_{i=1}^{N_L} counts(i) + \frac{1}{N_R} \sum_{i=N-N_r+1}^{N} \qquad (C.4)$$

$$\Delta bg = \frac{1}{N_L + N_R} \sqrt{\sum_{i}^{N_L N_R} (error(i))^2} \qquad (C.5)$$

Peak integration

The area under a diffraction peak, A_{peak}, is given by:

$$A_{peak} = \sum_{i}^{Peak} counts(i) \times \overbrace{(\varphi(i+1) - \varphi(i))}^{\text{step size}} \qquad (C.6)$$

$$\Delta A_{peak} \;=\; \overset{Peak}{\underset{i}{\sum}} error(i) \times \overbrace{(\varphi(i+1) - \varphi(i))}^{\text{step size}} \qquad (C.7)$$

$$stepsum \;=\; \overset{Peak}{\underset{i}{\sum}} \overbrace{\varphi(i+1) - \varphi(i)}^{\text{step size}} \qquad (C.8)$$

where *stepsum* is the angular width of the peak integration. The step size is not necessarily a constant, and is often chosen to be larger in the background.

Background Subtraction

The integrated intensity, I_{peak}, is then obtained by subtracting the background from the area under the peak, A_{peak}.

$$I_{peak} \;=\; \frac{1}{STEPSIZE} \times (A_{peak} - bg \times stepsum) \qquad (C.9)$$

$$\Delta I_{peak} \;=\; \frac{1}{STEPSIZE} \times \sqrt{(\Delta A_{peak})^2 + (\Delta bg \times stepsum)^2} \quad (C.10)$$

where $STEPSIZE$ is a reference step size.

Structure factor - F

The structure factor, F, can be obtained by applying the geometric and resolution correction factors, C_{all}, to the integrated itensity, I_{peak}, and taking the square root:

$$F \;=\; \sqrt{\frac{I_{peak}}{C_{all}}} \qquad (C.11)$$

$$\Delta F \;=\; \sqrt{F^2 + \left(\frac{\Delta I_{peak}}{C_{all}}\right)^2} - F \quad \text{(robust formula)} \qquad (C.12)$$

Appendix D

Formulae used by AVE

AVE calculates the weighted average of equivalent reflections using the following formulae.

Weighting Factors

For several symmetry equivalent structure factors, F_i, the weighting factor, w_i, of the ith reflection is given by:

$$w_i = \frac{1}{(\Delta F_i)^2} \qquad (D.1)$$

$$\text{with} \quad i = 1..E = \text{number of equivalent reflections}$$

Where ΔF_i is the error in the structure factor.

Average Structure Factors

The weighted average structure factor $\bar{F}$ is then given by:

$$\bar{F} = \frac{\sum\limits_{i=1}^{E} F_i w_i}{\sum\limits_{1=i}^{E} w_i} \qquad (D.2)$$

$$\bar{F^2} = \frac{\sum\limits_{i=1}^{E} (F_i w_i)^2}{\sum\limits_{1=i}^{E} (w_i)^2} \qquad (D.3)$$

Error of structure factors

The statistical error, σ_1 is:

$$\sigma_1 = \sqrt{\frac{E}{E-1}(\bar{F^2} - \bar{F}^2)} \qquad (D.4)$$

The systematic error is calculated using one of the following formulae depending on the value of *SIG2MODE*:

$$SIG2MODE = \ 0: \quad \sigma_2 \ = \ \sqrt{\frac{1}{\sum\limits_{i=1}^{E} w_i}} \qquad (D.5)$$

$$SIG2MODE = \ 1: \quad \sigma_2 \ = \ \frac{1}{E}\sum\limits_{i=1}^{E} \Delta F_i \qquad (D.6)$$

$$SIG2MODE = \ 2: \quad \sigma_2 \ = \ \sqrt{\frac{E}{\sum\limits_{i=1}^{E} w_i}} \qquad (D.7)$$

Agreement factor

$$\varepsilon_k = \frac{1}{E} \sum_{F_{i,k} > 2\sigma_{2,k}} \frac{\sigma_{1,k}}{F_{i,k}} \quad \text{k = index for non-equivalent reflections} \quad \text{(D.8)}$$

$$\bar{\varepsilon} = \frac{1}{M} \sum_{k=1}^{M} \varepsilon_k \quad M = \text{number of non-equivalent reflections} \quad \text{(D.9)}$$

Final error

The final error is then:

$$\sigma_k = \sqrt{\bar{\varepsilon}^2 \bar{F}_k^2 + \sigma_{2,k}^2} \quad \text{(D.10)}$$

Appendix E

Proof that a centered unit cell leads to systematically missing peaks

This is a proof that translational symmetry of (0.5,0.5) such as is found in the $c(8\times2)$ reconstruction of indium antimonide leads to missing peaks and that the other peaks are twice as large. The translation of (0.5,0.5) leads to the following:

The structure factor is.

$$e^{2\pi i(hx+ky)} + e^{2\pi i(h(x+\frac{1}{2})+k(y+\frac{1}{2}))} \tag{E.1}$$

$$= e^{2\pi i(hx+ky)} + e^{2\pi i(hx+ky)}e^{2\pi i(\frac{h}{2}+\frac{k}{2})} \tag{E.2}$$

$$= (1 + e^{2\pi i(\frac{h+k}{2})})e^{2\pi i(hx+ky)} \tag{E.3}$$

which is zero when $h+k = 2n+1$ and 2 when $h+k=2n$.

.

Bibliography

[1] N. L. Allinger, Y. H. Yuh, and J. H. Lii. Molecular mechanics - the mm3 force-field for hydrocarbons .1. *J. Amer. Chem. Soc.*, 111:8551–8566, 1989.

[2] J. Als-Nielsen and D. McMorrow. *Elements of Modern X-ray Physics.* Wiley, 2001.

[3] T. Bar, T. V. De Bocarme, and N. Kruse. Structural changes of Ag crystals during reaction with nitric oxide. *Surface Science*, 454:240–245, 2000.

[4] W. Barvosa-Carter, A. S. Bracker, J. C. Culbertson, B. Z. Nosho, B. V. Shanabrook, L. J. Whitman, H. Kim, N. A. Modine, and E. Kaxiras. Structure of III-Sb(001) growth surfaces: The role of heterodimers. *Phys. Review Letters*, 84:4649–4652, 2000.

[5] J. D. Batteas, J. C. Dunphy, G. A. Somorjai, and M. Salmeron. Coadsorbate induced reconstruction of a stepped Pt(111) surface by sulfur and CO: A novel surface restructuring mechanism observed by scanning tunneling microscopy. *Phys. Review Letters*, 77:534–537, 1996.

[6] L. Becker, S. Aminpirooz, B. Hillert, M. Pedio, J. Haase, and D. L. Adams. Threefold-coordinated hollow adsorption site for Ni(111)-c(4x2)-CO - a surface-extended X-ray-absorption fine- structure study. *Phys. Review B-Condensed Matter*, 47:9710–9714, 1993.

[7] P. Bernard, K. Peters, J. Alvarez, and S. Ferrer. Ultrahigh vacuum high pressure chamber for surface X-ray diffraction experiments. *Review Scientific Instruments*, 70:1478–1480, 1999.

[8] D. K. Biegelsen, R. D. Bringans, J. E. Northrup, and L. E. Swartz. Surface reconstructions of GaAs(100) observed by scanning tunneling microscopy. *Phys. Review B-Condensed Matter*, 41:5701–5706, 1990.

[9] C. Binns, C. Norris, and M. G. Bartheslabrousse. Adsorbed metallic chains as approximations to quasi-one-dimensional systems. *Physica Scripta*, T45:283–288, 1992.

[10] J. Bohr, R. Feidenhansl, M. Nielsen, M. Toney, R. L. Johnson, and I. K. Robinson. Model-independent structure determination of the InSb(111)2x2 surface - reply. *Phys. Review Letters*, 56:2878–2878, 1986.

[11] R. Brako and D. Sokcevic. Adsorbate-induced substrate relaxation and the adsorbate-adsorbate interaction. *Surface Science*, 469:185–195, 2000.

[12] M. Brogan. Use of nickel in autocatalysts. Private communication, 2000.

[13] G. Brown and D.E. Moncton, editors. *Handbook on Synchrotron Radiation*, chapter Surface Crystallography Chapter 7. North-Holland, 1991.

[14] Catalysts and Far East Chemicals Inc. Catalysts for synthesis gas production. http://www.ccife.co.jp/product1-e.htm, 2000.

[15] J. Cerda, F. J. Palomares, and F. Soria. Structure of GaAs(100)-c(8x2)-Ga. *Phys. Review Letters*, 75:665–668, 1995.

[16] P. Cernota, K. Rider, H. A. Yoon, M. Salmeron, and G. Somorjai. Dense structures formed by CO on Rh(111) studied by scanning tunneling microscopy. *Surface Science*, 445:249–255, 2000.

[17] Advanced Ceramics Cleveland, Ohio, USA. UHV compatible ceramic heating element. http://www.advceramics.com/.

[18] G. Comelli, V. R. Dhanak, M. Kiskinova, K. C. Prince, and R. Rosei. Oxygen and nitrogen interaction with rhodium single crystal surfaces. *Surface Science Reports*, 32:167–231, 1998.

[19] F. Comin. A cryogenically cooled, sagittal focusing scanning monochromator for ESRF. *Review Scientific Instruments*, 66:2082–2084, 1995.

[20] P Coppens, editor. *Synchrotron Radiation Crystallography*. Academic Press, 1992.

[21] J.M Cowley. *Diffraction Physics*. North-Holland, 1986.

[22] Daresbury. Srs station 9.4. http://srs.dl.ac.uk/, 2000.

[23] A. A. Davis, R. G. Jones, G. Falkenberg, L. Seehofer, R. L. Johnson, and C. F. McConville. Evidence from scanning tunneling microscopy in support of a structural model for the InSb(001)-c(8x2) surface. *Applied Phys. Letters*, 75:1938–1940, 1999.

[24] R. Davis, D. P. Woodruff, P. Hofmann, O. Schaff, V. Fernandez, K. M. Schindler, V. Fritzsche, and A. M. Bradshaw. Local structure determination for low-coverage CO on Ni(111). *J. Phys.-Condensed Matter*, 8:1367–1379, 1996.

[25] P. de Groot, M. Coulon, and K. Dransfeld. $Ni(CO)_4$ formation on Ni single crystals: reaction kinetics and observation of surface faceting induced by the reaction. *Surface Science*, 94:204–220, 1980.

[26] T. Dellwig, G. Rupprechter, H. Unterhalt, and H. J. Freund. Bridging the pressure and materials gaps: High pressure sum frequency generation study on supported Pd nanoparticles. *Phys. Review Letters*, 85:776–779, 2000.

[27] V. R. Dhanak, A. Baraldi, R. Rosei, M. Kiskinova, P. W. Murray, G. Thornton, and M. Bowker. Reconstructive interactions in mixed N+O layers on Rh(110). *Phys. Review B-Condensed Matter*, 50:8807–8815, 1994.

[28] R. Doll and M. A. Vanhove. Global optimization in LEED structure determination using genetic algorithms. *Surface Science*, 355:L393–L398, 1996.

[29] D.M. Eigler and Schweizer E.K. Positioning single atoms with a scanning tunneling microscope. *Nature*, 344:524–526, 1990.

[30] H. Eisele, O. Flebbe, T. Kalka, and M. Dahne-Prietsch. Cross-sectional STM study of InAs quantum dots for laser devices. *Surface Interface Analysis*, 27:537–541, 1999.

[31] ESRF. Characteristics of beam modes at the esrf. `http://www.esrf.fr/machine/myweb/MODES.html`, 2000.

[32] ESRF. European Synchrotron Radiation Facility (esrf). `http://www.esrf.fr/`, 2000.

[33] ESRF. Surface Diffraction beamline ID3. `http://www.esrf.fr/exp_facilities/ID3/user_guide/`, 2000.

[34] R. Feidenhansl. Surface-structure determination by X-ray diffraction. *Surface Science Reports*, 10:105–188, 1989.

[35] S. Ferrer and F. Comin. Surface diffraction beamline at ESRF. *Review Scientific Instruments*, 66:1674–1676, 1995.

[36] S. Ferrer, X. Torrelles, V. H. Etgens, H. A. Vandervegt, and P. Fajardo. Atomic-structure of the c(4x2) surface reconstruction of Ge(001) as determined by X-ray-diffraction. *Phys. Review Letters*, 75:1771–1774, 1995.

[37] N. Flanders. Britney spears guide to semiconductor physics. `http://britneyspears.ac/physics/vcsels/vcsels.htm`.

[38] M. Freemantle. *Chemistry in action.* Macmillan Education, 1987.

[39] E. Fridell, H. Persson, B. Westerberg, L. Olsson, and M. Skoglundh. The mechanism for NOx storage. *Catalysis Letters*, 66:71–74, 2000.

[40] H. X. Gao and L. M. Peng. Parameterization of the temperature dependence of the Debye-Waller factors. *Acta Crystallographica Section A*, 55:926–932, 1999.

[41] A. Gaussmann and N. Kruse. CO-induced structural-changes of Pd particle surfaces. *Catalysis Letters*, 10:305–315, 1991.

[42] C. Giacovazzo, editor. *Fundamentals of Crystallography.* Oxford Science Publications, 1992.

[43] C. J. Gilmore and G. Bricogne. Mice computer program. *Methods Enzymology*, 277:65–78, 1997.

[44] D.E. Goldberg. *Genetic algorithms in search, Optimization and machine learning.* Addison Wesley, 1989.

[45] D. W. Goodman. Catalysis - from single-crystals to the real-world. *Surface Science*, 300:837–848, 1994.

[46] D. W. Goodman. Correlations between surface science models and "real- world" catalysts. *J. Phys. Chem.*, 100:13090–13102, 1996.

[47] S. J. Gurman and R. L. McGreevy. Reverse Monte-Carlo simulation for the analysis of EXAFS data. *J. Phys.-Condensed Matter*, 2:9463–9473, 1990.

[48] Theo Hahn, editor. *International Tables for Crystallography*, volume A - Space-Group Symmetry. International union of Crystallography, 1996.

[49] B. Hammer. Bond activation at monatomic steps: NO dissociation at corrugated Ru(0001). *Phys. Review Letters*, 83:3681–3684, 1999.

[50] D. J. Hannaman and M. A. Passler. Structural determination of Ni(110)-(2x1)2CO by LEED - differentiation of substrate-C and C-O tilt angles. *Surface Science*, 203:449–462, 1988.

[51] M. Henzler. Growth modes in homoepitaxial and heteroepitaxial growth. *Progress Surface Science*, 42:297–316, 1993.

[52] Madden H.H., Kuppers J., and Ertl G. Interaction of carbon monoxide with (110) nickel surfaces. *Journal of Chemical Physics*, 58(8):3401–3410, April 1973.

[53] G. Hill and J. Holman. *Chemistry in Context*. Thomas Nelson and sons, 1989.

[54] P. B. Howes, K. A. Edwards, J. E. MacDonald, T. Hibma, T. Bootsma, M. A. James, and C. L. Nicklin. The atomic structure of the Si(111)-Pb buried interface grown on the Si(111)-($\sqrt{3} \times \sqrt{3}$)-Pb reconstruction. *Surface Review Letters*, 5:163–166, 1998.

[55] A Iandelli. Sulla struttura dei composti in p, in as e in sb. *Gazz.Chim.Ital.*, 1940.

[56] IBM. STM image gallery. http://www.almaden.ibm.com/vis/stm/gallery.html, 2000.

[57] P. W. Jacobs and G. A. Somorjai. Conversion of heterogeneous catalysis from art to science: the surface science of heterogeneous catalysis. *J. Molecular Catalysis A-Chem.*, 131:5–18, 1998.

[58] J. A. Jensen, K. B. Rider, Y. Chen, M. Salmeron, and G. A. Somorjai. High pressure, high temperature scanning tunneling microscopy. *J. Vacuum Science and Technology B*, 17:1080–1084, 1999.

[59] J. A. Jensen, K. B. Rider, M. Salmeron, and G. A. Somorjai. High pressure adsorbate structures studied by scanning tunneling microscopy: CO on Pt(111) in equilibrium with the gas phase. *Phys. Review Letters*, 80:1228–1231, 1998.

[60] P. John, T. Miller, and T. C. Chiang. Insb(100) reconstructions probed with core-level photoemission. *Phys. Review B-Condensed Matter*, 39:1730–1737, 1989.

[61] A. D. Johnson. Use of miscut on InSb(001) to improve device properties. Private Communication.

[62] N. Jones, C. Norris, C. L. Nicklin, P. Steadman, S. H. Baker, A. D. Johnson, and S. L. Bennett. Atomic structure of the InSb(001)-c(8x2) reconstruction determined by X-ray diffraction. *Surface Science*, 409:27–36, 1998.

[63] N. Jones, C. Norris, C. L. Nicklin, P. Steadman, J. S. G. Taylor, A. D. Johnson, and C. F. Mcconville. Atomic structure of the InSb(001)-c(4x4) reconstruction determined by X-ray diffraction. *Surface Science*, 398:105–116, 1998.

[64] N. Jones, C. Norris, C. L. Nicklin, P. Steadman, J. S. G. Taylor, C. F. McConville, and A. D. Johnson. An X-ray diffraction study of oxide removal from InSb(001) substrates. *Applied Surface Science*, 123:141–145, 1998.

[65] S. D. Kevan. Surface-states and reconstruction on Ge(001). *Phys. Review B*, 32:2344–2350, 1985.

[66] S. D. Kevan, R. F. Davis, D. H. Rosenblatt, J. G. Tobin, M. G. Mason, D. A. Shirley, C. H. Li, and S. Y. Tong. Structural determination of molecular overlayer systems with normal photoelectron diffraction - c(2x2) CO-Ni(001) and (square-root-3 x square-root-3) R30-degrees CO-Ni(111). *Phys. Review Letters*, 46:1629–1632, 1981.

[67] R Koper. Ni(110) sample supplied by "surface preparation laboratory", The Netherlands.

[68] U. Korte. Interpretation of reflection high energy electron diffraction from disordered surfaces: Dynamical theory and its application to the experiment. *Surface Review Letters*, 6:461–495, 1999.

[69] C. Kumpf, O. Bunk, J. H. Zeysing, Y. Su, M. Nielsen, R. L. Johnson, R. Feidenhans'l, and K. Bechgaard. Low-temperature structure of in-

dium quantum chains on silicon. *Phys. Review Letters*, 85:4916–4919, 2000.

[70] C. Kumpf, L. D. Marks, D. Ellis, D. Smilgies, E. Landemark, M. Nielsen, R. Feidenhans, J. Zegenhagen, O. Bunk, J. H. Zeysing, Y. Su, and R. L. Johnson. Subsurface dimerization in III-V semiconductor (001) surfaces. *Phys. Review Letters*, 86:3586–3589, 2001.

[71] C. Kumpf, D. Smilgies, E. Landemark, M. Nielsen, R. Feidenhans'l, O. Bunk, J. H. Zeysing, Y. Su, R. L. Johnson, L. Cao, J. Zegenhagen, B. O. Fimland, L. D. Marks, and D. Ellis. Structure of metal-rich (001) surfaces of III-V compound semiconductors - art. no. 075307. *Phys. Review B*, 6407:5307-+, 2001.

[72] K. Y. Kung, P. Chen, F. Wei, Y. R. Shen, and G. A. Somorjai. Sum-frequency generation spectroscopic study of CO adsorption and dissociation on Pt(111) at high pressure and temperature. *Surface Science*, 463:L627–L633, 2000.

[73] K. Lascelles and L. V. Renny. The rate of formation of nickel carbonyl from carbon-monoxide and nickel single-crystals. *Surface Science*, 125:L67–L72, 1983.

[74] J. H. Lii and N. L. Allinger. Molecular mechanics - the mm3 force-field for hydrocarbons .2. vibrational frequencies and thermodynamics. *J. Amer. Chem. Soc.*, 111:8566–8575, 1989.

[75] S. Lizzit, A. Baraldi, D. Cocco, G. Comelli, G. Paolucci, R. Rosei, and M. Kiskinova. NO adsorption on the Rh(110) surface: kinetics

and composition of the adlayer studied by fast XPS. *Surface Science*, 410:228–236, 1998.

[76] A. Locatelli, B. Brena, G. Comelli, S. Lizzit, G. Paolucci, and R. Rosei. Structural determination of the Pd{110}(2x1)p2mg-CO system by means of high-energy X-ray photoelectron diffraction. *Phys. Review B-Condensed Matter*, 54:2839–2845, 1996.

[77] M. O. Lorenzo, C. J. Baddeley, C. Muryn, and R. Raval. Extended surface chirality from supramolecular assemblies of adsorbed chiral molecules. *Nature*, 404:376–379, 2000.

[78] L. D. Mapledoram, M. P. Bessent, A. Wander, and D. A. King. An automated tensor LEED analysis of the Ni(111)-c(4x2)-2CO structure. *Chem. Phys. Letters*, 228:527–532, 1994.

[79] Johnson Matthey. How we control pollution today: passenger cars. http://www.johnsonmatthey.com/environment/cuttingpollution/02.html, 2000.

[80] C. F. McConville, T. S. Jones, F. M. Leibsle, S. M. Driver, T. C. Q. Noakes, M. O. Schweitzer, and N. V. Richardson. Surface reconstructions of InSb(100) observed by scanning-tunneling-microscopy. *Phys. Review B*, 50:14965–14976, 1994.

[81] B. J. McIntyre, M. Salmeron, and G. A. Somorjai. A variable pressure temperature scanning tunneling microscope for surface science and catalysis studies. *Review Scientific Instruments*, 64:687–691, 1993.

[82] A. Mellergard and R. L. McGreevy. Reverse Monte Carlo modelling of neutron powder diffraction data. *Acta Crystallographica Section A*, 55:783–789, 1999.

[83] V. Metcalfe and A. Gierth. Unix socket FAQ. `http://www.ntua.gr/sock-faq/sfaq.html`.

[84] A. Munkholm and S. Brennan. Influence of miscut on crystal truncation rod scattering. *J. Applied Crystallography*, 32:143–153, 1999.

[85] H. Nakano, S. Kawakami, T. Fujitani, and J. Nakamura. Carbon deposition by disproportionation of CO on a Ni(977) surface. *Surface Science*, 454:295–299, 2000.

[86] C. L. Nicklin, J. S. G. Taylor, N. Jones, P. Steadman, and C. Norris. An ultrahigh-vacuum chamber for surface x-ray diffraction. *J. Synchrotron Radiation*, 5:890–892, 1998.

[87] M. Nielsen, R. Feidenhans'l, F. B. Rasmussen, J. Baker, G. Falkenberg, L. Lottermoser, R. L. Johnson, A. J. Steinfort, and P. M. L. Scholte. Epitaxial clusters studied by synchrotron X-ray diffraction and scanning tunneling microscopy. *Physica B*, 248:1–8, 1998.

[88] C.A Norris. Grazing incidence fluorescence. Private communication.

[89] Chalmers University of Technology. *Stereochemistry of Limonene*, 2001. `http://www.oc.chalmers.se/spartanc/lab7.html`.

[90] J. S. Ozcomert, W. W. Pai, N. C. Bartelt, and J. E. Reuttrobey. Kinetics of oxygen-induced faceting of vicinal Ag(110). *Phys. Review Letters*, 72:258–261, 1994.

[91] N. Pangher and J. Haase. Bridge-bonded CO in Ni(110)-p2mg(2x1)-CO - a SEXAFS study. *Surface Science*, 293:L908–L911, 1993.

[92] S.S.P. Parkin. The magic of magnetic multilayers. *IBM Journal of Research and Development*, 42(1), 1998. Also available as http://www.research.ibm.com/journal/rd/421/parkin.html.

[93] V. I. Parvulescu, P. Grange, and B. Delmon. Catalytic removal of NO. *Catalysis Today*, 46:233–316, 1998.

[94] D. W. Pashley, J. H. Neave, and B. A. Joyce. A model for the appearance of chevrons on RHEED patterns from InAs quantum dots. *Surface Science*, 476:35–42, 2001.

[95] T.J. Pearson. Pgplot graphics subroutine library. http://www.astro.caltech.edu/~tjp/pgplot/.

[96] R.E. Peierls. *Quantum Theory of Solids*. Clarendon, 1955.

[97] L. M. Peng, G. Ren, S. L. Dudarev, and M. J. Whelan. Debye-Waller factors and absorptive scattering factors of elemental crystals. *Acta Crystallographica Section A*, 52:456–470, 1996.

[98] K. F. Peters, P. Steadman, H. Isern, J. Alvarez, and S. Ferrer. Elevated-pressure chemical reactivity of carbon monoxide over Au(111). *Surface Science*, 467:10–22, 2000.

[99] K.F Peters. AFM study of Ni(110) surface after heating in 2.3 bar of carbon monoxide. Private Communication.

[100] K.F. Peters, C.J. Walker, P. Steadman, O. Robach, H. Isern, and S. Ferrer. The adsorption of carbon monoxide on Ni(110) above atmospheric pressure investigated with surface X-ray diffraction. *Phys. Review Letters*, 86:5325, 2001.

[101] I. K. Robinson. Crystal truncation rods and surface-roughness. *Phys. Review B-Condensed Matter*, 33:3830–3836, 1986.

[102] I. K. Robinson. X-ray crystallography of surfaces and interfaces. *Acta Crystallographica Section A*, 54:772–778, 1998.

[103] I. K. Robinson, S. Ferrer, X. Torrellas, J. Alvarez, R. Vansilfhout, R. Schuster, K. Kuhnke, and K. Kern. Vibrational anisotropy of a CO monolayer on Ni(110). *Europhysics Letters*, 32:37–42, 1995.

[104] Roger Sayle and E. James Milner-White. Rasmol: Biomolecular graphics for all. *Trends in Biochemical Sciences (TIBS)*, 20(9):374, September 1995.

[105] U. Shmueli, editor. *International Tables for Crystallography*, volume B - Reciprocal Space. International union of Crystallography, 1996.

[106] A. Siokou, R. M. Van Hardeveld, and J. W. Niemantsverdriet. Surface reactions of nitrogen oxide on rhodium(100), adsorption, dissociation and desorption. *Surface Science*, 404:110–114, 1998.

[107] S. L. Skala, J. S. Hubacek, J. R. Tucker, J. W. Lyding, S. T. Chou, and K. Y. Cheng. Structure of GaAs(100)-c(8x2) determined by scanning-tunneling-microscopy. *Phys. Review B-Condensed Matter*, 48:9138–9141, 1993.

[108] Certified Scientific Software. spec x-ray diffraction and data acquisition software. http://www.certif.com/, 2000.

[109] G. A. Somorjai. Surface reconstruction and catalysis. *Annual Review Phys. Chem.*, 45:721–751, 1994.

[110] G. A. Somorjai. The surface science of heterogeneous catalysis. *Surface Science*, 300:849–866, 1994.

[111] G. A. Somorjai. Modern surface science and surface technologies: An introduction. *Chem. Rev.*, 96:1223–1235, 1996.

[112] G. A. Somorjai. New model catalysts (platinum nanoparticles) and new techniques (SFG and STM) for studies of reaction intermediates and surface restructuring at high pressures during catalytic reactions. *Applied Surface Science*, 121:1–19, 1997.

[113] G. A. Somorjai and G. Rupprechter. Molecular studies of catalytic reactions on crystal surfaces at high pressures and high temperatures by infrared-visible sum frequency generation (SFG) surface vibrational spectroscopy. *J. Phys. Chem. B*, 103:1623–1638, 1999.

[114] G.A. Somorjai. *Introduction to Surface Chemistry and Catalysis*. John Wiley and Sons Inc., 1994.

[115] P. Sprunger, F. Besenbacher, and I. Stensgaard. STM study of the Ni(110)-(2x1)-2CO system - structure and bonding-site determination. *Surface Science*, 324:L321–L327, 1995.

[116] P. Steadman, K. Peters, H. Isern, J. Alvarez, and S. Ferrer. Interaction of CO with the reconstructed Au(111) surface near atmospheric pressures. *Phys. Review B*, 62:R2295–R2298, 2000.

[117] A. J. Steinfort, P. M. L. O. Scholte, A. Ettema, F. Tuinstra, M. Nielsen, E. Landemark, D. M. Smilgies, R. Feidenhansl, G. Falkenberg, L. Seehofer, and R. L. Johnson. Strain in nanoscale germanium hut clusters on Si(001) studied by X-ray diffraction. *Phys. Review Letters*, 77:2009–2012, 1996.

[118] C. Stelz. Thalidomide and the importance of chirality. http://www.geocities.com/cs9309_2000/code.html, 2001.

[119] M. A. Van Hove. Surface crystallography - an educational review. *Heterogeneous Chem. Rev.*, 2:81–89, 1995.

[120] M. A. Van Hove, K. Hermann, P. R. Watson, and J. Rumble. Greatly improved surface structure database - ssd version 3. *Surface Review Letters*, 6:805–811, 1999.

[121] P. R. Varekamp, M. Bjorkqvist, M. Gothelid, and U. O. Karlsson. Observation of true c(8x2) symmetry in scanning tunnelling microscopy images of the clean InSb(001) surface. *Surface Science*, 350:L221–L226, 1996.

[122] J.A Venables. *Introduction to surface and thin film processes.* Cambridge University Press, 2000.

[123] E. Vlieg. *A Concise ROD manual.* Department of Solid state chemistry, University of Nijmegen, The Netherlands. `http://www.esrf.fr/computing/scientific/joint_projects/ANA-ROD/index.ht%ml`.

[124] E. Vlieg. *From beam time to structure factors.* `http://www.esrf.fr/computing/scientific/joint_projects/ANA-ROD/index.html`.

[125] E. Vlieg. Integrated intensities using a six-circle surface X-ray diffractometer. *J. Applied Crystallography*, 30:532–543, 1997.

[126] E. Vlieg. A (2+3)-type surface diffractometer: mergence of the z-axis and (2+2)-type geometries. *J. Applied Crystallography*, 31:198–203, 1998.

[127] E. Vlieg. ROD: a program for surface X-ray crystallography. *Journal of Applied Crystallography*, 33:401–405, 2000.

[128] E. Vlieg, O. Svensson, and R. Wilke. Anarod. `http://www.esrf.fr/computing/scientific/joint_projects/ANA-ROD/index.html`.

[129] E. Vlieg, J. F. Van der Veen, S. J. Gurman, C. Norris, and J. E. MacDonald. X-ray-diffraction from rough, relaxed and reconstructed surfaces. *Surface Science*, 210:301–321, 1989.

[130] B. Voigtlander, D. Bruchmann, S. Lehwald, and H. Ibach. Structure and adsorbate adsorbate interactions of the compressed Ni(110)-(2x1)CO structure. *Surface Science*, 225:151–161, 1990.

[131] C. Voss and N. Kruse. Field-promoted morphological changes of Pt crystals after NO adsorption. *Surface Science*, 416:L1114–L1117, 1998.

[132] C.J. Walker. Rasmol extensions to ROD. `http://www.esrf.fr/computing/scientific/joint_projects/ANA-ROD/index.ht%ml`.

[133] T. R. Ward, R. Hoffmann, and M. Shelef. Coupling nitrosyls as the 1st step in the reduction of NO on metal-surfaces - the special role of rhodium. *Surface Science*, 289:85–99, 1993.

[134] J. D. Watson and Crick F.H.C. structure for deoxyribose nucleic acid. *Nature*, 1953.

[135] R.C. Weast, editor. *Handbook of Chemistry and Physics*. CRC press, Inc, 55 edition, 1974.

[136] S. Weichel, F. Grey, K. Rasmussen, M. Nielsen, R. Feidenhans'l, P. B. Howes, and J. Vedde. Fusion bonding of Si wafers investigated by X-ray diffraction. *Applied Phys. Letters*, 76:70–72, 2000.

[137] D. A. Wesner, F. P. Coenen, and H. P. Bonzel. X-ray photo-electron diffraction study of perpendicular and tilted CO on clean and potassium-modified Ni(110). *Phys. Review B-Condensed Matter*, 39:10770–10780, 1989.

[138] M. Weygand, M. Schalke, P. B. Howes, K. Kjaer, J. Friedmann, B. Wetzer, D. Pum, U. B. Sleytr, and M. Losche. Coupling of protein sheet crystals (s-layers) to phospholipid monolayers. *J. Materials Chem.*, 10:141–148, 2000.

[139] E. D. Williams. Surface steps and surface-morphology - understanding macroscopic phenomena from atomic observations. *Surface Science*, 300:502–524, 1994.

[140] A.J.C Wilson and E. Prince, editors. *International Tables for Crystallography*, volume C - Mathematical, physical and chemical tables. IUCR, second edition, 1999.

[141] Mark Winter. Webelements periodic table home of the periodic table on the world-wide web. `http://www.webelements.com/`.

[142] E.A. Wood. Vocabulary of surface crystallography. *Journal of Applied Physics*, 35(4):1306–1312, 1963.

[143] R.W.G. Wyckoff. *Crystal structures*. Interscience, 1969.

[144] W. S. Yang and R. G. Zhao. Model-independent structure determination of the InSb(111)2x2 surface. *Phys. Review Letters*, 56:2877–2877, 1986.

[145] Jr. Yates J.T. *Experimental Innovations in Surface Science*. Springer-Verlag, New York, 1998.

[146] C. J. Yu, A. G. Richter, J. Kmetko, S. W. Dugan, A. Datta, and P. Dutta. Structure of interfacial liquids: X-ray scattering studies - art. no. 021205. *Phys. Review E*, 63:021205, 2001.

[147] C. Zhao and M. A. Passler. A reinvestigation of the surface-structure of Ni(110)- (2x1)2CO by LEED. *Surface Science*, 320:1–6, 1994.